AD-A187 953 AL AND MG ALLOYS FOR AEROSPACE APPLICATIONS USING RAPID 1/1
SOLIDIFICATION AN..(U) ILLINOIS UNIV AT URBANA DEPT OF
MATERIALS SCIENCE AND ENGINEE.. H L FRASER 07 OCT 81
UNCLASSIFIED AFOSR-TR-87-1584 AFOSR-85-0191 F/G 11/6 1 NL

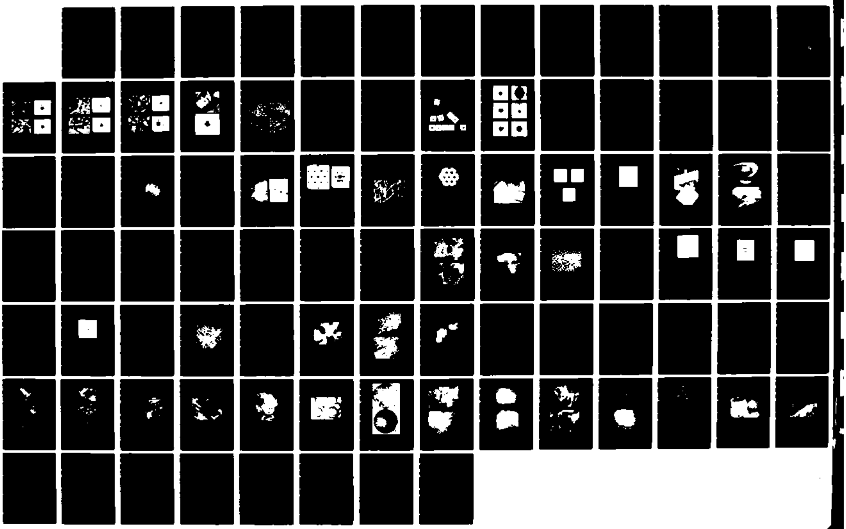

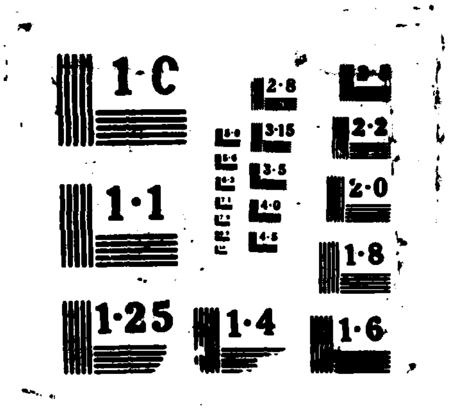
1·0
2·8
2·5
3·15
2·2
3·5
4·0
2·0
1·1
4·5
1·8
1·25
1·4
1·6

DTIC FILE COPY

②

AFOSR-TR- 87-1584

AD-A187 953

SECOND ANNUAL TECHNICAL REPORT

ON

Al and Mg ALLOYS FOR AEROSPACE APPLICATIONS USING RAPID SOLIDIFICATION AND POWDER METALLURGY PROCESSING

AFOSR Grant No: AFOSR-85-0191

DTIC
S ELECTE D
NOV 1 7 1987
D

Submitted by

Hamish L. Fraser
Department of Materials Science & Engineering
University of Illinois
1304 W. Green Street
Urbana, IL 61801

DISTRIBUTION STATEMENT A
Approved for public release;
Distribution Unlimited

87 10 [illegible] 069

Table of Contents

1. INTRODUCTION 1
2. SUMMARY STATEMENTS 2
3. RESULTS 3
    3.1 Al Alloys for Elevated Temperature Applications (Al-8Fe-2Mo) 3
        -- Al-8Fe-2Mo Alloy 4
        -- Al-8Fe-2Mo-Si Alloys 5
    3.2 Mg-Gd Alloys 21
        -- Solution-Treated and Aged Alloys 21
        -- Mechanical Behavior 23
    3.3. Mg-Si Alloys 35
        3.3.1. As-Cast 37
        3.3.2. Melt Spun Ribbon 38
        -- Evolution of Microstructure in Melt-spun Mg-Si Alloys 39
        -- Aging Response of Melt-spun Alloys 40
        -- Microhardness of Melt-spun Alloys 42
    3.4 Mg-Li Alloys 61
        3.4.1 Melt-Spun Ribbons 61
        3.4.2 Centrifugally Atomized Powder 62
        -- As-Atomized Microstructure 62
        -- Dynamically Compacted Material 63
        -- Hot Isostatically Pressed (HIP) Material 64
4. REFERENCES 82
5. FUTURE WORK 84
6. PUBLICATIONS FROM AFOSR SUPPORT 85

DTIC
COPY
INSPECTED
6

A-1

SECURITY CLASSIFICATION OF THIS PAGE (*When Data Entered*)

REPORT DOCUMENTATION PAGE		**READ INSTRUCTIONS BEFORE COMPLETING FORM**
1. REPORT NUMBER AFOSR-TR- 87-1584	2. GOVT ACCESSION NO.	3. RECIPIENT'S CATALOG NUMBER
4. TITLE (*and Subtitle*) Al and Mg Alloys for Aerospace Applications Using Rapid Solidification and Powder		5. TYPE OF REPORT & PERIOD COVERED Second Annual Technical Report 6. PERFORMING ORG. REPORT NUMBER
7. AUTHOR(*s*) Hamish L. Fraser		8. CONTRACT OR GRANT NUMBER(*s*) AFOSR-85-0191
9. PERFORMING ORGANIZATION NAME AND ADDRESS University of Illinois, Dept. of Materials Science, 1304 W. Green Street, Urbana, IL 61801		10. PROGRAM ELEMENT, PROJECT, TASK AREA & WORK UNIT NUMBERS 61102F 2306/A1
11. CONTROLLING OFFICE NAME AND ADDRESS Air Force of Scientific Research, Bolling AFB, Bldg. 410, Washington, D.C. 20332 NE		12. REPORT DATE 10/7/87 13. NUMBER OF PAGES 85
14. MONITORING AGENCY NAME & ADDRESS(*if different from Controlling Office*) Same as 11		15. SECURITY CLASS. (*of this report*) unclassified 15a. DECLASSIFICATION/DOWNGRADING SCHEDULE

16. DISTRIBUTION STATEMENT (*of this Report*)

This document has been approved for public release; its distribution is unlimited.

17. DISTRIBUTION STATEMENT (*of the abstract entered in Block 20, if different from Report*)

18. SUPPLEMENTARY NOTES

19. KEY WORDS (*Continue on reverse side if necessary and identify by block number*)

Rapid Solidification Processing of Al- and Mg-alloys, Powder Metallurgy, Dynamic Powder Compaction

20. ABSTRACT (*Continue on reverse side if necessary and identify by block number*)

On reverse side.

DD FORM 1 JAN 73 1473 EDITION OF 1 NOV 65 IS OBSOLETE

SECURITY CLASSIFICATION OF THIS PAGE (*When Data Entered*)

Regarding the work on elevated temperature P/M Al alloys, the microstructural changes in rapidly solidified and heat-treated (450°C) Al-8Fe-2Mo-(0-1)Si alloys have been studied. The long-time heat-treated microstructure of the Si-free ternary alloy consists primarily of a rather coarse distribution of precipitates of the Al_6(Fe,Mo) and the monoclinic Al_3Fe phases in an α-Al matrix; small amounts of two additional phases, the BCC Al_p(Fe,Mo) and the BCC $Al_{12}Mo$, were also detected. In contrast, the alloys containing Si showed a uniform dispersion of fine cuboidal/polygonal precipitates of the BCC $Al_{12}(Fe,Mo)_3Si$ phase, with a markedly superior resistance to coarsening. From the standpoint of both an attractive morphology of precipitates and good thermal stability, alloys containing Si hold good promise for elevated temperature applications.

In the case of the studies of Mg-Gd alloys, the following summary remarks may be made. Firstly, the aging sequence for alloys which had been solution-treated and quenched has been established. Thus, following quenching, decomposition of the super-saturated solid solution involves the formation of coherent zones with a structure consistent with that of Mg_3Cd, with lattice parameters given by $a=6.43Å$ and $c=5.2Å$. These zones develop upon further aging into semi-coherent precipitates with an orthorhombic structure with lattice parameters given by $a=22.24Å$, $b=6.42Å$ and $c=5.21Å$. Finally, the equilibrium phase $Mg_{24}Gd_5$ is formed. The highest hardness achieved during aging was ≈ 133 (Knoop microhardness), obtained by aging for 2hrs at 300°C. The microstructure corresponding to that condition consisted of ellipsoidal particles of the orthorhombic phase, mentioned above, in a Mg matrix. This microstructural condition also gave rise to the highest strengths in tensile tests. The mechanical properties of these alloys was shown to be dependent on Gd content. Thus, although higher ultimate tensile strengths were realized in the case of alloys containing 20%Gd, a more satisfactory combination of properties were effected in the alloys containing 10%Gd. This was in part attributed to reduced grain boundary precipitation in the case of the more dilute alloy. In summary, the mechanical test results are indeed relatively exciting, and may be correlated in part to microstructure. A more detailed understanding of this relationship is being developed as part of the third year's work and will be summarized in the final report.

Concerning the study of Mg-Si alloys, the microstructures and properties of melt-spun Mg-Si ribbons have been studied. Three types of microstructures: cellular based on α-Mg, coupled eutectic of α-Mg and Mg_2Si, and dendritic Mg_2Si, have been observed. A microstructure composed entirely of the coupled eutectic structure of refined Mg_2Si rods in a α-Mg matrix was observed in a 5 wt.% Si alloy; this Si content is about four times higher than the equilibrium eutectic composition. The evolution of these microstructures can be explained on the basis of undercooling below the extended liquidus such that formation of the eutectic occurs in a region of coupled growth, this region being asymmetrical disposed towards the intermetallic compound. The microhardness and thermal stability of the completely coupled eutectic structure was markedly superior than that of the other alloys. Thus, the 5 wt.% Si alloy, with this structure, holds good promise for elevated temperature applications.

Finally, a preliminary study has been made of the effect of adding Si to binary Mg-Li alloys. The reason for adding Si involves the use of rapid solidifcation to effect a dispersion of silicide particles which may impart an improvement in the creep properties of these alloys. It was found that with Li present, it was not possible to effect using melt-spinning the refined microeutectic obtained in the Mg-5Si binary alloy at that level of Si. It was thought that this is due to the lowering of the eutectic temperature by Li additions. Further work is involved with lowering the Si concentration to enable the relationship between Si and Li content on the solidification mode to be determined, and hopefully permit the conditions required for the formation of the refined microeutectic in the ternary alloys to be predicted. These alloys have also been reduced to powders, and these have been compacted using dynamic compaction and also hot isostatic pressing. Mechanical properties have been obtained, and it has been shown that the effect of adding a relatively small amount of Si (1.5%) is to almost double the yield strengths of these alloys. The microstructure/property relationships are being determined curently.

1. INTRODUCTION

This report covers the progress made in the second year of a three study on the application of rapid solidification processing (RSP) to Al and Mg alloys. The main emphasis of this study has been on the understanding of the microstructures produced by rapid solidification. The alloy systems studied include: 1) Al alloys for elevated temperature applications, namely Al-8Fe-2Mo with additions of Si, and 2) Mg alloys for elevated temperature applications, namely, Mg-Gd, Mg-Li, Mg-Li-Si, and Mg-Si. The report is divided into three sections: Summary Statements, Results, and Future Work. Individual sections are further subdivided as appropriate.

2. SUMMARY STATEMENTS

Regarding the work on elevated temperature P/M Al alloys, the microstructural changes in rapidly solidified and heat-treated (450°C) Al-8Fe-2Mo-(0-1)Si alloys have been studied. The long-time heat-treated microstructure of the Si-free ternary alloy consists primarily of a rather coarse distribution of precipitates of the $Al_6(Fe,Mo)$ and the monoclinic Al_3Fe phases in an α-Al matrix; small amounts of two additional phases, the BCC $Al_p(Fe,Mo)$ and the BCC $Al_{12}Mo$, were also detected. In contrast, the alloys containing Si showed a uniform dispersion of fine cuboidal/polygonal precipitates of the BCC $Al_{12}(Fe,Mo)_3Si$ phase, with a markedly superior resistance to coarsening. From the standpoint of both an attractive morphology of precipitates and good thermal stability, alloys containing Si hold good promise for elevated temperature applications.

In the case of the studies of Mg-Gd alloys, the following summary remarks may be made. Firstly, the aging sequence for alloys which had been solution-treated and quenched has been established. Thus, following quenching, decomposition of the super-saturated solid solution involves the formation of coherent zones with a structure consistent with that of Mg_3Cd, with lattice parameters given by $a=6.43Å$ and $c=5.2Å$. These zones develop upon further aging into semi-coherent precipitates with an orthorhombic structure with lattice parameters given by $a=22.24Å$, $b=6.42Å$ and $c=5.21Å$. Finally, the equilibrium phase $Mg_{24}Gd_5$ is formed. The highest hardness achieved during aging was ≈ 133 (Knoop microhardness), obtained by aging for 2hrs at 300°C. The microstructure corresponding to that condition consisted of ellipsoidal particles of the orthorhombic phase, mentioned above, in a Mg matrix. This microstructural condition also gave rise to the highest strengths in tensile tests. The mechanical properties of these alloys was shown to be dependent on Gd content. Thus, although higher ultimate tensile strengths were realized in the case of alloys containing 20%Gd, a more satisfactory combination of properties were effected in the alloys containing 10%Gd. This was in part attributed to reduced grain boundary precipitation in the case of the more dilute alloy. In summary, the mechanical test results are indeed relatively exciting, and may be correlated in part to microstructure. A more detailed understanding of this relationship is being developed as part of the third year's work and will be summarized in the final report.

Concerning the study of Mg-Si alloys, the microstructures and properties of melt-spun Mg-Si ribbons have been studied. Three types of microstructures: cellular based on α-Mg, coupled eutectic of α-Mg and Mg_2Si, and dendritic Mg_2Si, have been observed. A microstructure composed entirely of the coupled eutectic structure of refined Mg_2Si rods in a α-Mg matrix was observed in a 5 wt.% Si alloy; this Si content is about four times higher than the equilibrium eutectic composition. The evolution of these microstructures can be explained on the basis of undercooling below the extended liquidus such that formation of the eutectic occurs in a region of coupled growth, this region being asymmetrical disposed towards the intermetallic compound. The microhardness and thermal stability of the completely coupled eutectic structure was markedly superior than that of the other alloys. Thus, the 5 wt.% Si alloy, with this structure, holds good promise for elevated temperature applications.

Finally, a preliminary study has been made of the effect of adding Si to binary Mg-Li alloys. The reason for adding Si involves the use of rapid solidifcation to effect a dispersion of silicide particles which may impart an improvement in the creep properties of these alloys. It was found that with Li present, it was not possible to effect using melt-spinning the refined microeutectic obtained in the Mg-5Si binary alloy at that level of Si. It was thought that this is due to the lowering of the eutectic temperature by Li additions. Further work is involved with lowering the Si concentration to enable the relationship between Si and Li content on the solidification mode to be determined, and hopefully permit the conditions required for the formation of the refined microeutectic in the ternary alloys to be predicted. These alloys have also been reduced to powders, and these have been compacted using dynamic compaction and also hot isostatic pressing. Mechanical properties have been obtained, and it has been shown that the effect of adding a relatively small amount of Si (1.5%) is to almost double the yield strengths of these alloys. The microstructure/property relationships are being determined curently.

3. RESULTS

3.1 Al Alloys for Elevated Temperature Applications (Al-8Fe-2Mo)

High purity Al-8Fe-2Mo alloy ingots containing 0, 0.5 and 1 wt.% Si were produced by induction melting in an argon atmosphere and casting into a copper mold. The ingots were sectioned, induction remelted in a quartz crucible under helium, and ejected by argon pressure onto a mild steel wheel rotating at a surface velocity of 35 m/s to produce rapidly solidified ribbons having a thickness of 25 to 50 μm and width of 3 to 6 mm. Cut ribbons were encapsulated in quartz under vacuum, and after heat-treating at 450°C for various times to 100 hrs quenched in water to arrest further transformation.

X-ray diffraction studies were performed on a Rigaku D-max diffractometer using Cu Kα radiation. Heat-treated ribbons (450°C, 50 hrs) of the 0.5 and 1 wt.% Si alloys were mounted on a glass slide, placed in the diffractometer chamber, and the patterns recorded. The scan was repeated five times and the intensities summed each time. Transmission electron microscopy (TEM) studies were carried out in the Philips EM420 and EM430 microscopes operating at 120 and 150 keV, respectively. Energy dispersive x-ray (EDX) microanalysis of the precipitates was conducted in a Vacuum Generator HB5 STEM, equipped with a field emission gun. The concentration of different elements was determined from the intensity of x-rays using standard techniques.[1] The proportionality constant relating the concentration ratios to the intensity ratios of the different elements[1] was determined using $Al_{12}Mo$, Mo_3Si, and Fe_2Mo line-compound standards.

The optical microstructure of Al-8Fe alloy particulate produced by RSP has been described by Jones[2] as either Zone A or Zone B, depending on its response to etching by Keller's reagent; the microstructure of the former appears featureless, whereas that of the latter exhibits strong contrast characteristic of a decomposed microstructure. On a finer scale, the Zone A microstructure appears as a cellular-dendritic structure based on α-Al with intercellular regions composed of a randomly oriented refined dispersion of particles of the quasicrystalline T' phase.[3] The as-rapidly solidified microstructure of all three alloys was completely Zone A, as shown, for example, in Fig. 1 for the 0.5 wt.% Si alloy. The microstructural changes in ribbons heat-treated at 450°C for times ranging from 0.25 to 100 hrs are described in the following.

Al-8Fe-2Mo Alloy

Within 0.25 hrs, precipitation occurred at grain boundaries, as shown in the bright field (BF) micrograph in Fig. 2a. Two types of precipitates, the $Al_6(Fe,Mo)$ phase[2,4,5] and a body centered cubic (BCC) phase having a lattice parameter of 1.27±0.005 nm, were identified; the latter phase was observed more commonly. A selected area diffraction (SAD) pattern from the grain boundary precipitate indicated by the arrow in Fig. 2a is shown in Fig. 2b. This and other patterns could be indexed consistently on the basis of a BCC lattice. Energy dispersive x-ray (EDX) microanalysis indicated that the BCC phase was based on Al and contained significantly larger amounts of Fe compared to Mo; small amounts of Si were also present. The exact stoichiometry has not been determined yet, but is tentatively described as $Al_p(Fe,Mo)$. Generally, other than a slight coarsening of the intercellular phase, the intragranular structure showed little or no change in most areas of the microstructure. However, thicker portions of the ribbon showed more decomposition, as seen in the example in Fig. 2c. The grain boundary precipitate labelled P in Fig. 2c was once again identified as the BCC $Al_p(Fe,Mo)$ phase (see associated SAD pattern in Fig. 2d). On occasion, the BCC phase was also observed as facetted particles within grains.

Further aging to 4 hrs led to additional precipitation of the $Al_6(Fe,Mo)$ and $Al_p(Fe,Mo)$ phases, together with transformation of the intragranular structure to needles of the orthorhombic θ' Al_3Fe phase.[4,5] Representative examples are shown in Figs. 3a and 3b. The precipitate labelled A in Fig. 3b was identified as $Al_6(Fe,Mo)$ (see SAD pattern in Fig. 3c), whereas the one labelled B was identified as the BCC $Al_p(Fe,Mo)$ phase (see [001] SAD pattern in Fig. 3d). The BCC Bravais lattice for this phase was confirmed by convergent beam electron diffraction.

On continued aging to 50 hrs, the orthorhombic θ' Al_3Fe needles disappeared; the microstructure at this stage consisted of a dispersion of rather coarse precipitates of the $Al_6(Fe,Mo)$, $Al_p(Fe,Mo)$ and the monoclinic Al_3Fe phases. In addition, a phase, tentatively identified as the BCC $Al_{12}Mo$ (lattice parameter of 0.758 nm), was also detected. TEM micrographs showing the $Al_6(Fe,Mo)$, $Al_p(Fe,Mo)$ and $Al_{12}Mo$ phases are presented in Figs. 4a–d. Evidence for the monoclinic Al_3Fe phase is shown in Fig. 5. This phase forms incoherently and displays fine twins (Fig. 5a), which produce extra spots and streaks in the diffraction pattern (Fig. 5b); the streaks form normal to the thin dimension of the twins. It appeared that the Al_3Fe phase formed at the grain boundaries from the $Al_6(Fe,Mo)$ and $Al_p(Fe,Mo)$ phases.

Al-8Fe-2Mo-Si Alloys

The aging response of these alloys was markedly different from that of the Al-8Fe-2Mo alloy. In contrast to the behavior of the ternary alloy at 0.25 hrs, precipitation was not limited to the grain and subgrain boundaries alone, but instead spread throughout the microstructure. A BF micrograph demonstrating this effect is shown in Fig. 6a for the 0.5 wt.% Si alloy. The precipitates which form at the grain and sub-grain boundaries are larger than those inside the grains; the latter appear with a straight-edged cuboidal/polygonal morphology, which indicates that nucleation may have taken place coherently.

Further aging to 4 hrs produced virtually no change in the microstructure (Fig. 6b). Although the intragranular precipitation processes commenced somewhat earlier in the Si-containing alloys relative to the Si-free alloy, the overall thermal stability was markedly superior, as evident from Figs. 6c and 6d, where the microstructures after a 50 hr aging are shown. There is some evidence of particle coarsening and spheroidization; however, the microstructures do not show the marked coarsening characteristic of the Al-8Fe-2Mo alloy. Moreover, no evidence was seen for either the Al_6Fe or the incoherent monoclinic Al_3Fe phases even after 100 hrs aging.

A typical x-ray diffraction pattern showing the variation of intensity (cps) as a function of 2θ is presented in Fig. 7 for the 1 wt.% Si alloy. The results of peak position, intensity, indexing and d-spacing of the various reflections are summarized in Table 1. All the precipitate reflections could be consistently indexed on the basis of a BCC lattice (h+k+l = 2n) with $a_0 = 1.263 \pm 0.003$ nm, which closely matches the value of 1.256 nm for the BCC α-AlFeSi compound,[6] and that of the precipitates reported in Al-8Fe-V-Si alloys.[7] No apparent change in the lattice parameter with Si content was observed. It should be noted that the 532 reflection is the strongest, followed by the 530, in agreement with other reports.[8] Detailed calculations of the structure factors to enable evaluation of the intensities has not been attempted.

Electron diffraction studies were carried out to confirm the x-ray results. Examples of diffraction patterns recorded from individual precipitates, covering the [001]-[011]-[111] streographic triangle, are shown in Fig. 8. These and all other patterns could be consistently indexed on the basis of a BCC lattice with a lattice parameter almost identical to that determined by x-ray diffraction.

To determine the point group and space group of the precipitates, convergent beam electron diffraction (CBED) was used. CBED patterns of the [001], [023], and [111] zone axes are shown in Figs. 9a—c. The BCC Bravais lattice for the precipitates is once again confirmed by examining the spacings and positions of reflections in the Zero Order Laue Zone (ZOLZ) and the First Order Laue Zone (FOLZ) in the [001] pattern. For a BCC lattice, the ratio of the spacings of the FOLZ and ZOLZ is equal to $\sqrt{2}$.[9] Measurements of these spacings from the patterns in Fig. 9a gave $d_{FOLZ}/d_{ZOLZ} = 12.68/9.03 = 1.4 \approx \sqrt{2}$, thus confirming the BCC lattice. Symmetry information deduced from the CBED patterns in Figs. 9a—c was compared to tables provided by Buxton et al.[10] The results are summarized in Table 2. For the [001] orientation, the projection diffraction and whole pattern symmetries are 2mm, which places the diffraction group as 2mm or $2mm1_R$. For the [023] zone axes, the projection diffraction, whole pattern and bright field (BF) symmetries are 2mm, m, and m, respectively, which gives 2_Rmm_R as the diffraction group. For the [111] zone axes, the projection diffraction and whole pattern symmetries are 6 and 3, respectively, which gives the diffraction group as 6_R. The possible point groups corresponding to the above diffraction groups (Table 3 of Buxton et al.[10]) are summarized in Table 3, from which it is established that the point group of the precipitates is m3.

The possible space groups for this point group are Pm3, Pn3, Pa3, Fm3, Fd3, Im3, and Ia3.[11] Since the lattice is BCC, the choice of space groups is reduced to the last two, namely, Im3 or Ia3. For the latter space group, reflections of type 0kl for which k and l are not multiples of 2, that is, of type 011, 033..., are forbidden, which is not the case here. Thus, the space group of the precipitates is unambiguously established as Im3, in agreement with that reported for the cubic α-AlFeSi compound.[6]

EDX microanalysis of the precipitates in both alloys was carried out. A typical spectrum of the intensity (counts) as a function of energy (keV) is shown in Fig. 10 for the 0.5 wt.% Si alloy . The average composition of the precipitates in both alloys, based on analyses of ten particles, is given in Table 4, together with that reported[12] for the cubic α-AlFeSi compound; it is evident that the compositions determined in this study are in excellent agreement. The structure, composition and morphology of these precipitates is identical to that of the precipitates reported in rapidly solidified and extruded in Al-Fe-V-Si alloys.[7]

The decomposition behavior of the Zone A microstructure in the Al-8Fe-2Mo alloy on aging is largely similar to that in binary Al-Fe alloys,[4,5] where the reaction takes place in three steps, namely: 1) formation of $Al_6(Fe,Mo)$ at the grain boundaries, 2) transformation of the intragranular structure to needles of the orthorhombic θ' Al_3Fe phase, and 3) transformation of these two phases to the equilibrium monoclinic Al_3Fe phase. In contrast, the transformation progresses more slowly in the ternary alloy. In addition to the phases mentioned above, two other phases have been detected in the present study, namely, the BCC $Al_p(Fe,Mo)$ and the BCC $Al_{12}Mo$. The $Al_p(Fe,Mo)$ phase and the precipitates in the Si-containing alloys are identical in structure and have closely comparable lattice parameters. Since Si was detected in this phase, trace amounts of this element present as an impurity presumably cause its formation. The $Al_{12}Mo$ phase forms possibly from the excess Mo which was not accommodated in the $Al_6(Fe,Mo)$ and $Al_p(Fe,Mo)$ phases.

The difference in transformation behavior between the Al-8Fe-2Mo alloy and the alloys containing Si can be understood on the basis of ternary Al-Fe-Si phase diagram. There is no published data on the Al-Fe-Mo phase diagram, but the present results suggest that with the addition of Si, the transformation behavior follows that in the Al-Fe-Si system, with Mo atoms substituting for the Fe.

The cubic α-AlFeSi compound is complex with 138 atoms per unit cell,[6] has a stochiometry corresponding to $Al_{20}Fe_5Si_2$,[12] and a range of homogeneity of about 5 wt.% Al.[13] A closer inspection of the composition reported by Phragmen[12] indicates a stochiometry near $Al_{12}Fe_3Si$. The equilibrium α-AlFeSi compound has an HCP structure with c=2.62 nm and a=1.23 nm, but is modified to the cubic form with a_o in the range of 1.25 to 1.27 nm by the presence of minor amounts (< 0.3 wt.%) of transition elements, notably Mn, V, Cr, W and Mo, substituting for the Fe.[14,15] The stoichiometric formula determined for the precipitates in this study corresponds to $Al_{19}Fe_4Mo_{0.3}Si_{1.3}$ and $Al_{19}Fe_4Mo_{0.3}Si_{1.7}$ for the 0.5 wt.% and 1 wt.% Si alloys, respectively, which is comparable to $Al_{19}Fe_4MnSi_2$ reported by Cooper[6] when trace amounts of Mn are present. On the assumption that the Mo atoms partially substitute for the Fe, the stoichiometry is obtained as $Al_{15}Fe_4Si$ for the 0.5 wt.% Si alloy and as $Al_{11}Fe_3Si$ for the 1 wt.% Si alloy, both being quite close to $Al_{12}Fe_3Si$.

Examination of the ternary Al-Fe-Si phase diagram[12,13] reveals that the equilibrium phases expected near 450°C for the alloy compositions used in this study are α-Al + Al_3Fe + cubic α-AlFeSi. However, the monoclinic Al_3Fe phase was not observed even after 100 hrs aging, although this phase is observed in the ternary Al-8Fe-2Mo alloy. Thus, an additional effect of Mo is to suppress the formation of this phase, either due to kinetic factors or thermodynamically by systematic alteration of the phase boundaries.

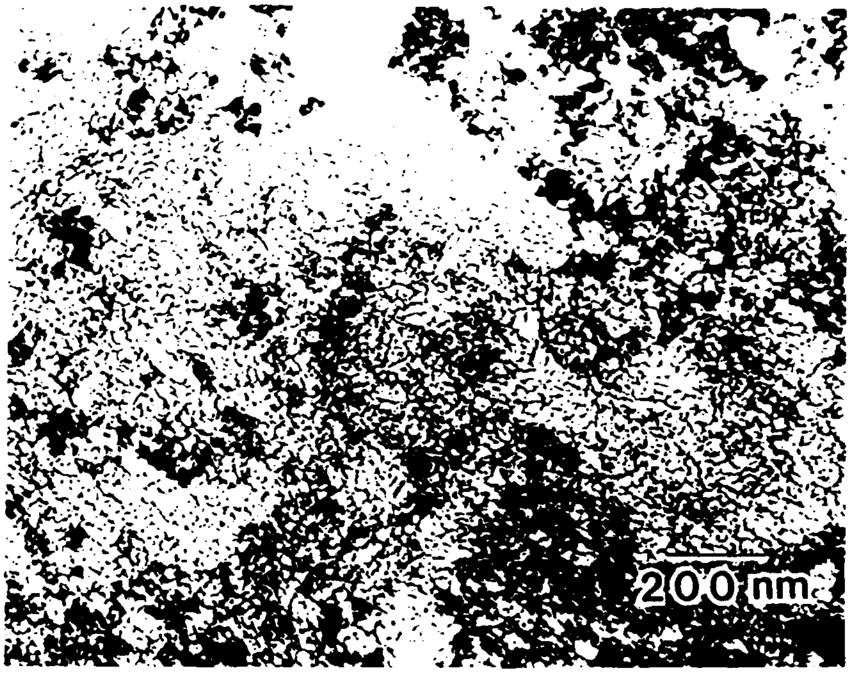

Figure 1. BF micrograph of as rapidly solidified Al-8Fe-2Mo-0.5Si alloy ribbon.

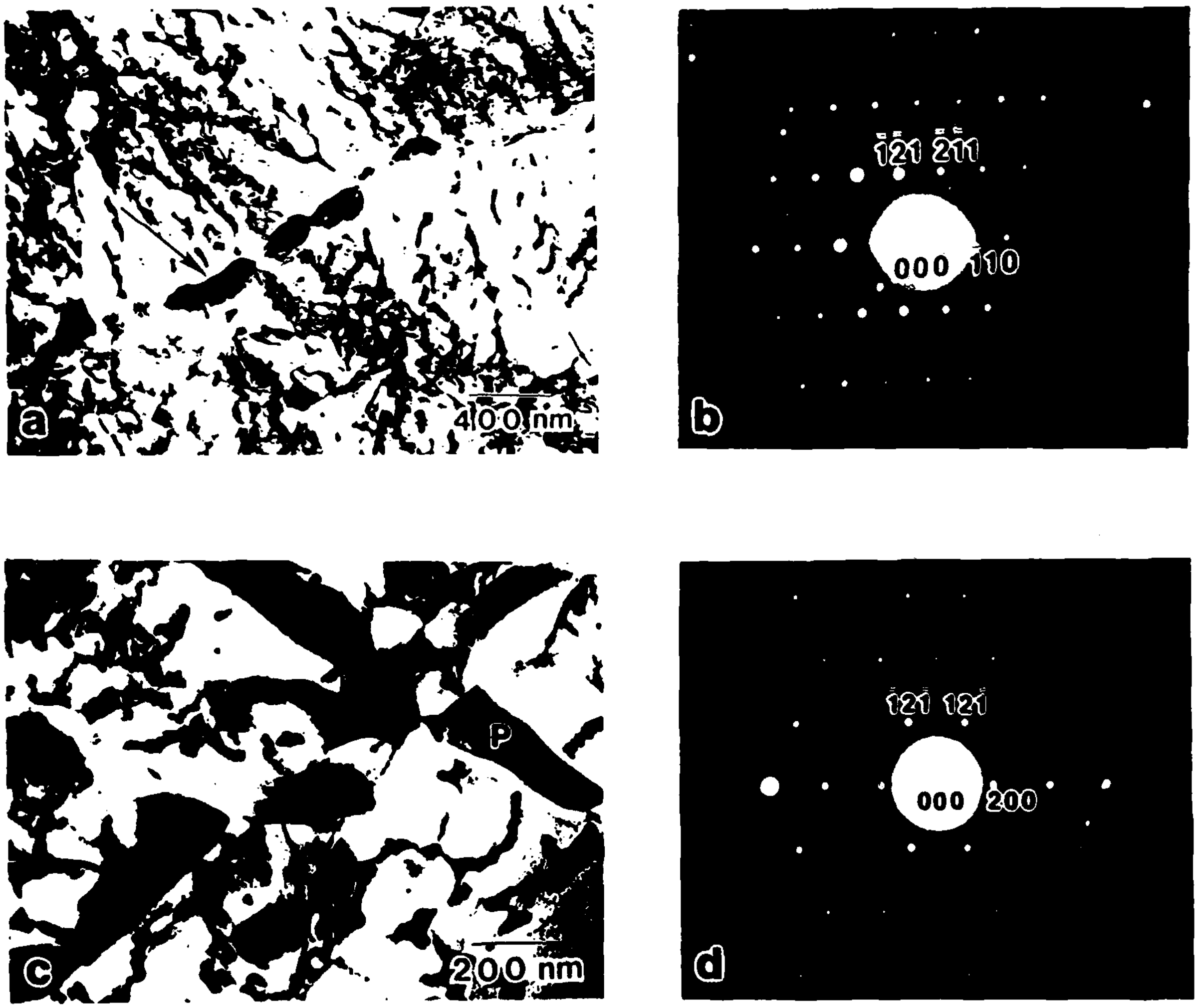
a
400 nm
b
$\bar{1}\bar{2}1$ $\bar{2}1\bar{1}$
000 $\bar{1}10$
c
P
200 nm
d
$\bar{1}2\bar{1}$ $12\bar{1}$
000 200

Figure 2. Al-8Fe-2Mo alloy ribbon aged at 450°C for 0.25 hrs. a) BF micrograph; b) [113] SAD pattern of precipitate indicated by arrow in "a"; c) BF micrograph from thicker area; d) [012] SAD pattern from precipitate labelled P in "c".

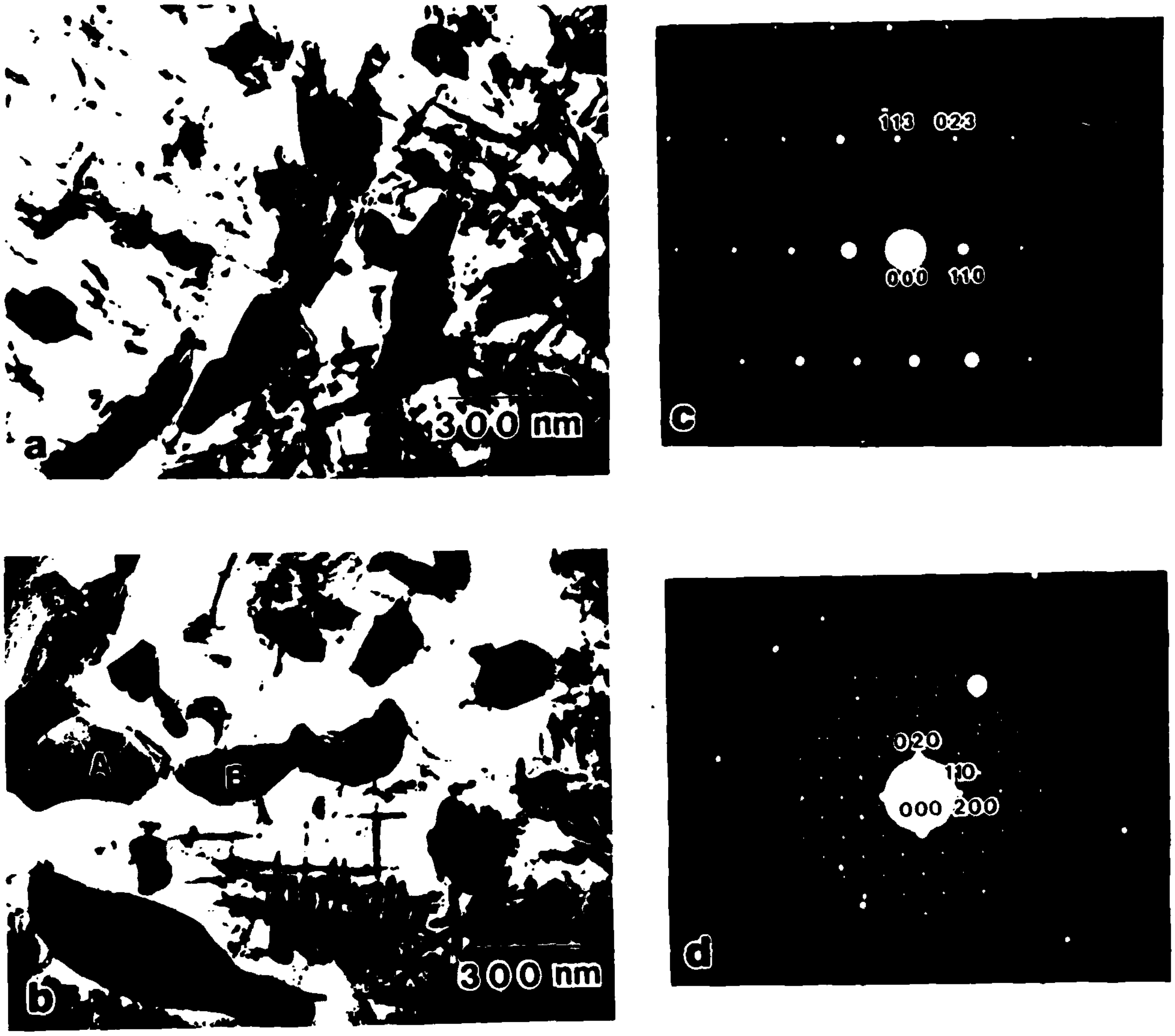
a
300 nm
c
1̄13
023
000
110
b
A
B
300 nm
d
020
110
000
200

Figure 3. Al-8Fe-2Mo alloy ribbon aged at 450°C for 4 hrs. a), b) BF micrographs; c) $[3\bar{3}2]$ and d) [001] SAD patterns of $Al_6(Fe,Mo)$ and $Al_p(Fe,Mo)$ precipitates labelled A and B, respectively in "b".

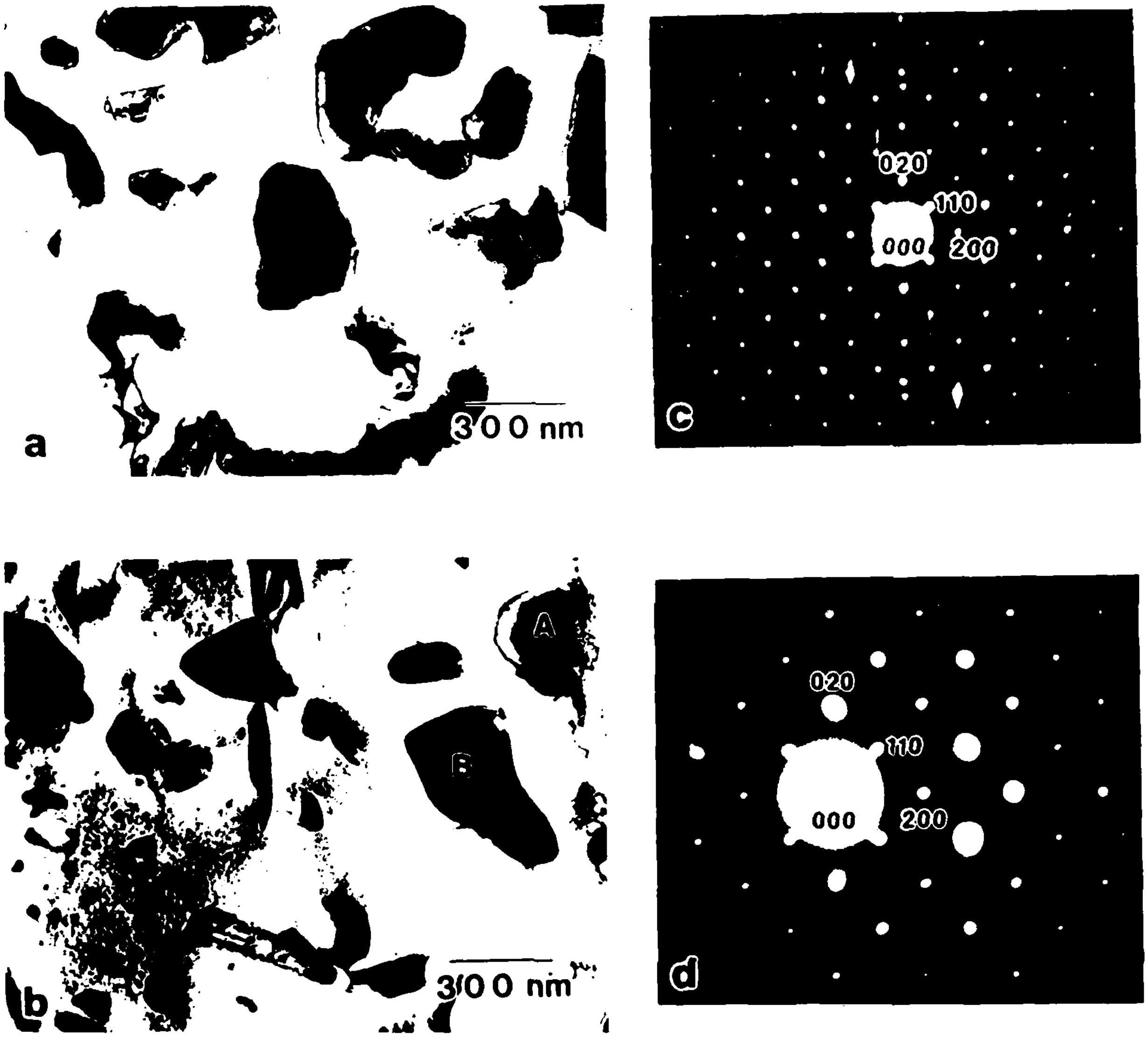

a
300 nm
c
020
110
000
200
A
B
b
300 nm
d
020
110
000
200

Figure 4. Al-8Fe-2Mo alloy ribbon aged at 450 °C for 50 hrs. a) BF micrograph showing $Al_x(Fe,Mo)$ precipitates; b) BF micrograph showing the $Al_x(Fe,Mo)$ (labelled A) and the $Al_{12}Mo$ (labelled B) phases; c), d) [001] SAD patterns of the precipitates labelled A and B in "b".

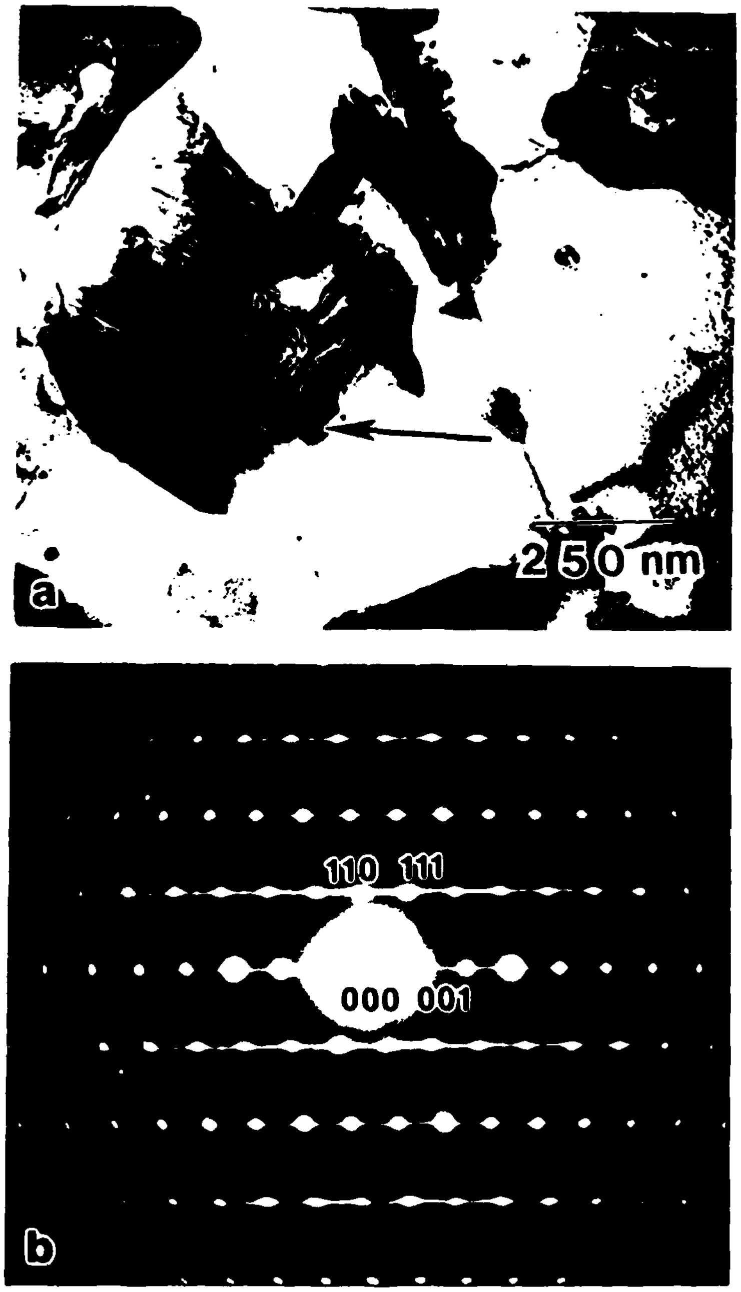
250 nm
a
110
111
000
001
b

Figure 5. Al-8Fe-2Mo alloy ribbon aged at 450°C for 50 hrs. a) BF micrograph showing the monoclinic Al$_3$Fe phase (see arrow); b) [$\bar{1}$10] SAD pattern.

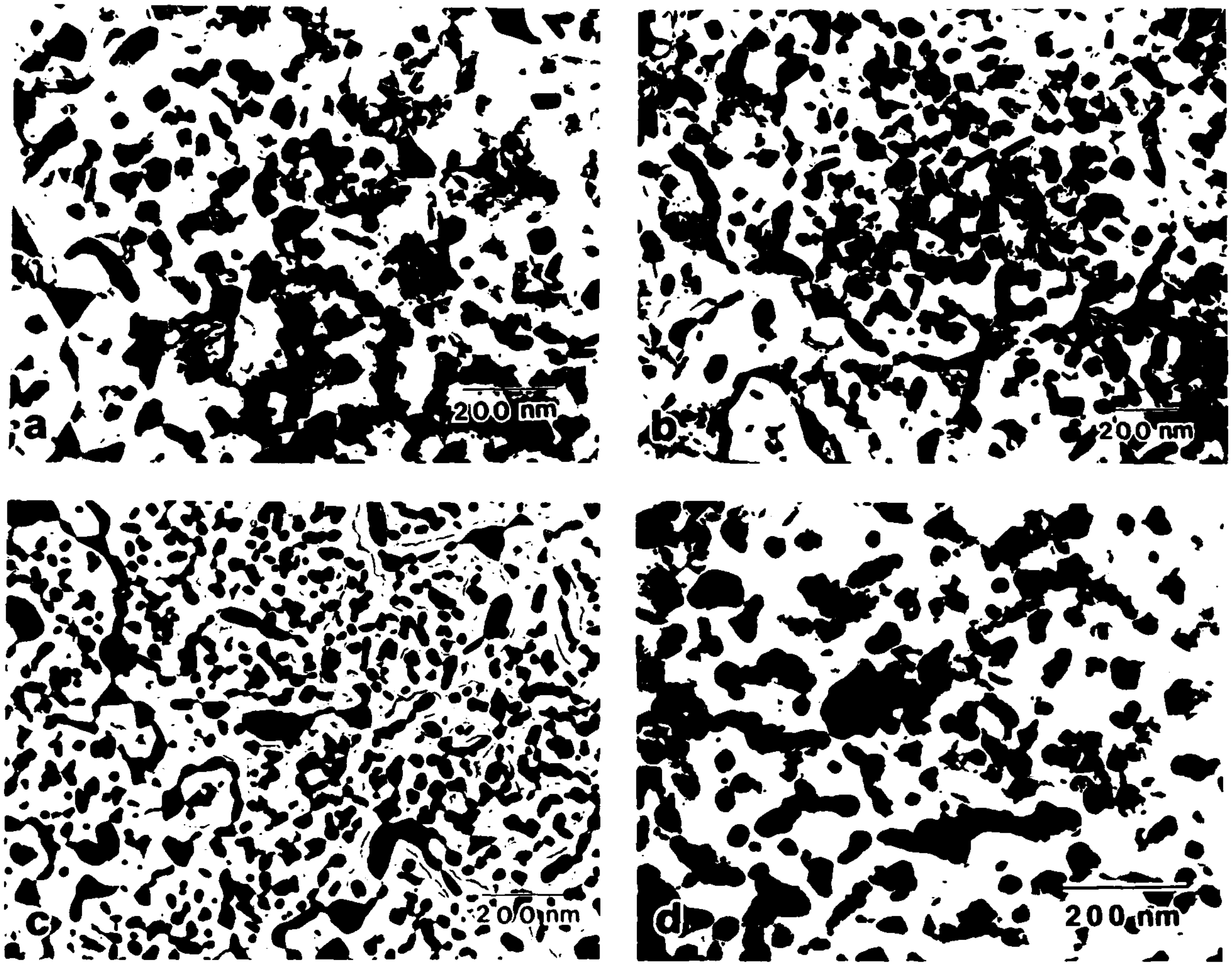
a
200 nm
b
200 nm
c
200 nm
d
200 nm

Figure 6. BF micrographs of Al-8Fe-2Mo-Si alloy ribbons aged at 450°C. 0.5 wt.% Si alloy—a) 0.25 hrs; b) 4 hrs; c) 50 hrs; d) 1 wt.% Si alloy, 50 hrs.

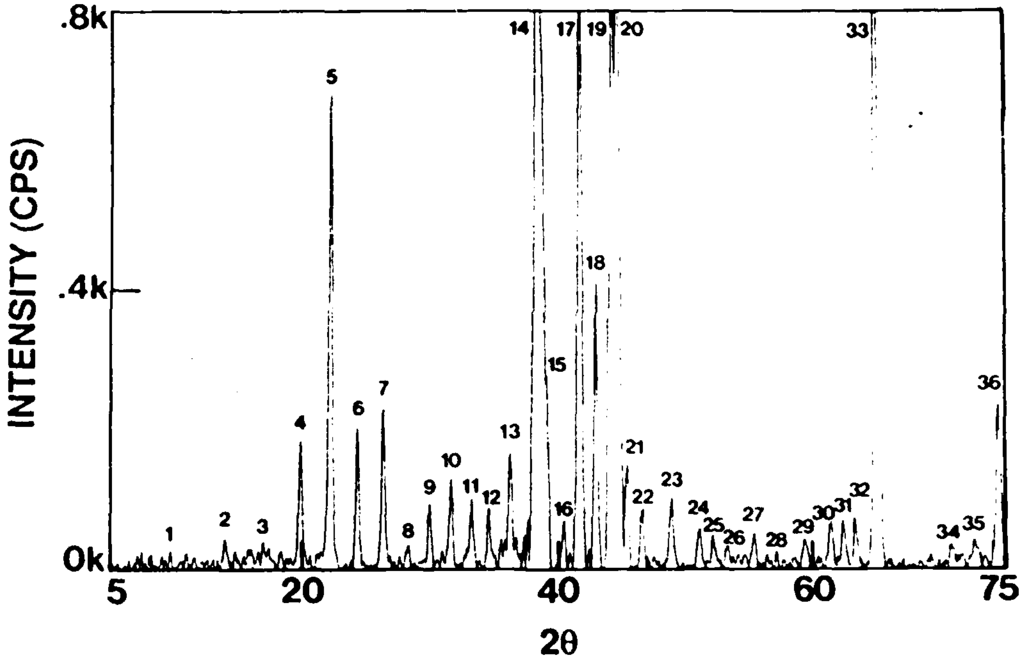

Figure 7. Variation of intensity as a function of 2θ for the 1 wt.% Si alloy heat-treated at 450°C for 50 hrs.

TABLE I

Summary of X-ray Diffraction Results

Peak No.	2θ	Intensity (cps)	I/I_o ppt.	hkl	d, nm	a_o, nm
1	9.80	170	10	110	0.902	1.275
2	13.98	167	9	200	0.633	1.266
3	17.10	162	9	211	0.519	1.269
4	19.86	312	17	220	0.447	1.264
5	22.24	808	45	310	0.399	1.263
6	24.38	315	17	222	0.365	1.264
7	26.40	330	18	321	0.337	1.262
8	28.30	116	6	400	0.315	1.261
9	30.02	178	10	330/411	0.297	1.262
10	31.70	221	12	420	0.282	1.261
11	33.28	194	11	332	0.269	1.262
12	34.60	182	10	422	0.259	1.269
13	36.28	295	16	431/510	0.248	1.262
14	38.46	18837	---	111 Al	0.234	0.405
15	39.04	511	28	521	0.231	1.263
16	40.44	236	13	440	0.223	1.261
17	41.72	1287	71	433/530	0.216	1.261
18	43.00	594	33	600	0.210	1.261
19	44.24	1811	100	532/611	0.205	1.261
20	44.70	3094	---	200 Al	0.203	0.406
21	45.42	335	19	620	0.200	1.262
22	46.64	210	12	541	0.195	1.261
23	48.94	208	12	631	0.186	1.262
24	51.20	160	9	550/543/710	0.178	1.261
25	52.26	145	8	640	0.175	1.261
26	53.34	119	6	552/633/712	0.172	1.261
27	55.46	142	8	730	0.166	1.261
28	57.22	132	7	651/732	0.161	1.266
29	59.40	136	8	554/741	0.156	1.263
30	61.46	170	9	653	0.151	1.261
31	62.44	180	10	660/822	0.149	1.261
32	63.40	182	10	743/750/831	0.147	1.261
33	65.10	1260	---	220 Al	0.143	0.405
34	70.84	126	7	754/851	0.133	1.261
35	72.56	139	8	763	0.130	1.262
36	74.42	363	20	770/853/941	0.127	1.261

Average $a_o = 1.263 \pm 0.003$ nm

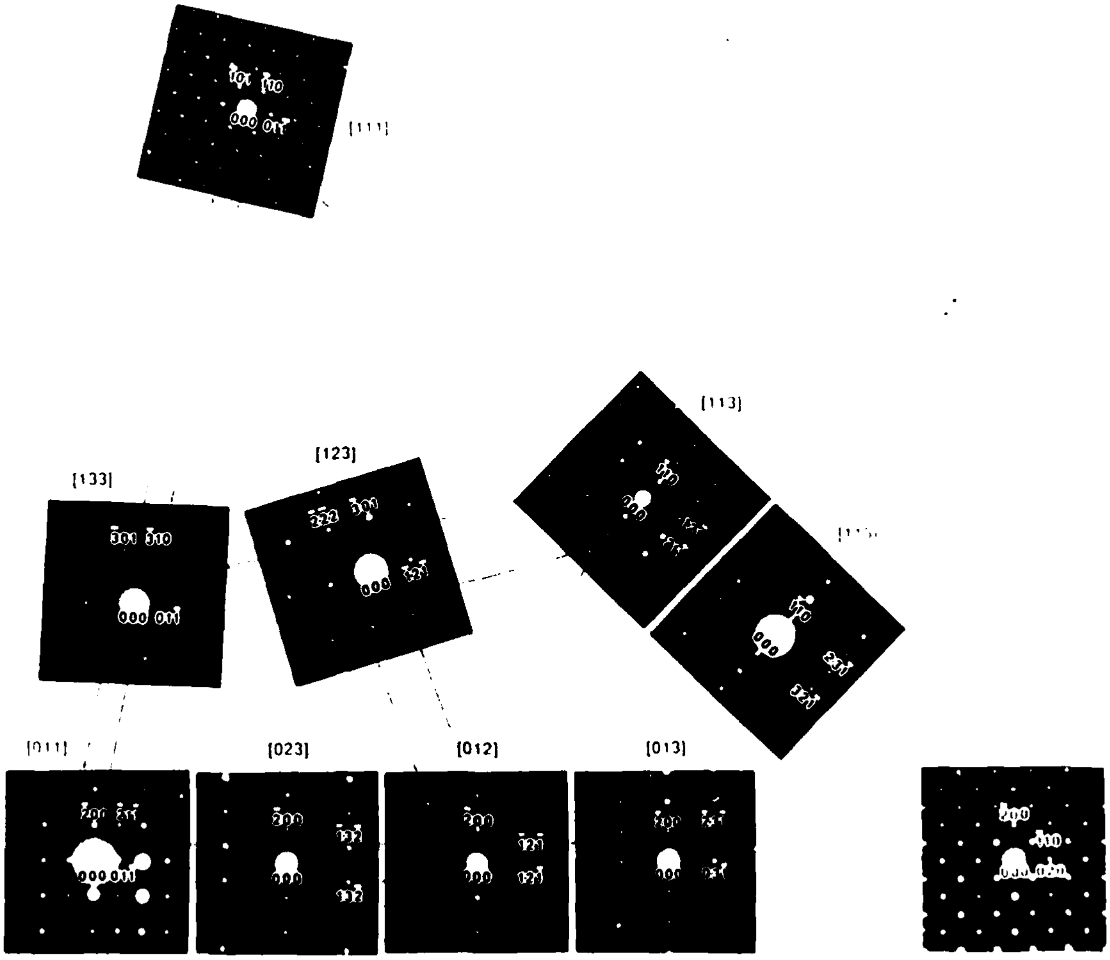
[111]
[133]
[123]
[113]
[011]
[023]
[012]
[013]

Figure 8. Examples of electron diffraction patterns recorded from individual precipitates.

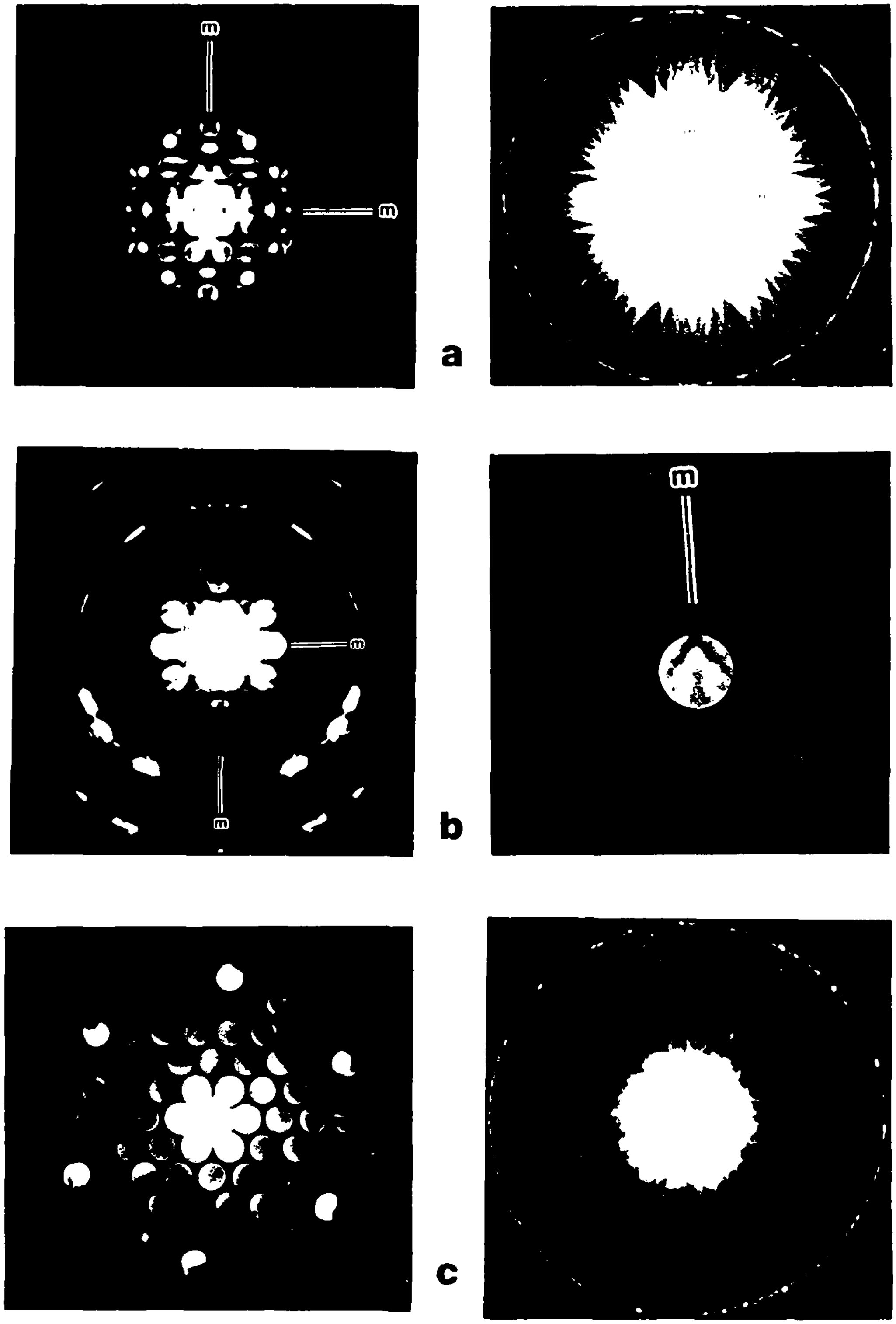

Figure 9. CBED patterns taken from precipitates. a) [001] showing 2mm projection and whole pattern symmetries; b) [023] showing 2mm projection symmetry and m whole pattern and bright field symmetries; c) [111] showing 6 and 3 projection and whole pattern symmetries, respectively.

TABLE 2

Observed Symmetries and Deduced Diffraction Groups

Zone Axis	Observed Symmetry			Deduced Diffraction Group
	Projection	Whole Pattern	BF	
[001]	2mm	2mm	—	2mm or $2mm1_R$
[023]	2mm	m	m	$2_R mm_R$
[111]	6	3	—	6_R

TABLE 3

Possible Point Groups Corresponding to the Deduced Diffraction Groups

Deduced Diffraction Groups	Possible Point Groups											
2mm		mm2					6m2					
$2mm1_R$			mmm			4mmm		6/mmm			m3	m3m
$2_R mm_R$	2/m		mmm		4/m	4mmm		6/mmm	3m	6m	m3	m3m
6_R				3							m3	

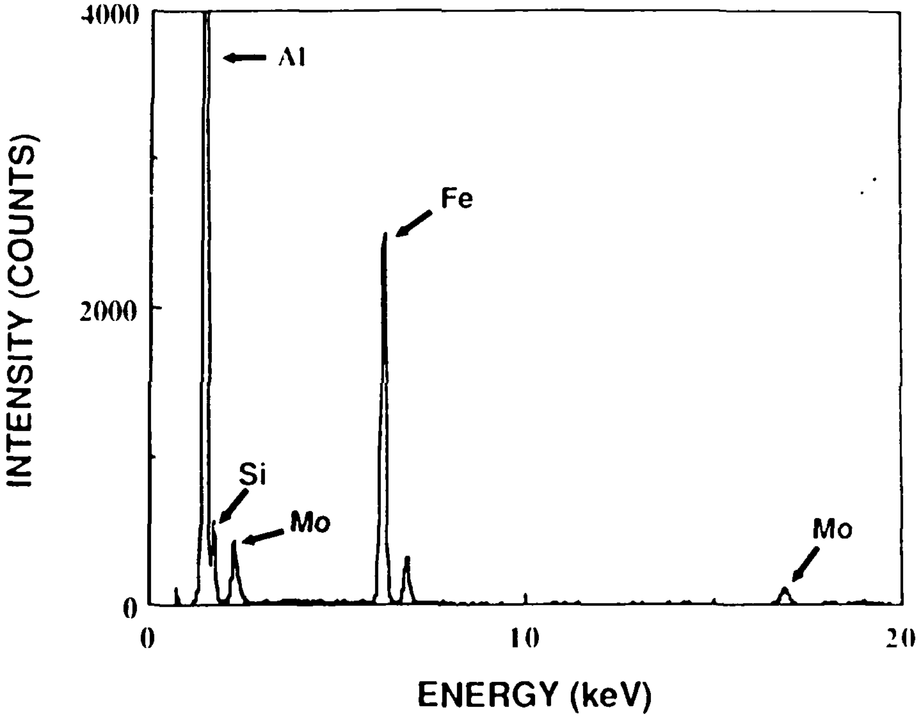

Figure 10. Typical EDX intensity spectrum taken from precipitates in the 0.5 wt.% Si alloy heat-treated at 450°C for 50 hrs.

TABLE 4

Composition of the Cubic α-AlFeSi Compound

	This Study								Phragmen (ref. 12)	
	0.5 wt.%Si Alloy				1.0 wt.% Si Alloy					
	wt.%		at.%		wt.%		at.%		wt.%	at.%
Al	62.1		75.9		62.6		75.5		62.5	75.0
Fe	29.6		17.5		28.1		16.4		31.9	18.5
		} 33.4		} 18.8		} 31.5		} 17.6		
Mo	3.8		1.3		3.4		1.2		—	—
Si	4.5		5.3		5.9		6.9		5.6	6.5

3.2 Mg-Gd Alloys

Mg-Gd alloys show promise for use in applications requring lightness and low density. Although the mechanical properties of Mg-RE alloys have been investigated, no attempts have been made to correlate these with the microstructure. Therefore, a study of the microstructures and mechanical properties of Mg alloys containing 10 and 20 wt.% Gd was undertaken, results of which are reported in the following.

Solution-Treated and Aged Alloys

An optical micrograph of the microstructure of Mg-20 wt.% Gd solution treated at 532°C for 12 hours followed by an oil quench is shown in Figure 11. Note that the microstructure is single phase. Numerous specimens of the solution treated material were aged at different temperatures and times to develop aging curves from which the optimum heat treatment conditions producing the largest increase in microhardness was determined. The results of the study are plotted in Figure 12. The hardness of alloy specimens aged at 200°C *increased slowly and leveled off after a hardness increase of* ≈10%. Specimens aged for two hours at 300°C exhibited the maximum increase in the microhardness after aging.

TEM examination of the heat treated specimens was conducted to determine the identity and precipitation sequence in the Mg-Gd alloys. In the case of Mg-20 wt.% Gd alloy specimens aged for twelve hours at 200°C to peak hardness, an essentially single phase microstructure was observed, although precipitates had formed along dislocations and grain boundaries within the matrix (Figure 13). SAD patterns obtained from the supersaturated matrix contained diffuse reflections located between the primary reflections (Figure 14 a&b), consistent with ordering in the matrix. The superlattice reflections were slightly elongated in a direction parallel to the basal plane of Mg. The reflections correspond to a g-vector of magnitude exactly one half of the matrix reciprocal lattice vector $10\bar{1}0$ and lie in the direction of this vector. It follows that the phase which forms as a result of ordering has a hexagonal lattice with a lattice parameter a equal to 6.43Å, (i.e.twice that of the initial solid solution). The value determined from SAD patterns was determined to be 6.49Å. The lattice parameter in the c direction of the ordered phase was found to equal the Mg a lattice parameter, 5.2Å. Simulations of the diffraction patterns shown in Figure 14 a&b are presented in Figure 14 c&d. This ordering behavior is similar to that observed in Mg-Dy alloys and is the ordering reaction observed in Mg_3Cd alloys[16]. The phase formed on ordering is of the type Mg_3Cd (DO19)[17].

Aging at a higher temperature produced a precipitate with a different morphology

(Figure 15). The precipitates formed within specimens aged at 300°C for 2 hours were ellipsoid shaped and measured ≈500Å in diameter and ≈4000Å along their major axes. These precipitates were also present in alloy specimens aged at 350°C for 0.5 hours. Diffraction patterns obtained from the matrix which contained this phase could not be indexed according to known phases. The new diffraction pattern may be indexed if an orthorhombic unit cell is assumed for the precipitate phase. Other diffraction patterns may also be indexed using the orthorhombic cell for the precipitate. The lattice parameters of the orthorhombic phase formed during decomposition were determined to be **a** = 22.24Å, **b** = 6.42Å, and **c** = 5.21Å. The value of the **c** parameter of the orthorhombic phase was found to be identical to that of Mg, and the value of the **a** parameter is the same as the lattice parameter of the equilibrium phase. A diffraction pattern obtained with the beam parallel to $[0001]_{Mg}$ and $[001]_{ppt}$ and a computer simulation of the pattern is presented in Figure 16. Note that the diffraction spots are elongated (spiked) in Figure 16. This spiking may result from a combination of lattice strain and geometry of the precipitate phase. The orientation relationship between the matrix and precipitate is given by $[0001]_{Mg}$ // $[001]_{orth\ ppt}$ and $(10\bar{1}0)_{Mg}$ // $(100)_{orth\ ppt}$. There are three variants possible with this relationship, and three variants of the orientation relationship between the precipitate and the matrix are observed. Aging the orthorhombic phase for times longer than 8 hours at 300°C transformed the structure into the equilibrium precipitate.

The precipitates formed within the matrix after aging for 2 hours at 350°C had a different crystal structure than those produced during aging at lower temperatures. The precipitates were long and thin, and their long direction was parallel to the c-axis of the Mg matrix (Figure 17). The crystallographic aspects of these precipitates were discussed in the report of the first year's work. CBED patterns obtained from the precipitate phase were identical to those obtained from the intercellular intermetallic in the as-cast material. Therefore, it was determined that this phase was the equilibrium phase $Mg_{24}Gd_5$. The interfaces between the matrix and precipitate phase were incoherent, but SAD patterns showed that there was an orientation relationship present between the matrix and the $Mg_{24}Gd_5$ platelets. The orientation relationship is $[0001]_{Mg}//[011]_{Mg_{24}Gd_5}$ and $(\bar{2}110)_{Mg}//(1\bar{1}1)_{Mg_{24}Gd_5}$. Diffraction patterns from several different poles obtained with only one platelet located within the diffraction aperture are shown in Figure 18. An actual and simulated $[0001]_{Mg}$ diffraction pattern is shown in Figure 19. Note that only every other precipitate spot is shown. This is due to limitations of our present computer simulation, not an error in the structural determination of the phase.

According to the theory described by Cahn and Kalonji,[18] six different varients of the orientation relationship between phases with this relationship are expected. From observation, only three variants are seen. Careful examination of the precipitates revealed the presence of interfaces within the precipitates (Figure 20). Diffraction patterns obtained from the matrix of these precipitates are consistent with those observed in twinned material. The twinning behavior is consistent with a Type I fcc twin, with a $\{111\}$ twin plane and a $[11\bar{2}]$ twin direction.

Further aging of the specimens resulted in coarsening of the precipitates, but the crystal structure of the phase remained unchanged. The phase precipitated on the grain boundaries was identified by CBED as $Mg_{24}Gd_5$. An orientation relationship was not observed between the intermetallic and either of the two adjacent grains.

Mechanical Behavior

Mechanical test specimens of Mg-10 and 20 wt.% Gd after various heat treatments were tested at room temperature and 200°C. The results of the tests are tabulated in Table 5. The ductility of the samples was quite dependent on the concentration of Gd in the alloys. There was no set of conditions where an alloy containing 20 wt.% Gd was more ductile than a more dilute alloy. In fact, the best combination of properties for the Mg-20 wt.% Gd alloys was observed in the as-cast condition. The grain size in these alloys was small, therefore many grains were favorably oriented for slip. The ductility of these α-Mg grains was large since very few precipitates were present within the matrix. The heat treated alloys had acceptable strengths at temperature, yet their ductilities were only 1 or 2%. The grain size in these alloys was very large due to grain growth during solution-treatment. The combination of large grain size and an unfavorable precipitate morphology would produce the poor ductilities observed in this material after heat treatment. The Mg-10 wt.% Gd alloys had a much better combination of tensile properties. Note that although the decrease in the Gd content of the alloy lowered the yield strength of the as-cast material, the ultimate strength and ductility were higher. This was attributed to the microstructure of the dilute alloys, which contained much less grain boundary intermetallic phase. Solution-treating and aging this alloy did not noticeably improve either of the tensile properties, although the ductility of the aged specimens was much improved in all test conditions for all specimens. Again this may be related to the microstructure. Figure 21 shows the matrix of a specimen before and after mechanical testing. The heat treat conditions involved a solution treatment for 8 hours at 535°C, followed by an oil quench, and subsequently the specimens were aged for 2 hours at 300°C. Energy dispersive x-ray analysis of thin foils shows the presence of Gd in the matrix, and very fine precipitates are apparent in the matrix. The diffraction patterns obtained from the matrix correspond to the formation of a ordered Mg_3Cd-type precipitate in the matrix. In the 20 wt.% Gd much larger orthorhombic precipitates are observed in this heat-treated condition. The thermal stability of the tensile properties of the 10 wt.% Gd alloys were excellent. The alloys retained on average 91% of their room temperature yield and ultimate strenght at 200°C. The ductility of the alloys was doubled by the increase in test temperature. This may be caused by the activation of pyramidal slip systems which operate at elevated temperatures, and an increase in thermally activated cross slip of basal dislocations onto adjacent slip planes. This has been observed in other alloy systems when tested at these temperatures.[19]

In an attempt to refine the grain size and improve ductility further, specimens of the 10 wt.% Gd alloy were solution-treated at 525°C rather than 535°C. At this lower temperature it was hoped that grain growth would be inhibited and the grain size of the solutioned specimens would be finer. The lower temperature reduces the driving force for grain growth after recrystallization. The grain size after this heat treatment was indeed reduced, from ASTM 3.7 to ASTM 4.8. The specimens were aged at the same temperature to produce identical precipitate distributions within the matrix. As can be observed in Table 5, the tensile properties were largely unaffected, while the ductility of the alloy was improved by about 12%. This result would be expected since the ductility of Mg is highly dependent on the grain size.[20]

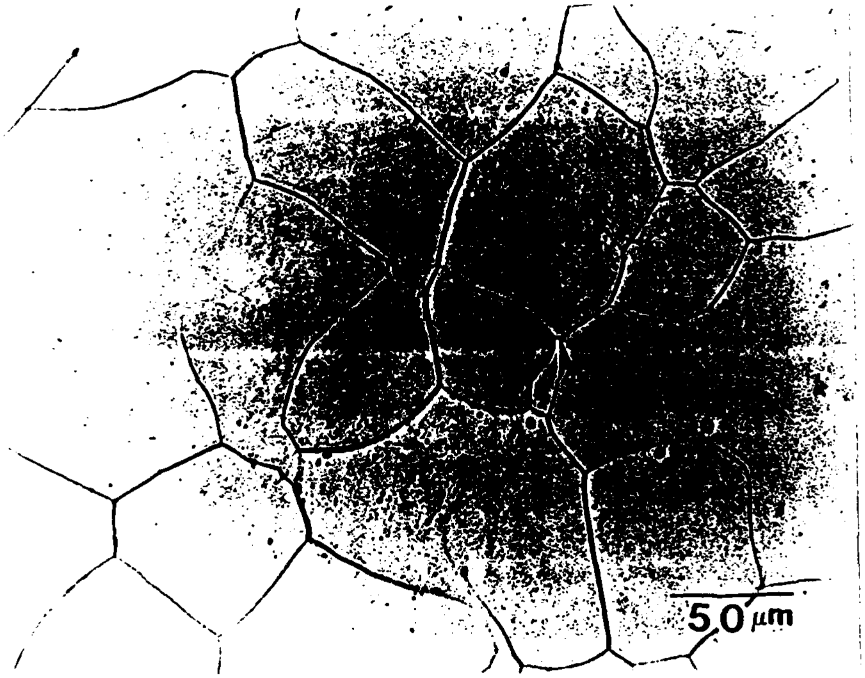

Figure 11. Optical micrograph of Mg-20wt.% Gd solution treated at 532°C for 12 hours.

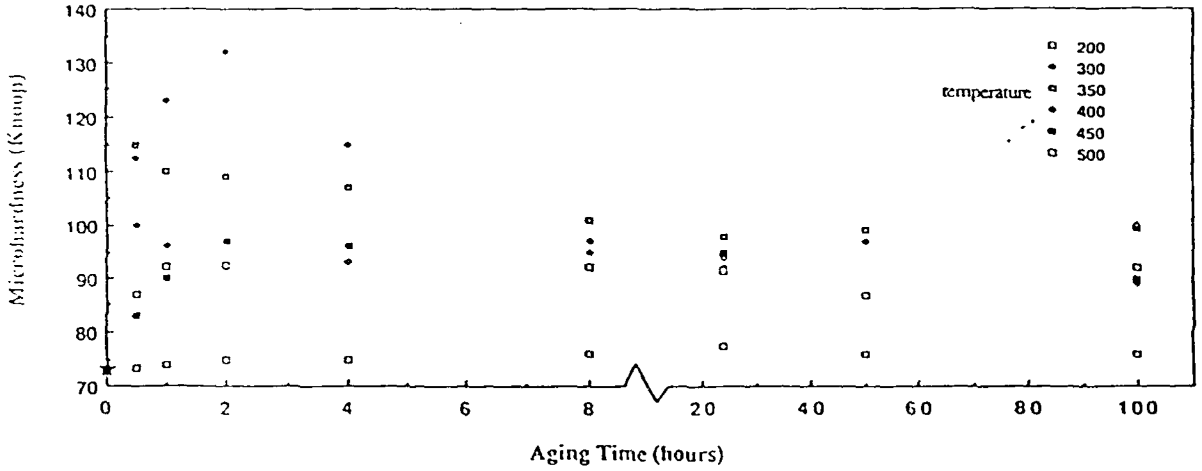

Figure 12. Knoop microhardness (50 gram load) of Mg-20wt.% Gd aged for various times and at different temperatures.

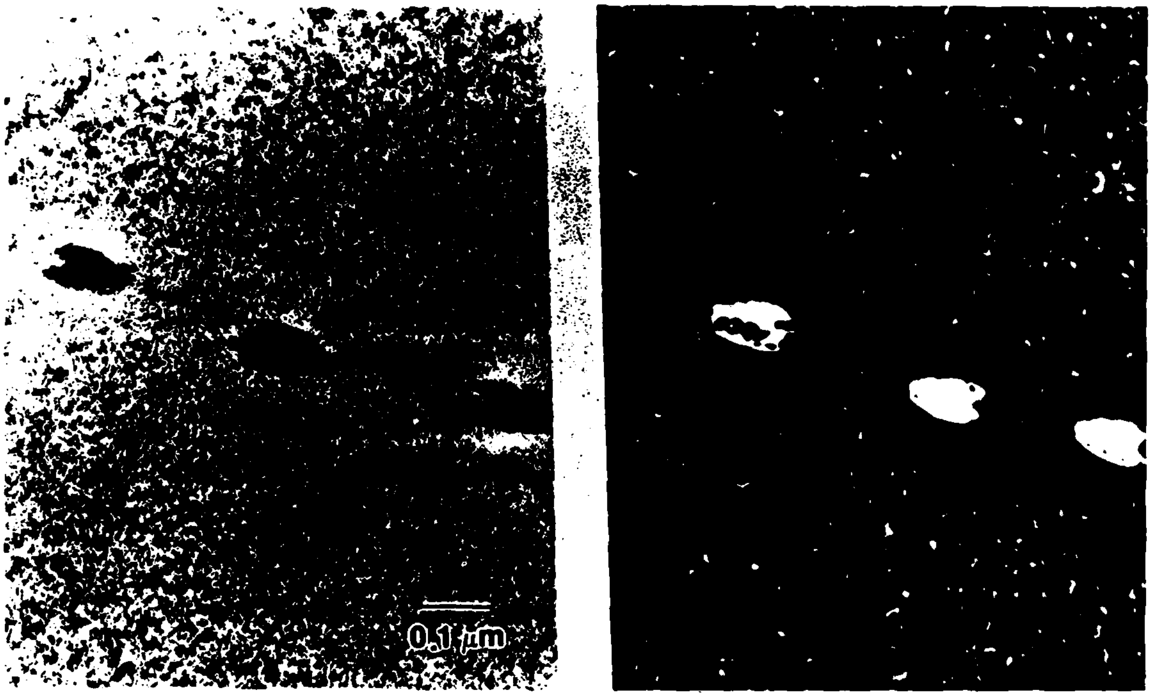

Figure 13. Precipitates present within the matrix and along dislocations after aging solution-treated Mg- 20wt.% Gd for 12 hours at 200°C.

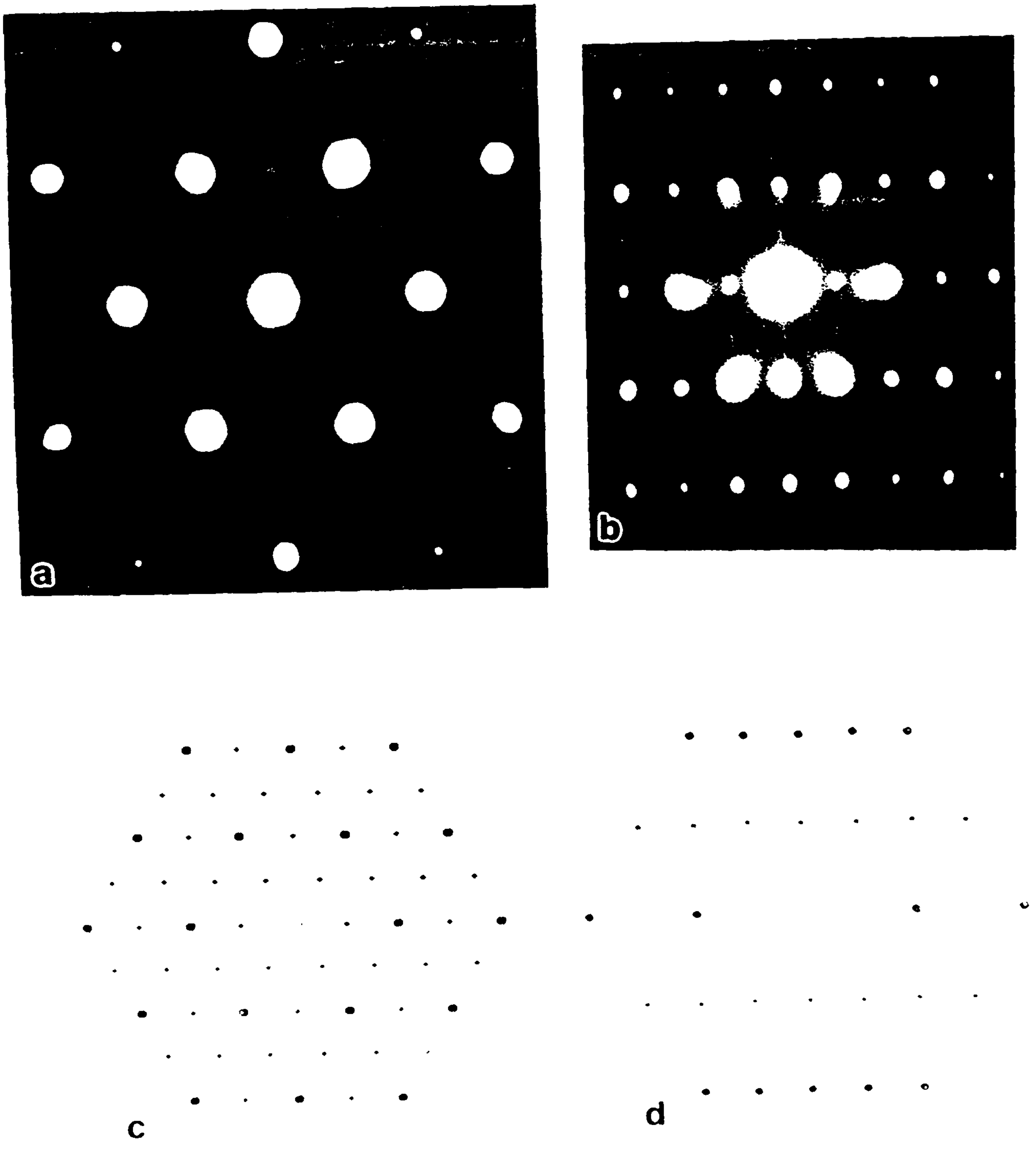
a
b
c
d

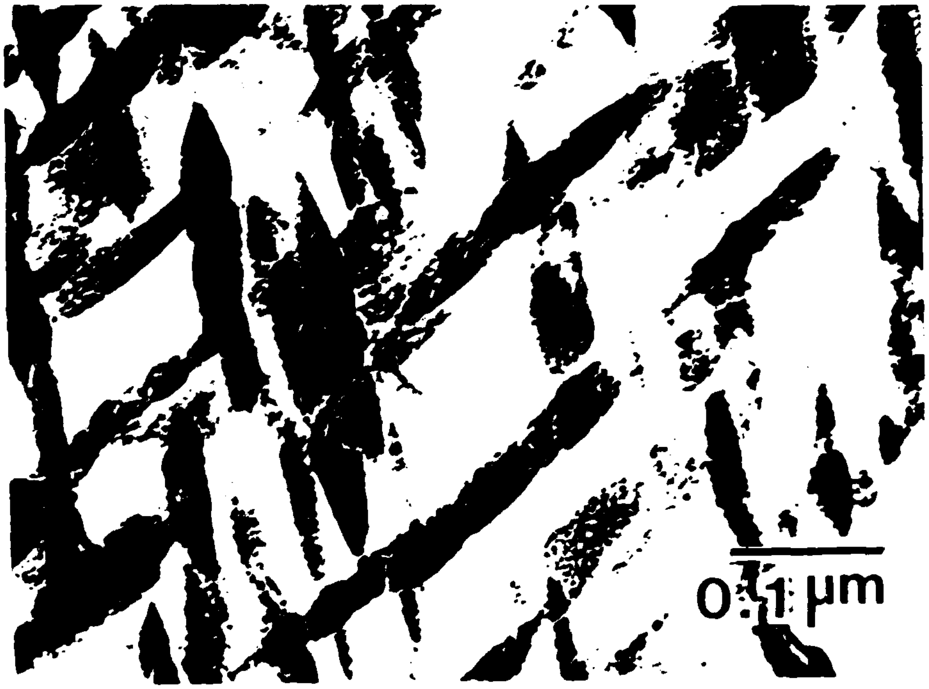

Figure 15. TEM micrograph of the precipitates observed in solution treated Mg-20wt.% Gd aged for 2 hours at 300°C

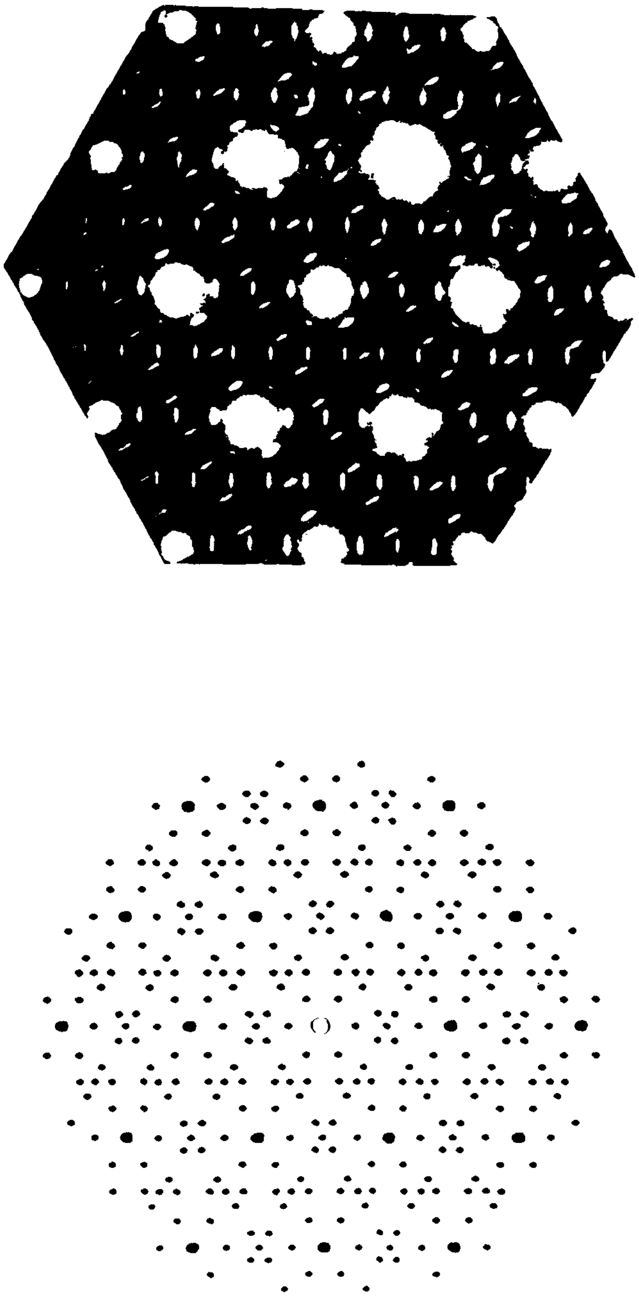

Figure 16. Diffraction pattern obtained with the beam parallel to [0001]Mg in Mg-20wt.% Gd aged for 2 hours at 300°C. A computer simulation of the pattern is also included.

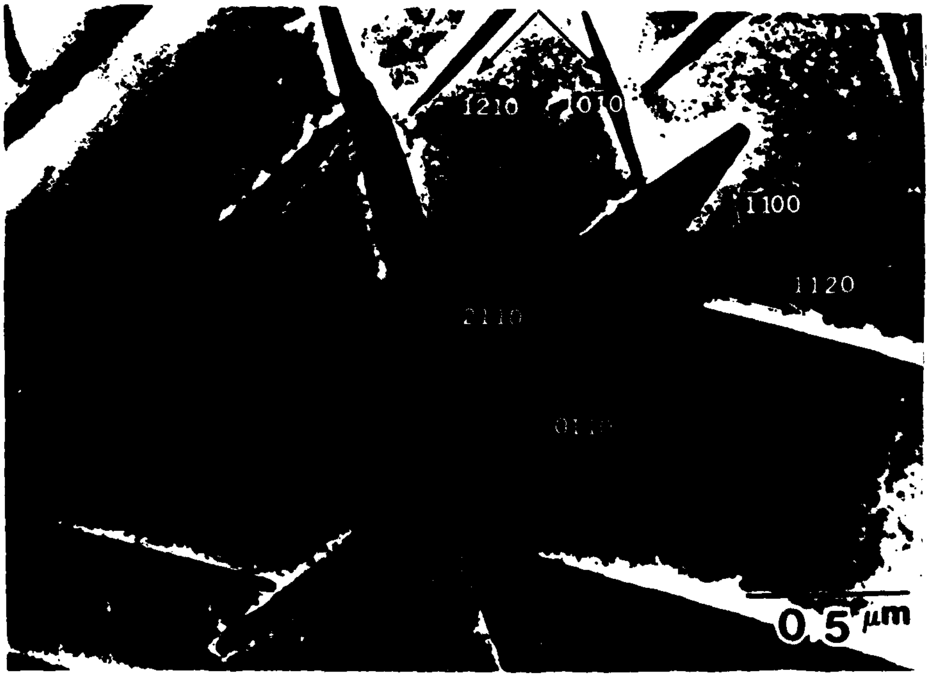
1210
1010
1100
1120
2110
0110
0.5 µm

Figure 17. Precipitates present in the matrix of Mg-20wt.% Gd solution treated and aged for 2 hours at 350°C.

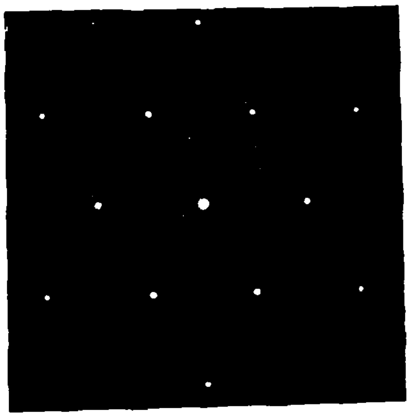

[0001] Mg

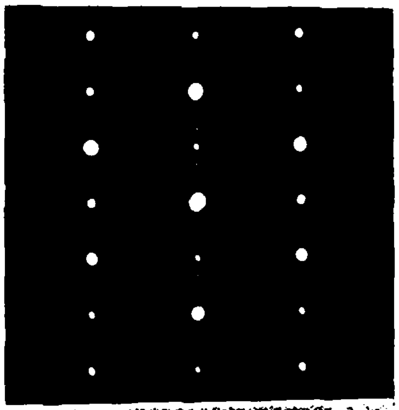

[1$\bar{1}$20] Mg

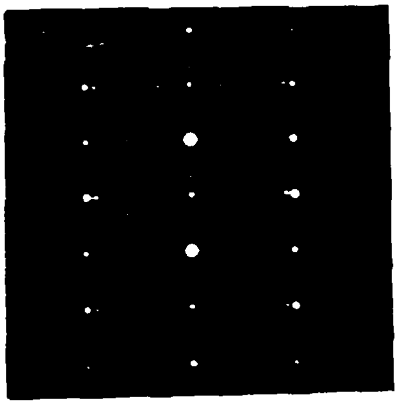

[1$\bar{2}$10] Mg

Figure 15. SAD patterns obtained from several poles and precipitates. Only a single precipitate used at a time

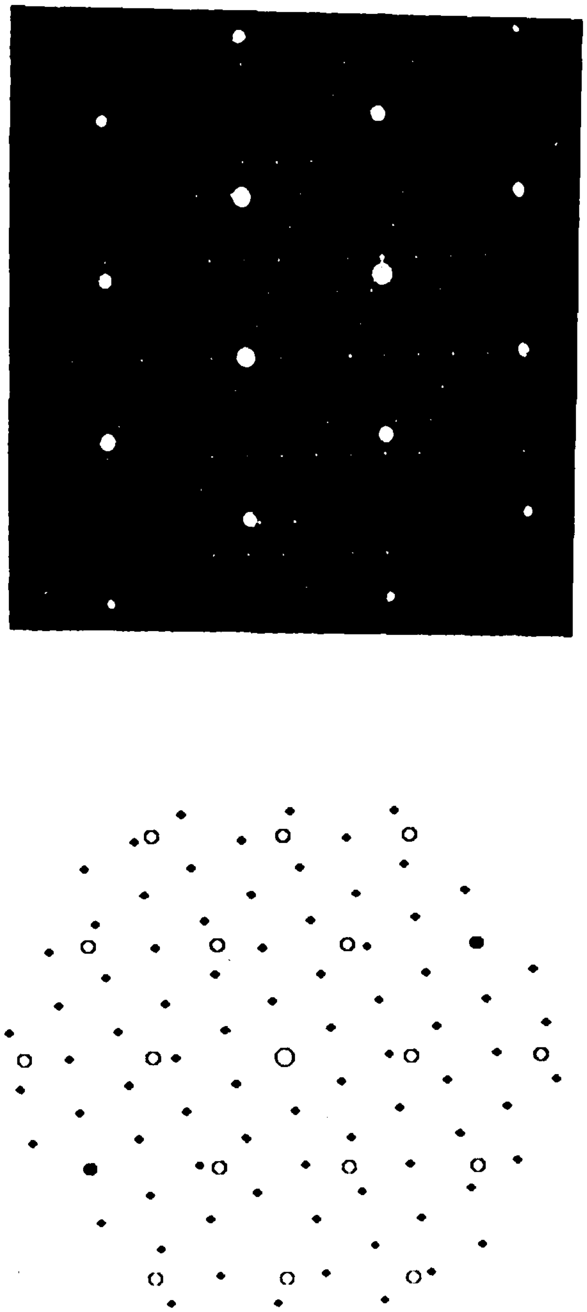

Figure 19. Actual and simulated SAD patterns for $Mg_{24}Gd_5$ precipitates in a Mg matrix.The beam direction is [0001]Mg and [011]ppt. Due to computer limitations, only every other precipitate reflection is shown.

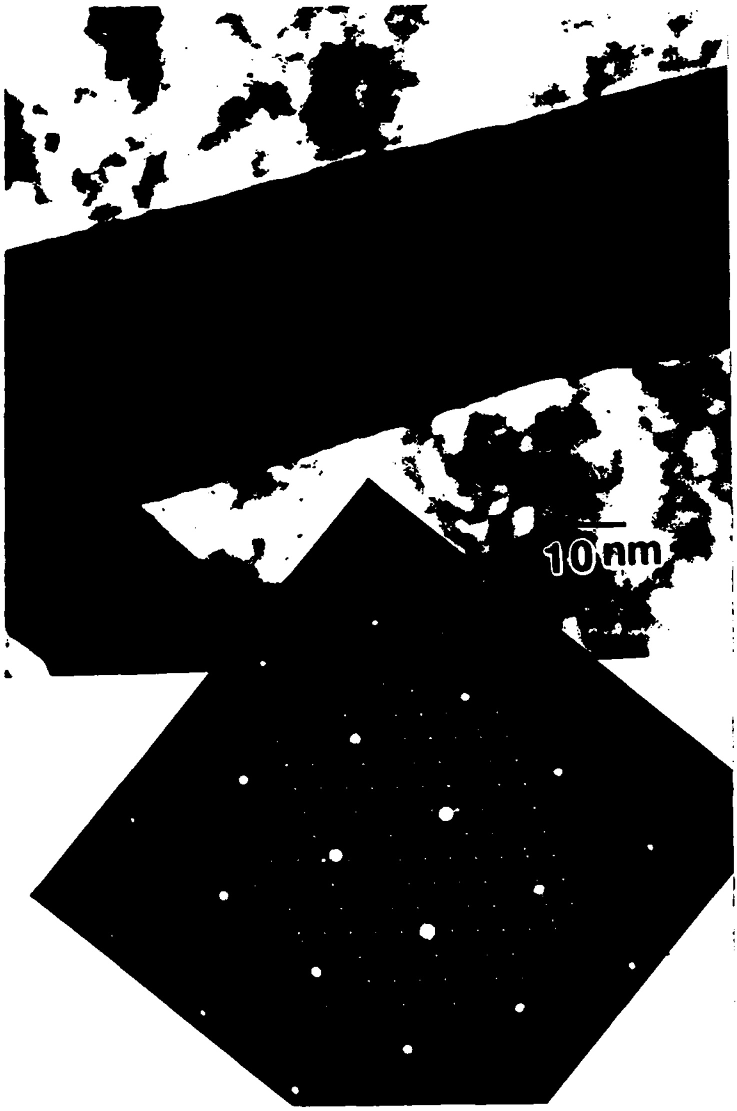

Figure 20. Micrograph showing evidence of twinning in several of the $Mg_{24}Gd_5$ precipitates.

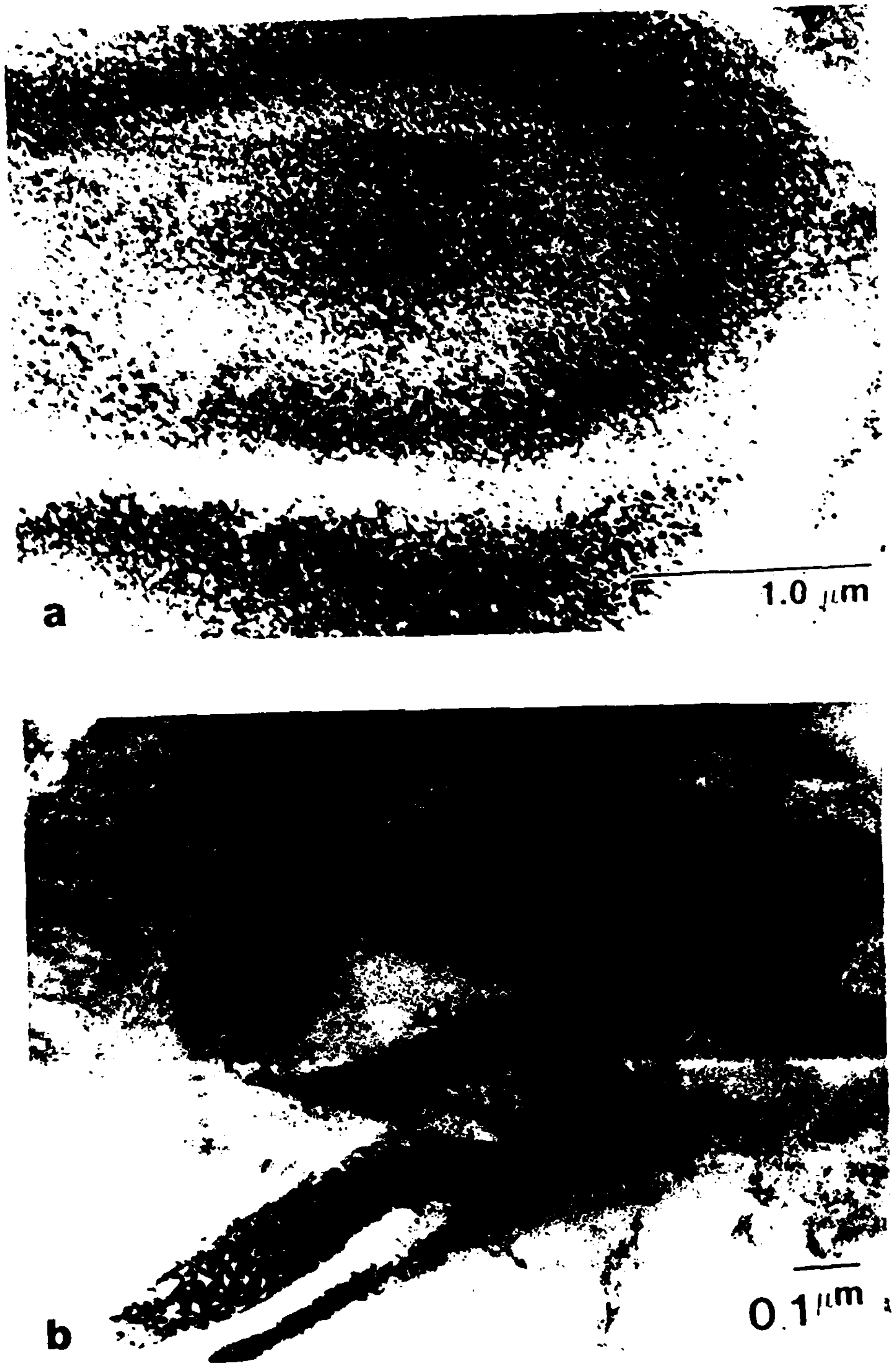

Figure 21. Microstructure of Mg-20 wt.% Gd before and after tensile testing. The alloy was solution treated at 300°C for 2 hours and tested at 25°C. a) Before testing; b) After testing.

TABLE 5

Tensile data for Mg-Gd alloys after different heat treatments

Alloy	Condition	Test Temp (°C)	0.2%Y.S. MPa (Ksi)	U.T.S. MPa (Ksi)	e_f
Mg-20wt%Gd	as-cast	25	136.2	154.4	3.36
	535/8/OQ	25	72.3	157.0	7.47
	535/8/OQ	25	fol	214.3	0.05
	300/2/FC	200	81.2	212.3	1.74
	535/8/OQ	25	fol	139.6	0.052
	350/2/FC	200	82.5	195.0	0.94
Mg-10wt%Gd	as-cast	25	88.3	176.6	7.6
	535/8/OQ	25	*	*	*
	535/8/OQ	25	97.2	187.4	11.6
	300/2/FC	200	68.8	167.1	22.05
	535/8/OQ	25	83.0	174.7	9.35
	350/2/FC	200	85.4	165.9	19.64
	525/8/OQ	25	92.3	168.1	10.3
	300/2/FC	200	86.3	159.0	25.5

* Inclusion present at fracture surface.
fol - failed on loading
Condition legend - solutioning temp (°C)/aging time (hours)/cooling medium

3.3. Mg-Si Alloys

To model the RSP behavior of Mg-based alloys the Mg-Si alloy system was chosen. This decision was based on criteria developed during the study of RSP Al-transition metal alloys.[21] During the course of this study it was determined that with sufficient undercooling eutectic microstructures may be produced in alloys with compositions quite removed from the equilibrium eutectic composition. Since the heat content per unit volume of Mg is smaller than Al, it was hoped that larger undercoolings could be produced in the Mg alloys. The Mg-Si phase diagram contains one intermetallic compund, Mg_2Si, located between the pure elements (Figure 22). The Mg-rich side of the phase diagram is a simple eutectic between Mg and Mg_2Si located at 1.34wt%Si. In addition, the solubility of each constituent of the phase diagram in the other is negligible. RSP may improve the solubility, and any structures which form should be quite stable.

Mg-Si alloys containing Si in the range of 0.5 to 8 wt.% were prepared by induction melting and casting into a stainless steel mold.Melt spinning was used to produce rapidly solidified material because using this method the alloy melt could be superheated prior to solidification. This eliminates the possibility of unmelted silicide acting as a nucleating agent for solidification,which would limit the degree of undercooling in the melt. The microstructures of these alloys are described in the following.

3.3.1. As-Cast

Hypoeutectic alloys with compositions of 0.5 and 1.0 wt.% Si had a microstructure consisting of primary α-Mg dendrites with an interdendritic eutectic structure.The phases which comprised the eutectic were determined to be α-Mg and the intermetallic compound Mg_2Si. Hypereutectic alloys of compositions 2.0, 3.0, 4.0, 5.0, and 8.0 wt.% Si contained large, faceted crystals of Mg_2Si. The lattice parameter of the Mg_2Si compound, present as the primary phase in the latter and as one of the phases of the eutectic constituent in the former, was calculated from SAD patterns to be 6.5Å. The space group was established by CBED to be Fm3m. These results are consistent with published values for Mg_2Si (space group-Fm3m, a_0=6.338Å).

3.3.2. Melt Spun Ribbon

Microstructure

The microstructures of the 1.0 wt.% Si through 3.0 wt.% Si alloys were similar and consisted of α-Mg cells with a rod-like eutectic located at the cell boundaries . In the 1.0 wt.% Si MSR, the eutectic comprised of individual rods located between adjacent α-Mg cells. The rods were identified by CBED as Mg_2Si. As the Si content of the alloy was increased, the complexity of the eutectic also increased. The 3.0 wt.% Si alloy contained a branched intercellular network of Mg_2Si rods (Figure 23 a&b). The individual rods were quite small (25nm diameter), and were uniformly spaced along the cell boundary. Several of the eutectic rods had branches, analogous to secondary dendrite arms. It is important to note that although the composition of the alloy is hypereutectic and according to the equilibrium phase diagram primary Mg_2Si dendrites are expected to form during solidification, no evidence of primary Mg_2Si dendrites was seen in any of the TEM specimens from MSR.

With further increase in Si content, the amount of the eutectic progressively increased, *till at 5 wt.% Si, the entire microstructure* was composed of a refined and uniform distribution of this structure (Figure 24). Ribbons of this alloy were more resistant to cracking during bending than other alloy ribbon. The individual eutectic colonies were much larger than the cells seen in other Mg-Si melt-spun alloys. The average cell size of the alloys and in the case of the 5.0 wt.% Si alloy the colony size is tabulated in Table 9.

The morphology of the eutectic was quite uniform. The individual Mg_2Si rods were rarely branched, and were evenly distributed throughout the matrix. The geometry of the cross section of an individual rod was round, although a large number of the rods were noticeably elongated (Figure 25). This behavior has been observed in other faceted eutectics, and is attributed to asymmetic interfacial energy.[22] The inter-rod spacing, l, was uniform and an average value was found to be 16.1 nm, whereas the average diameter of the rod cross section was found to vary from 14.3 nm to 7.5 nm (average 11.7 nm).

The Mg_2Si rods showed a definite orientation relationship with the α-Mg matrix. This relationship was determined by analysis of SAD patterns and computer simulations to be $(0001)Mg \,//\, (010)Mg_2Si$ and $[01\bar{1}0]Mg \,//\, [001]Mg_2Si$. Stereographic projections (planes) for $[0001]Mg$ and $[\bar{2}110]Mg$ zone axes corresponding to this orientation relationship are shown in Figure 26. Using the method of Cahn and Kalonji,[18] it is determined that three variants of this orientation relationship are possible, each with $\langle 010 \rangle$ aligned with a different $[01\bar{1}0]$. Computer simulated diffraction patterns were produced for several zone axes. Simulations and actual diffraction patterns obtained with the electron beam aligned parallel with i) the basal plane of Mg (Figure 27); ii) the $[\bar{2}110]$Mg zone axis aligned with (100)Mg_2Si zone axis (Figure 28), and iii) the $[\bar{1}2\bar{1}0]$Mg zone axis with (0001)Mg // (020)Mg_2Si (Figure 29). Using trace analysis the direction of the long axis of the Mg_2Si eutectic rods within the matrix was determined to be aligned with the $[01\bar{1}1]$ direction of Mg. A stereogram (directions) showing this relationship and a diffraction pattern and simulation are shown in Figures 30 and 31, respectively. This relationship also corresponds to the growth direction of the eutectic rods and the matrix. As the rods deviate during solidification from this growth direction, faults form within the rod and reestablish this orientation relationship. This growth direction is not expected and presumably results from the faceted nature of Mg_2Si phase. The growth direction and orientation relationship allows alignment of the following planes; (420)Mg_2Si (d=1.417Å) and $(20\bar{2}0)$Mg (d=1.390Å) and (400)Mg_2Si (d=1.58Å) and $(11\bar{2}0)$Mg (d=1.605Å). This alignment reduces the interfacial energy of the eutectic mixture. A schematic diagram of the relationship is shown in Figure 32.

The microstructure of the 8.0 wt.% Si alloy was fundamentally different from those of the previous alloys (Figure 33). The primary solidification phase in the alloy in this condition was identified by CBED as Mg_2Si, which formed dendrites within the matrix. Each intermetallic dendrite formed the center of a solidification cell. Each cell consisted of a central region and a finely branched outer region. Presumably, the initial dendrite forms the central region, and a fine, branched dendrite structure surrounds the outer region. It is reasonable to speculate that this structure forms as the amount of undercooling in the melt increased and Mg was rejected into the melt by the primary dendrite. As the degree of undercooling increases, the stable dendrite tip radius decreases. Small perturbations on the dendrite tips become unstable and degenerate into several new dendrites. This process continues until a new metastable equilibrium is reached for the tip radius and spacing. The formation of primary Mg_2Si dendrites rather than α-Mg cells during solidification indicates that the degree of total undercooling in the melt was insufficient to permit initiation of solidification below the extended α-liquidus.

Evolution of Microstructure in Melt-spun Mg-Si Alloys

The microstructures observed in the alloys can be divided into three regimes; cellular (dendritic) based on α-Mg, coupled eutectic, and dendritic based on Mg_2Si. The formation of these microstructures may be explained using a coupled eutectic metastable Mg-Mg_2Si phase diagram (Figure 34). At compositions equal to or less than 4.0 wt.% Si, solidification proceeds in the cellular (dendritic) regime. Solidification of the 5.0 wt.% Si alloy occurs in the coupled eutectic region, and the 8.0 wt.% Si alloy solidifies in the Mg_2Si dendritic region. Using the phase diagram, the total undercooling of the melt may be estimated by assuming that the 5.0 wt.% Si alloy is undercooled to a temperature just below the extended α-liquidus, and that coupled eutectic growth occurs at that point. The total undercooling from the liquidus may then be estimated to be $\approx$150°C. Using this value as a rough estimate for the undercooling in each of the other alloys, the solidification structure of each alloy may be predicted using the metastable phase diagram. The solidification path of the initial undercooling of the alloy takes the form of a straight vertical line on the phase diagram. Once a solidification event occurs within the melt, the solidification path moves toward the metastable eutectic composition which corresponds to that degree of undercooling. The slope of this path depends on the balance between heat removal and heat generation during solidification. If the rate of heat removal is greater than that of heat generation, the trend of the path will be toward decreasing temperatures, while if the melt reheats, the trend will be toward higher temperatures. The solidification path moves toward the coupled eutectic region because the solidifying material rejects solute into the melt, increasing the melt composition. Since eutectic solidification proceeds without changing the bulk composition of the melt, the solidification path ends in that region. This behavior explains the presence of an eutectic structure at the cell boundaries of 1.0 and 3.0 wt.% Si alloys. Alloys richer in Si than the maximum metastable eutectic composition reject Mg into the melt rather than Si. In these alloys the solidification path after nucleation moves toward the left (more dilute in Si) rather than the right (richer in Si) in these alloys. This behavior, along with the effect of undercooling on the dendrite tip radius, can account for the presence of the fine eutectic located at the boundaries of the primary Mg_2Si dendrites in the 8.0 wt.% Si alloy.

Aging Response of Melt-spun Alloys

The thermal stability of the melt-spun Mg-Si alloy ribbons was studied. The microstructure of the cellular (dendritic) alloys was unchanged after two hours at 300°C, although the eutectic rods in the 3.0 wt.% Si alloys were somewhat rounded. After 100 hours at 300°C, the Mg_2Si had spheroidized. The mean particle size in the 3.0 wt.% Si alloy was measured to be 86 nm. In contrast, the microstructure of the 5.0 wt.% Si alloy showed greater stability during aging. After two hours at 300°C, the eutectic structure was still present (Figure 35). However, a small rod-free denuded zone had formed alongside the cell boundaries, and large Mg_2Si precipitates had formed at triple points between the cells. The eutectic rods were still present after 72 hours at 300°C. The individual rods had become rectangular in cross section (Figure 36 a&b), with the same crystallographic planes forming the facets as was observed in the as-spun material. The individual rods contained breaks at random intervals, but were still easily identified as rods. Further aging resulted in the formation of a dual phase microstructure consisting of α-Mg and Mg_2Si particles (Figure 37).

Directionally solidified eutectic alloys show excellent high temperature stability. The stability of a rod composite structure may be determined by the perturbation method of Lord Rayleigh. He determined the rate of breakdown of a liquid cylinder into a row of spherical droplets. The growth of these droplets follows a sinusoidial distribution with material transport controlled by capillary diffusion. Cline[23] modified the theory for solid systems. In solid systems, coarsening may occur by material transport between individual rods, and surface anisotropy may also be important. Due to the low diffusivity of Si in Mg, diffusion between rods is much slower than diffusion along the rod surface. The faceted nature of the phase in rod form and the anisotropic surface energy of the phase also affect the coarsening behavior. The sharp cusp in the surface energy as a function of orientation prevents the interface from easily deviating from the facet plane. Therefore, in faceted rods the growth of sinusoidial perturbations will not occur. In faceted materials faults and twins play an important role in the coarsening behavior of the eutectic rods. Due to surface tension, material diffuses away from the intersection point of the interface and the rod surface. The groove that forms may propagate through the rod, dividing it in two sections.

Presumably, rapid diffusion along cell boundaries and along the eutectic rod interfaces produce the denuded zone adjacent to the cell boundaries. Si atoms located near the interface diffuse toward it, and from there diffuse rapidly toward regions of lowest energy. These are usually double or triple points along the cell boundaries. Here the Si atoms form large precipitates of Mg_2Si. The difference in diffusivity between high and low diffusivity paths can be quite large at low temperatures; $D_{gb} / D_m = 10^8$.[24] This value can be larger in hexagonal material if the interface is located perpendicular to the c-axis.[25] When the denuded zone reaches a width which is large compared to the bulk diffusion distance, Mg_2Si precipitates may form at the ends of the eutectic rods. The Si atoms diffuse along the rod surface and collect at the termination points. This behavior can be seen in Figure 36b. Note the large precipitates of cubic morphology located along the perimeter between the eutectic rods and the denuded zone. These precipitates were identified as Mg_2Si using CBED.

The 8.0 wt.% Si alloy consisted of primary Mg_2Si dendrites in a Mg matrix. After a two hour anneal at 300°C, the dendritic Mg_2Si centers were rounded and the eutectic rods along the perimeter of the dendrites had broken-up into smaller individual particles. Further aging at this temperature continued to spheroidize the intermetallic compound contained in the matrix.

Microhardness of Melt-spun Alloys

Knoop microhardness measurements were obtained from both as-spun and aged specimens. The microhardness of the as-spun alloys increased with Si content to 5 wt.% and then decreased at higher compositions (Figure 38). The peak in the microhardness corresponds to the 5 wt.% Si alloy with the coupled eutectic microstructure. The results of microhardness tests on ribbon aged at 300°C are shown in Figure 39. Small initial increases in hardness were observed in the 1.0 and 3.0 wt.% Si alloys, whereas the 5.0 wt.% Si alloy had a large drop in hardness, and the 8.0 wt.% Si alloy remained relatively stable. The increase in hardness of the dilute alloys may result from the break-up of the Mg_2Si eutectic rods into smaller individual particles. This process would be less effective as a strengthening mechanism as the Si content increased, and would not be a factor in the other alloys due to their dissimilar microstructure. The presence and growth of the denuded region alongside the cell boundaries can account for the drop in hardness of the coupled eutectic structure. Deformation is localized in these zones, which lowers the overall strength of the material. The primary intermetallic precipitates in the 8.0 wt.% Si alloy are not appreciably coarsened by heat treatment. Only the fine eutectic located along the border of the primary dendrites coarsens. This would result in only the modest drop in the microhardness observed in the 8.0 wt.% Si melt-spun ribbon.

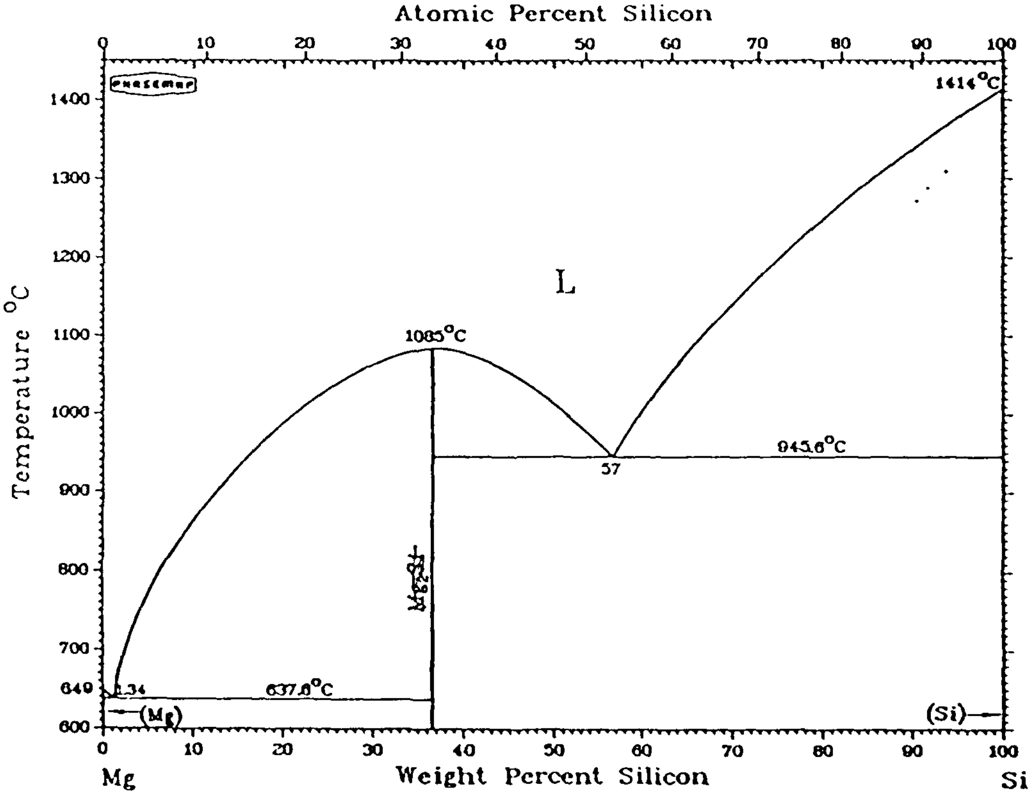

Figure 22. The Mg-Si phase diagram.

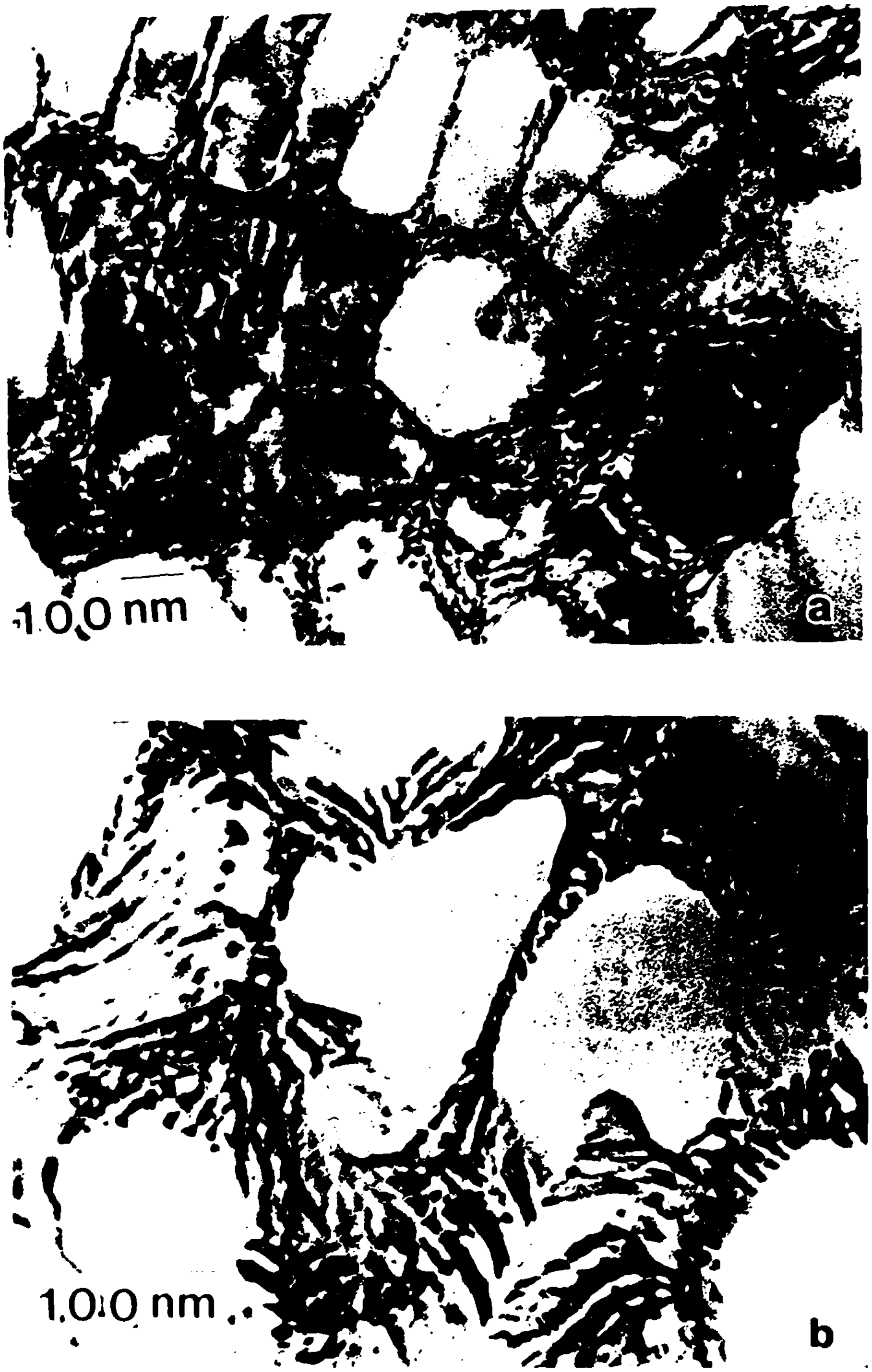
100 nm
a
100 nm
b

Figure 23. Microstructure of melt spun Mg-3.0wt.% Si. a) Cellular(dendritic) microstructure
b) Mg_2Si rods located at the cell boundaries

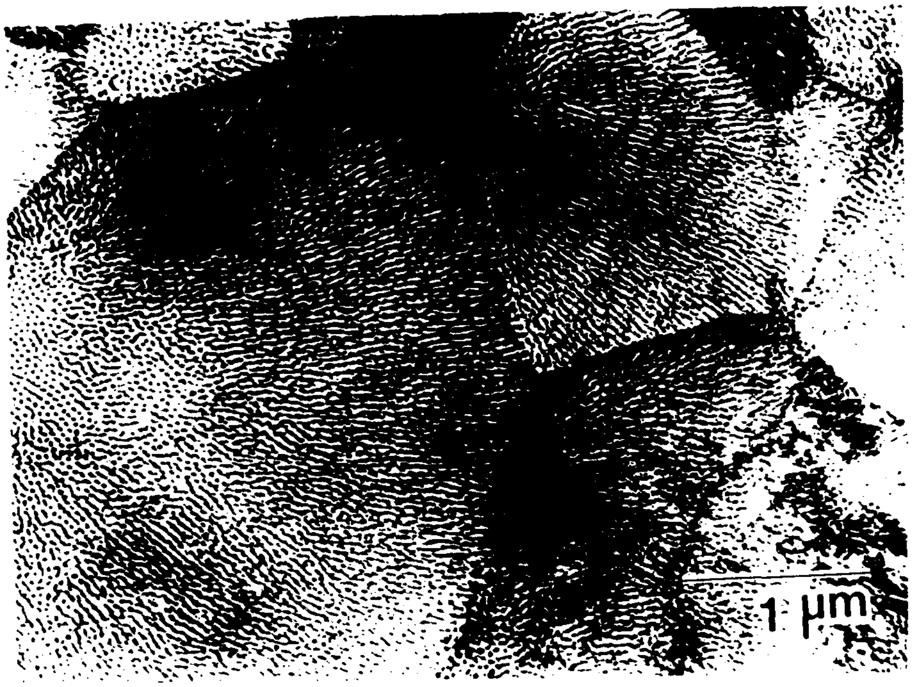

Figure 24. Microstructure present in melt-spun Mg-5.0wt% Si ribbon.

Figure 25. Fine eutectic microstructure present in melt-spun Mg-5.0wt.% Si. Note the individual eutectic rods are noticeably elongated.

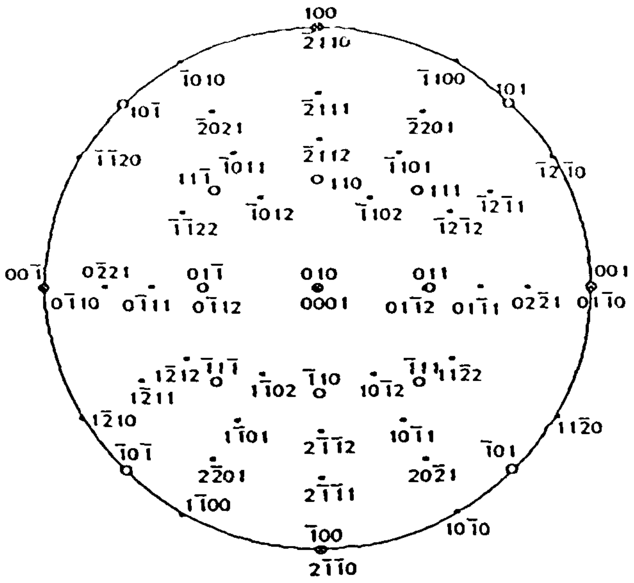
100
2̄110
1̄010
1̄100
101
101̄
2̄021
2̄111
2̄201
1̄120
1̄011
2̄112
1̄101
1̄21̄0
111̄
110
0111
1̄21̄1
1̄012
1̄102
1̄122
1̄21̄2
001̄
02̄21
011̄
010
011
001
01̄10
01̄11
01̄12
0001
011̄2
011̄1
022̄1
011̄0
12̄12
1̄11̄
12̄11
11̄02
1̄10
101̄2
1̄11
1̄1̄22
12̄10
11̄20
1̄01̄
11̄01
21̄1̄2
101̄1
1̄01
22̄01
202̄1
21̄1̄1
11̄00
1̄00
101̄0
21̄1̄0

[0001] stereographic projection

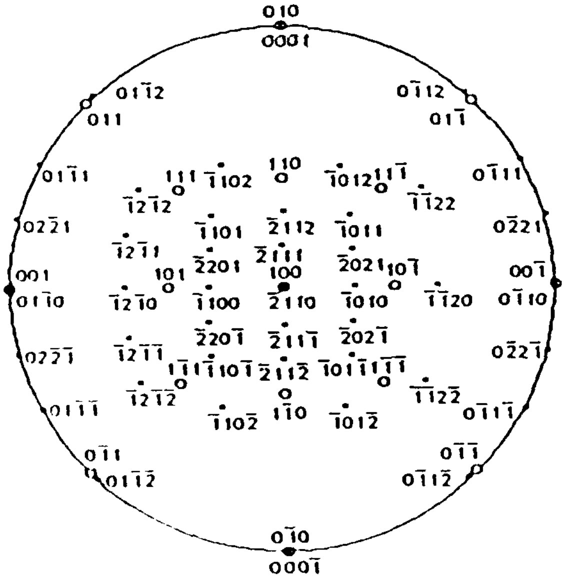
010
0001
01̄12
011
01̄1̄2
011̄
01̄11
111
1̄102
110
1̄012
11̄1̄
1̄21̄2
1̄1̄22
1̄101
2̄112
1̄011
01̄1̄1
02̄21
02̄2̄1
1̄21̄1
101
2̄201
2̄111
100
2̄021
101̄
001
001̄
01̄10
1̄21̄0
1̄100
2̄110
1̄010
1̄1̄20
01̄1̄0
2̄201̄
2̄111̄
2̄021̄
02̄2̄1
02̄21̄
1̄21̄1̄
1̄11̄
1̄101̄
2̄112̄
1̄011̄
1̄1̄1̄
1̄21̄2̄
1̄1̄22̄
01̄11̄
01̄1̄1̄
1̄102̄
1̄10
1̄012̄
011̄
01̄1̄
01̄12̄
01̄1̄2̄
01̄0
0001̄

[2110] stereographic projection

Figure 26. Stereographic projections which correspond to the orientation relationship observed between Mg and Mg_2Si in the coupled eutectic.

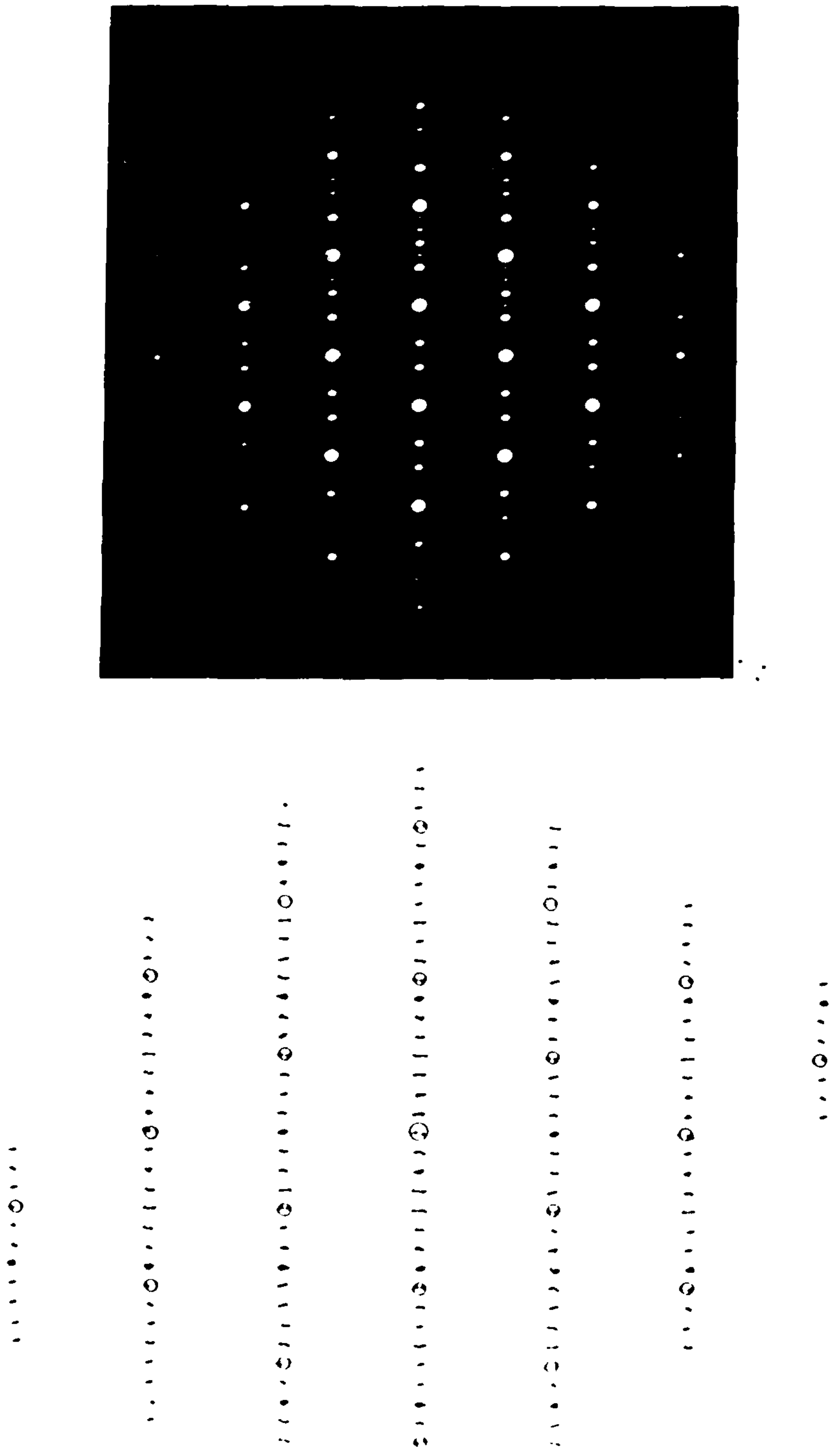

Figure 27. Actual SADP obtained from the coupled eutectic with the beam aligned close to [0001]Mg. Included is a computer simulation of the diffraction pattern.

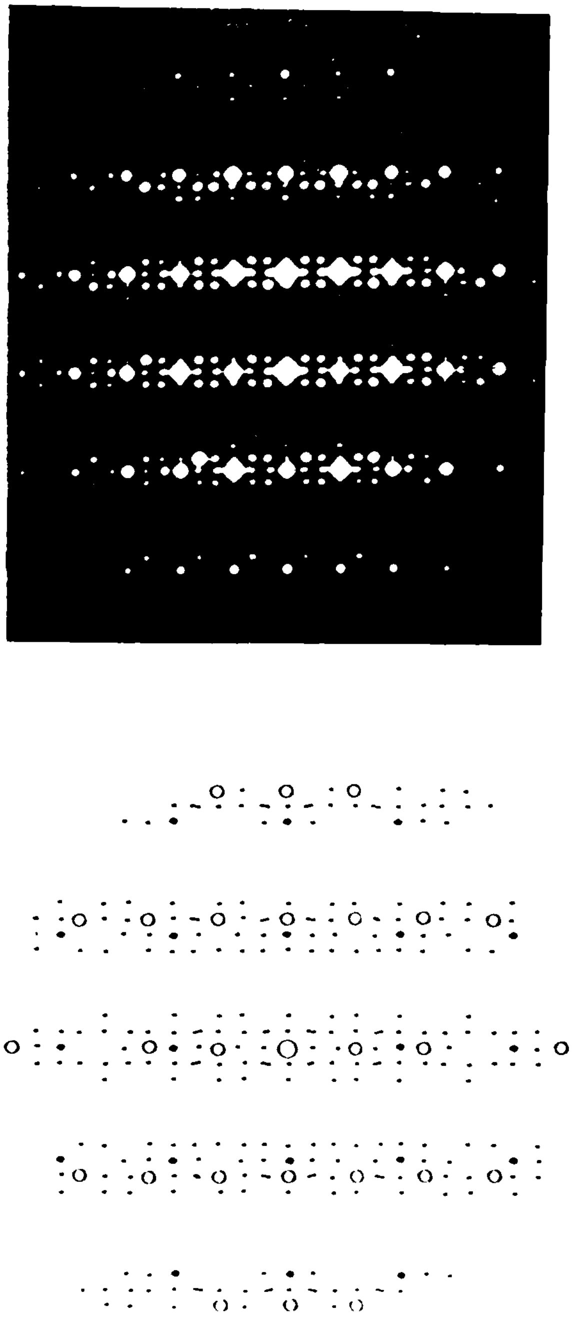

Figure 28. Actual SADP obtained from the coupled eutectic with the beam aligned close to $[\bar{2}110]$Mg. A computer simulated diffraction pattern is included for comparison.

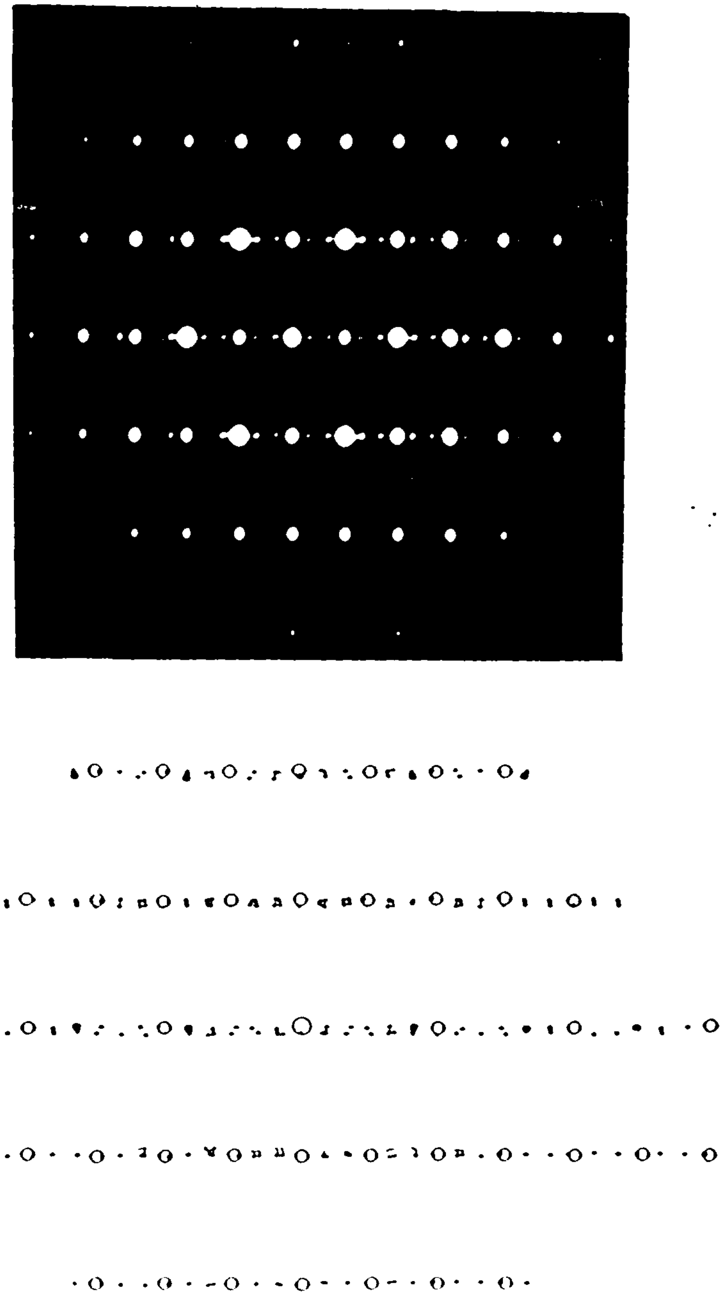

Figure 29. Actual SADP obtained from the coupled eutectic with the beam aligned close to [1210]Mg. A computer simulated diffraction pattern is included for comparison.

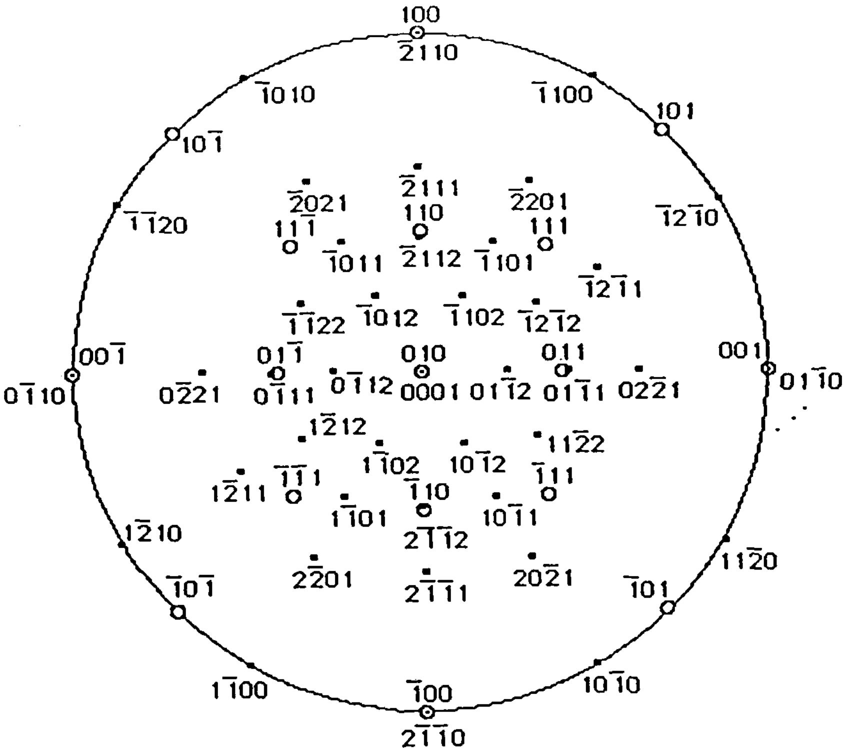
100
2̅110
1̅010
1̅100
101
101̅
2̅111
2̅021
2̅201
1̅1̅20
1̅21̅0
110
111̅
111
1̅011
2̅112
1̅101
1̅21̅1
1̅1̅22
1̅012
1̅102
1̅21̅2
001̅
011̅
010
011
001
01̅10
02̅21
01̅11
01̅12
0001
011̅2
011̅1
022̅1
011̅0
12̅12
11̅02
101̅2
112̅2
1̅1̅1
12̅11
1̅11
1̅10
11̅01
101̅1
21̅1̅2
12̅10
112̅0
1̅01̅
1̅01
22̅01
21̅1̅1
202̅1
11̅00
1̅00
101̅0
21̅1̅0

Directions are shown.

Figure 30. Stereographic projection showing the relationship between the matrix and the long axis of the Mg.

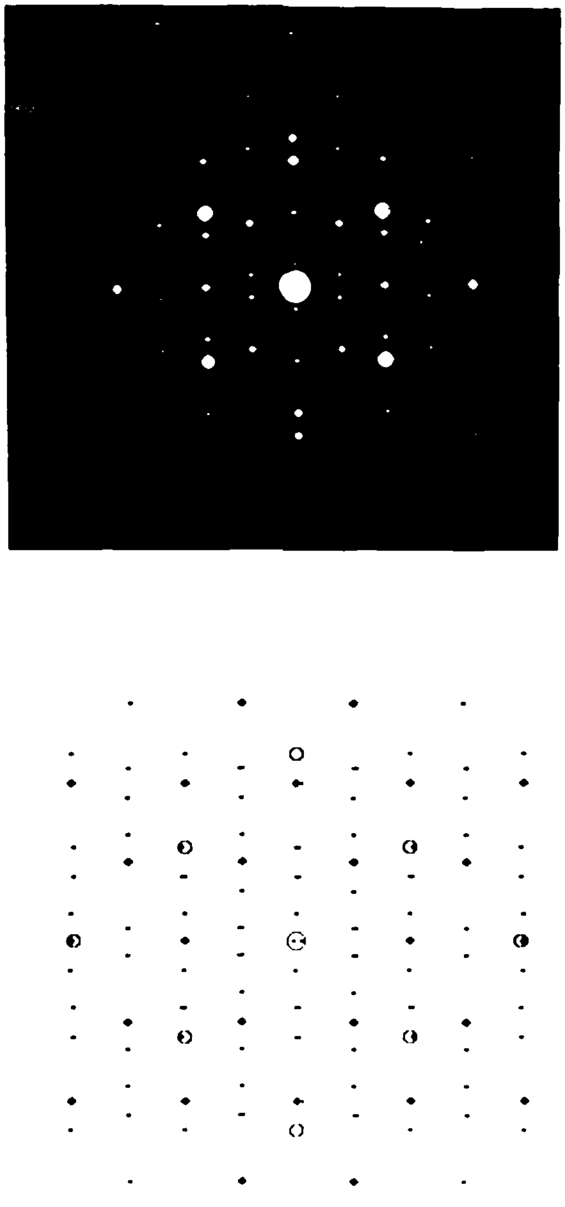

Figure 31. SADP taken with the beam parrallel to the long axis of the eutectic rods. The matrix direction is close to [01$\bar{1}$1] A computer simulated diffraction pattern is included for comparison

Lattice Plane		Spacing	Misfit
d_1	$(400)_{Mg_2Si}$	1.580Å	$\frac{\lvert d_1 - d_2 \rvert}{d_2} = 0.0137$
d_2	$(2\bar{1}\bar{1}0)_{Mg}$	1.605Å	
d_3	$(420)_{Mg_2Si}$	1.417Å	$\frac{\lvert d_3 - d_4 \rvert}{d_4} = 0.0194$
d_4	$(20\bar{2}0)_{Mg}$	1.390Å	

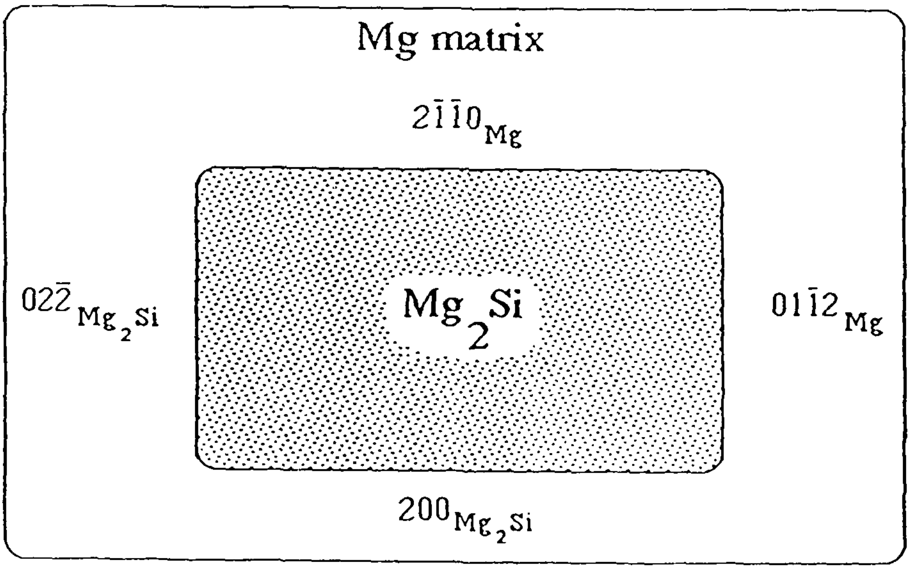
Mg matrix
$2\bar{1}\bar{1}0_{Mg}$
$02\bar{2}_{Mg_2Si}$
Mg_2Si
$01\bar{1}2_{Mg}$
200_{Mg_2Si}

Figure 32. Schematic diagram showing the mismatch and alignment observed between the crystal planes in Mg and Mg_2Si.

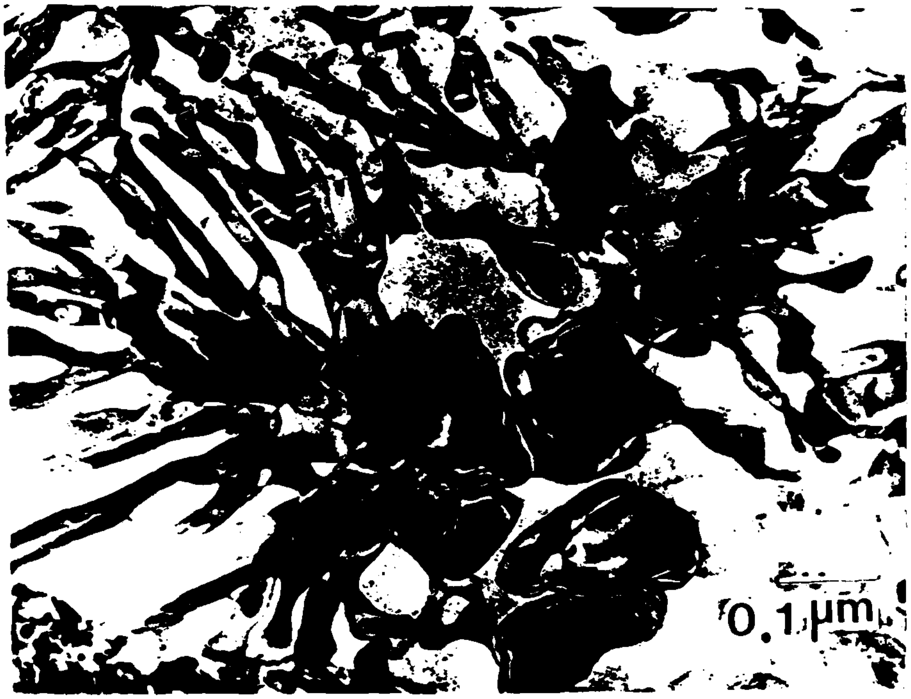

Figure 33. Microstructure present in melt-spun Mg-8.0wt.% Si ribbon.

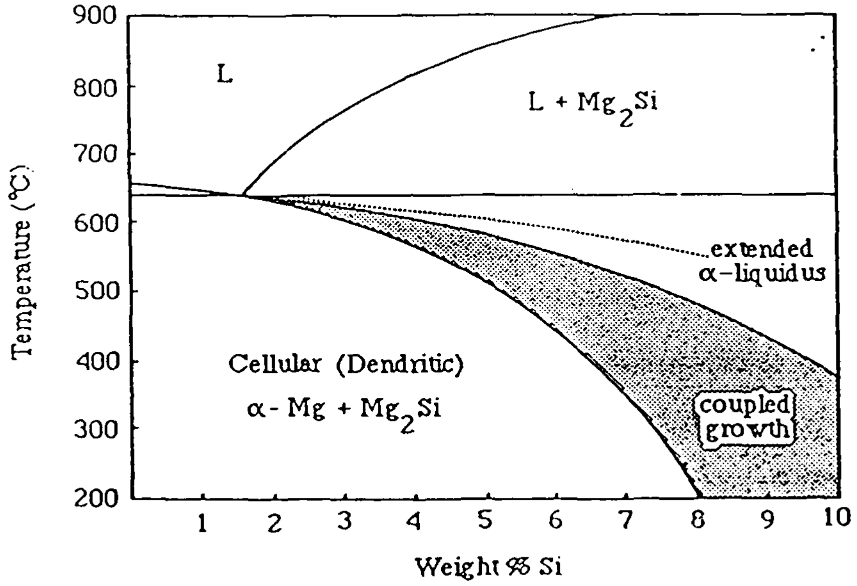

Figure 34. Mg-Si metastable phase diagram.

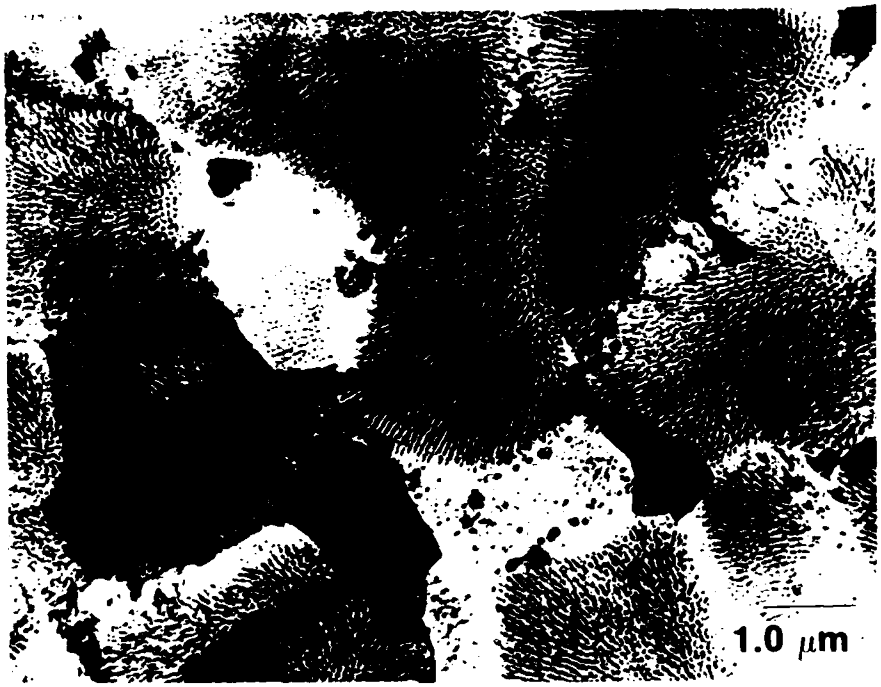

Figure 35. Mg-5.0wt.% Si melt-spun ribbon after aging for 2 hours at 300°C.

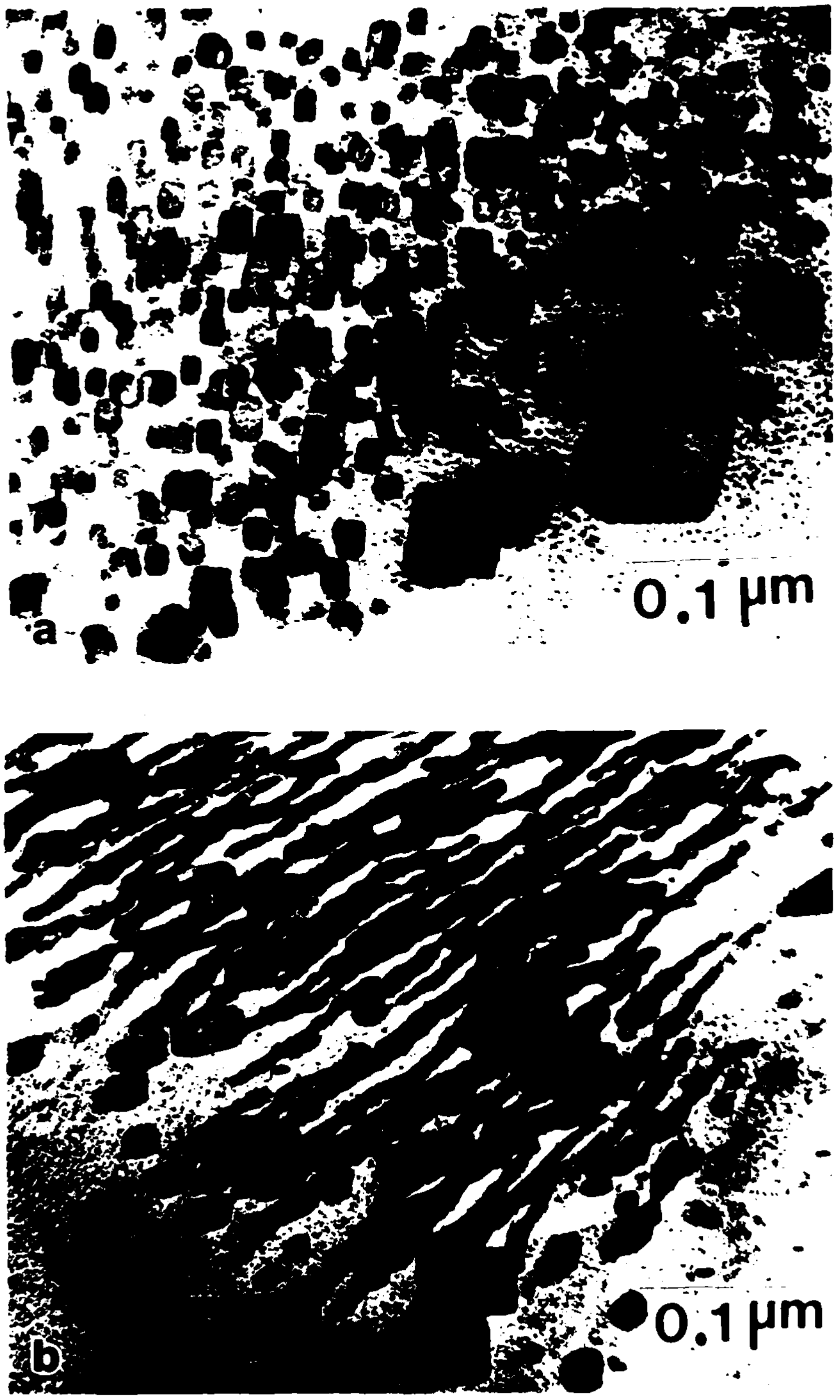

Figure 36. Eutectic rods in melt-spun Mg-5.0wt.% Si. Aged 72 hours at 300°C.a) view down rod axis b) view 48° away from rod axis.

Figure 37. Dual phase microstructure produced after aging the Mg-5.0wt.% Si melt-spun ribbon for 200 hours at 300°C.

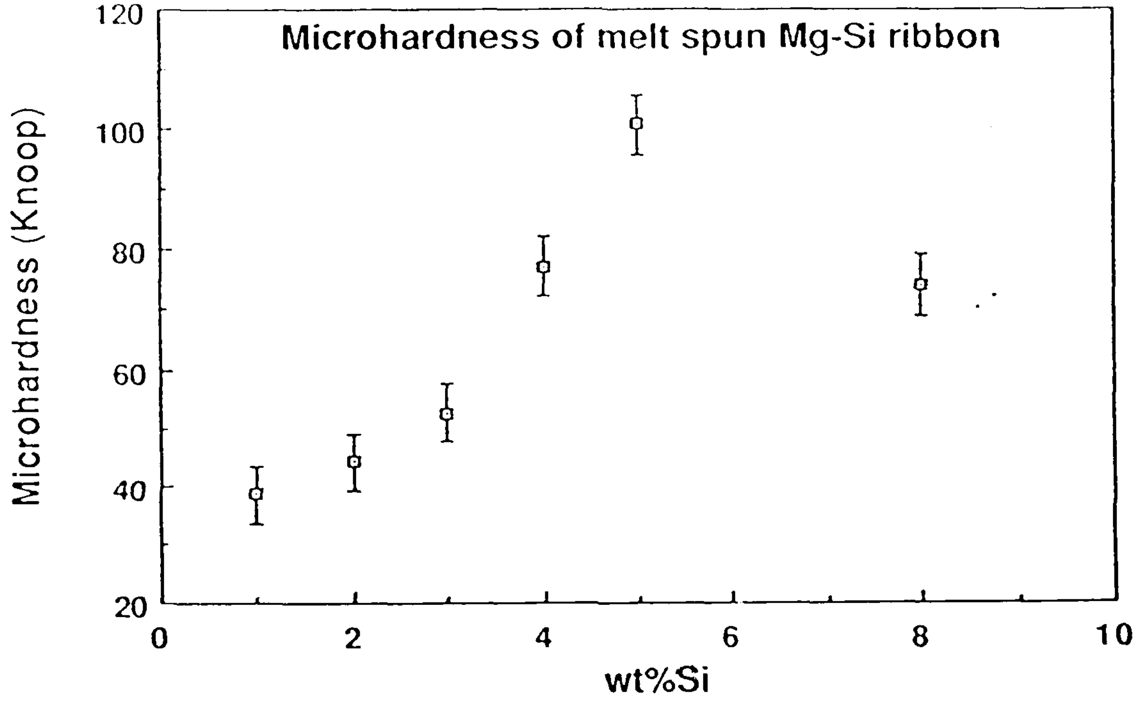

Figure 38. Microhardness (Knoop, 50gram load) of the melt-spun ribbon as a function of Si content.

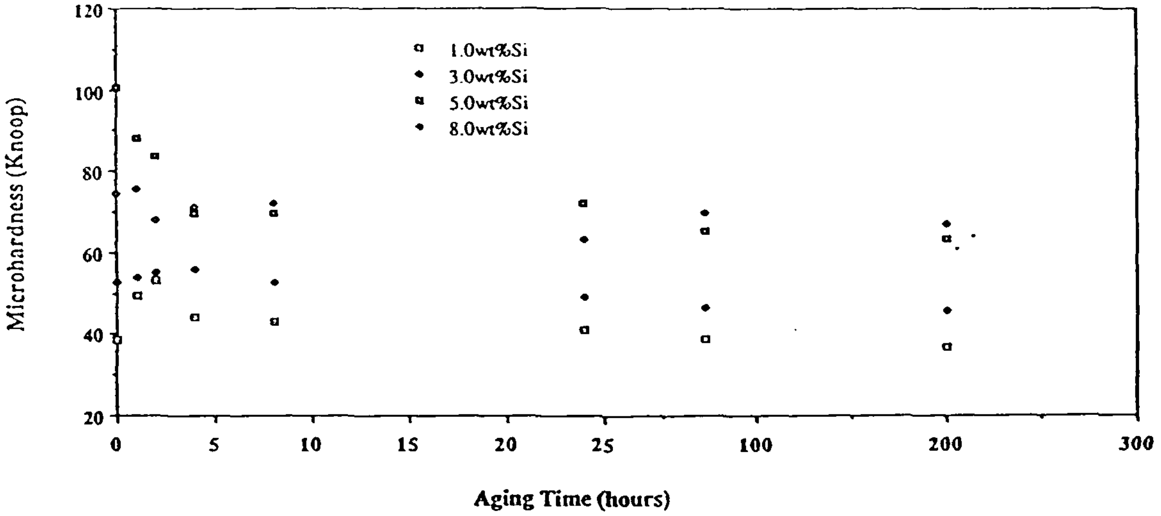

Figure 39. Microhardness (Knoop, 50 gram load) for the melt spun Mg-Si alloy ribbons after aging at different temperatures and for various times.

3.4 Mg-Li Alloys

Mg-Li alloys have excellent modulus and very low densities. In addition, the Li promotes non-basal slip in Mg which improves the ductility of the alloys. Larger additions of Li to Mg produce the ductile bcc phase. Unfortunately, Mg-Li alloy have very low creep strengths. The addition of a stable dispersoid is expected to improve this property. Si additions and RSP have been used in an attempt to form stable silicide dispersions in Mg-Si alloys. The microstructures of the as-cast Mg-Li alloys have been described in the report of the first year's work.

3.4.1 Melt-Spun Ribbons

A superheat of 250°C was used to eliminate the possibility of unmelted Mg_2Si particles affecting the solidification structure of the melt-spun ribbon. It was observed that the quality (i.e. uniformity of width and thickness) of the melt spun ribbon increased with increasing Si content. The surface condition of the ribbon also improved with increasing Si content. Melt spinning had effect of reducing the grain size in the binary 5.0 and 12.0 wt.% Li alloys. The as-spun microstructure of the Mg-8wt.%Li alloy was two phase after melt spinning. The microstructure consisted predominately of α-Mg, with small grains of β-Mg dispersed in the matrix. The microstructures of the melt spun binary alloys are shown in Figure 40 a,b&c.

Silicon additions to the binary Mg-Li alloys result in the formation of crystals of Mg_2Si, although they are much smaller than in the LSM alloy. The size and number of larger Mg_2Si precipitates increased with Li content. Figure 41 a,b&c shows the microstructures typical of the three melt spun alloys. In the Mg-5.0wt.% Li-5.0wt.% Si the majority of the silicide was in the form of irregular eutectic rods (Figure 42). The amount of eutectic decreased with increasing Li content of the alloy. The Mg-Li-Ge diagram developed by Kinzhibalo[26] shows that the eutectic composition between Mg_2Ge and Mg decreases with Li content. If the diagram is similar to the Mg-Li-Si phase diagram, and this is reasonable because of the similar chemical nature of Ge and Si, then the eutectic composition between Mg_2Si and Mg would also decrease with increasing Li content. This would cause the amount of eutectic observed in the alloy to also decrease, since the undercooling of the alloy melt would have to be very large to reach the region of coupled eutectic growth.

Upon aging the Mg-8wt.% Li-5wt.% Si alloy for 2 hours at 300°C the microstructure contained fine irregular randomly oriented precipitates (Figure 43). The facets of the Mg_2Si crystals were rounded after heat treatment. In all three alloys, after heat treating for 2 hours at

500°C, the large primary Mg_2Si crystals and eutectic structure had been transformed into a uniform matrix of α, β, or α/β, depending upon alloy composition, and large Mg_2Si precipitates (Figure 44).

Microhardness measurements were obtained from the cross section melt-spun ribbon. The results are listed in Table 6. The hardness of the melt spun ribbon was greater than that observed for the LSM alloys or the as-cast material. This is due to the much finer distribution of silicide in the ribbon. The ability to preheat the melt prior to melt spinning to eliminate unmelted material is a major benefit of melt spinning. The unmelted particles can act as nucleating agents during solidification. Without these nucleating agents, the alloy can be undercooled to a much lower temperature, which yields a higher interface growth velocity and finer distribution of silicide in the matrix.

3.4.2 Centrifugally Atomized Powder

Centrifugally atomized powder was produced to provide particulate for consolidation. Powder may be consolidated using dynamical compaction, which preserves the as-solidified microstructure. Melt-spun ribbon is difficult to compact in this manner, and therefore, mechanical data from the as-solidified material could not be obtained.

As-Atomized Microstructure

Two alloys were centrifugally atomized; Mg-8wt.%Li and Mg-8wt.%Li-1.5wt.%Si. This Si content was chosen for several reasons. This amount of Si will produce a fine dispersion of silicide, yet it should not be large enough to allow the formation of primary Mg_2Si dendrites which would lower the ductility of the alloy. A SEM micrograph of the alloy powders is shown in Figure 45. Note the spherical nature of the powders and the presence of only a few satellites on the powder surface. Optical micrographs of individual powders are shown in Figure 46 a&b. The microstructures of the individual powders are apparently very fine. The α and β phases, and in the Si containing alloy the Mg_2Si phase, were all detected in x-ray powder patterns. TEM examination of individual powders revealed the presence of a cellular microstructure with very fine Mg_2Si particles located intercellularly (Figure 47a). The microstructure of the binary alloy was dual phase α-Mg and β-Li (Figure 47b).

Dynamically Compacted Material

The CA powder was dynamically compacted and the microstructure and mechanical properties of the compacts examined. It hs been shown that dynamical compaction (DC) does not affect the as-rapidly solidified microstructure in the center of the powder.[27] The powder interface is highly deformed during the compaction process, and in some cases melted and resolidified, but the interior of the powder is only deformed and does not experience a significant thermal excursion. This means that metastable microstructures may be retained in the powder using dynamic compaction. Optical micrographs of the compacted material taken perpendicular to the compaction plane are shown in Figure 48 a&b. Note that the rapidly solidified microstructure is retained after processing. There are several regions in the compacts were interfacial melting is evident. In the micrographs these regions are the irregular light color areas located at the powder-powder boundaries. The microstructure of the binary alloy contained both α and β grains randomly distributed throughout the matrix (Figure 49a). No rational orientation relationship between the α and β phases in the powder has been observed. The Mg-8wt.% Li-1.5wt.% Si alloy had small Mg_2Si rods at the boundaries of α cells (Figure 49b). Small β grains were also located intergranularly, and a few were located within the cells.

The compacts were subsequently heat treated for 2 hours at 300°C. After the heat treatment, the α and β phases had coarsened significantly in the binary alloy (Figure 50a), while no observable change had occurred in the Si containing alloy (Figure 50b). The microstructure in the remelted regions in the binary alloy was much more refined after heat treatment than in the bulk of the material. The reason for this behavior is not known, but it is possible that oxide from the surface of the powder was mixed into the melted region during compaction and this oxide suppresses the growth of the α and β grains much like the silicide dispersion in the Si containing alloys. Microhardness values obtained from the as-compacted and heat treated material show that the alloy containing silicon retains a greater percentage of as-compacted hardness after heat treatment than the binary alloy. Hardness values for the binary alloy Mg-8wt.% Li are 61.7 as-compacted and 47.8 after the heat treatment. Hardness values for the Mg-8wt.% Li-1.5wt.% Si alloy are 65.4 as-compacted and 57.5 after heat treatment. From these data and the micrographs it appears that the silicide dispersion acts as an effective barrier to the growth of the α and β phases.

Tensile specimens were machined from the compacts. The specimens were machined with their tensile axis perpendicular to the compaction direction. Several of the specimens were heat treated for 2 hours at 300°C prior to testing. Results of the tests are presented in Table 7.

The ductility of all of the specimens was low, which is the result of weak interparticle bonding in the compact.

Hot Isostatically Pressed (HIP) Material

The alloy powder was HIP'd at 350°C and 186MPa for 8 hours. These HIP conditions were determined for pure Mg powder, and were also successfully used to HIP the alloy powder. Optical micrographs of the HIP'd material are shown in Figure 51 a&b. Porosity was not observed in sections from either composition. The α and β grains in the binary alloy had coarsened considerably. Individual grains were not apparent in the Si containing alloy. It appears that the silicide dispersion is effective in stabilizing the fine grain size in these alloys. Further examination of the consolidated material revealed that the Mg_2Si particles in the as-atomized powder had substantially coarsened during the HIP process (Figure 52). There was no difference in the Mg_2Si particle size between those located in α or β grains. The largest particles were located on grain boundaries, presumably due to the enhanced grain boundary diffusion of Si in the alloy. Mg precipitates in β were observed in both alloys (Figure 53). Since they were not observed in the as-atomized or dynamically compacted specimens, it is presumed that they must have been produced during the HIP process. Microhardness values were obtained from both HIP'd compacts. The binary Mg-8wt.% Li alloy had an as-HIP'd Knoop microhardness of 44.1, and the alloy with 1.5wt.% Si added had a microhardness of 63.3. When these values are compared to those for the DC material, it ius apparent that the microhardness of the HIP'd binary alloy was lowest. There is a good correlation between hardness and grain size of the material; for example, the grain size was largest in the HIP'd material. The Si containing alloy did not experience a loss in microhardness due to hipping, presumably due to the stabilizing effect of the silicide dispersion.

Compression test specimens were machined from the compacts and the results of testing these samples are presented in Table 8. The compression data show the effectiveness of the silicide dispersion on both the room temperature and elevated temperature strength of the alloy. The addition of 1.5wt.% Si to the binary alloy increased the ultimate compressive strength of the alloy by ≈ 50%. The Si containing alloy also retained a greater percentage of its strength at temperature than did the binary alloy. The alloys tested at temperature had a much larger apparent ductility than did those tested at room temperature. Unfortunately, due to the nature of the test the strain to failure was not determined.

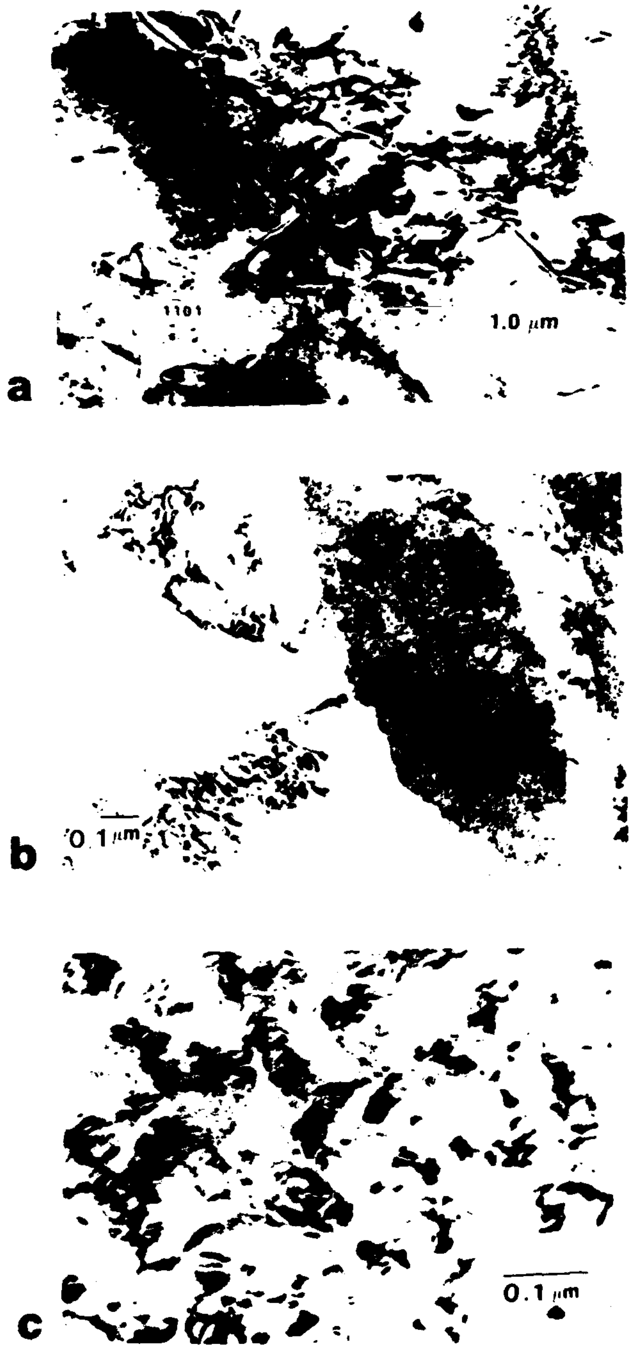
1.0 μm
a
0.1 μm
b
0.1 μm
c

Figure 40. Microstructure of the melt-spun binary Mg-Li alloys.a) Mg-5wt.% Li; b) Mg-8wt.% Li; c) Mg-12wt.% Li.

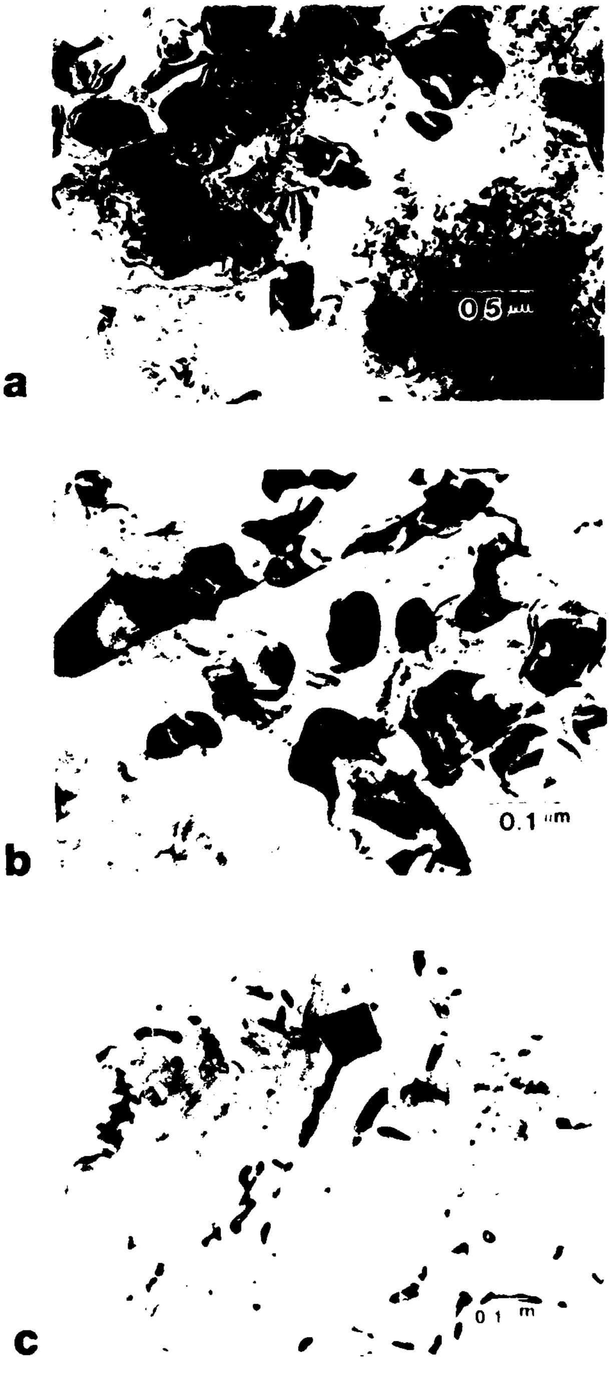
0.5 μm
a
0.1 μm
b
0.1 m
c

Figure 41. Microstructure present in melt-spun Mg-Li-Si alloys.a) Mg-5wt.% Li-5wt.% Si; b) Mg-8wt.% Li-5wt.% Si; c) Mg-12wt.% Li-5wt.% Si.

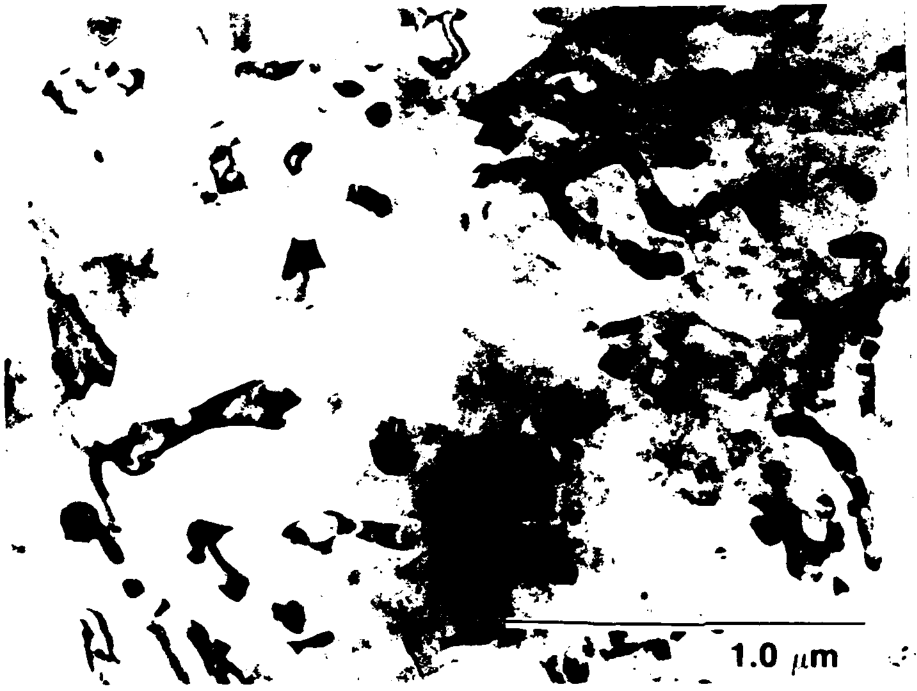

Figure 42. Irregular Mg_2Si rods present in the microstructure of Mg-5wt.% Li-5wt.% Si.

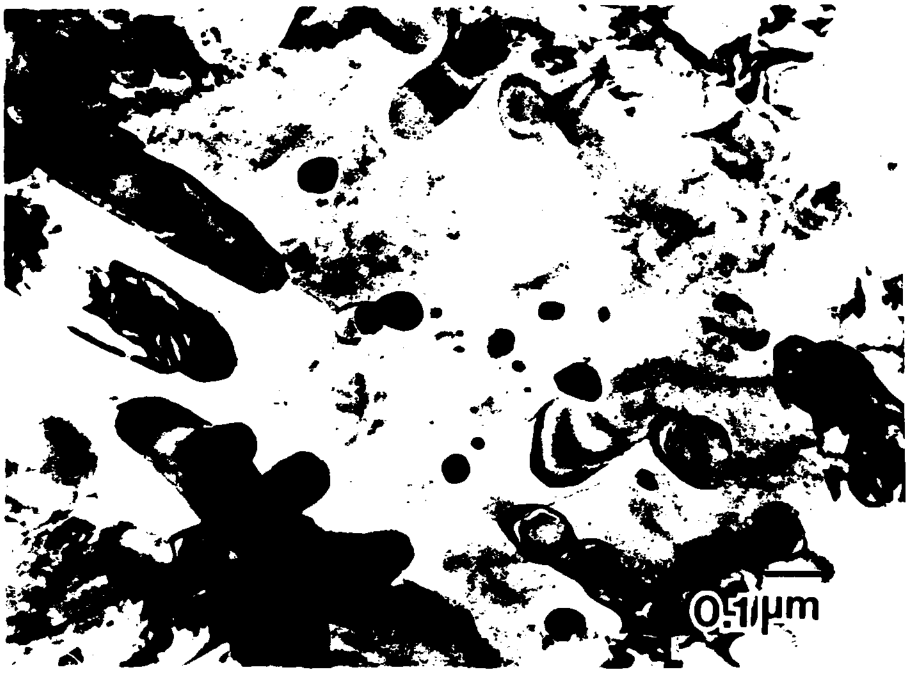

Figure 43. Microstructure of melt-spun Mg-8wt.% Li-5wt.% Si after aging for 2 hours at 300°C.

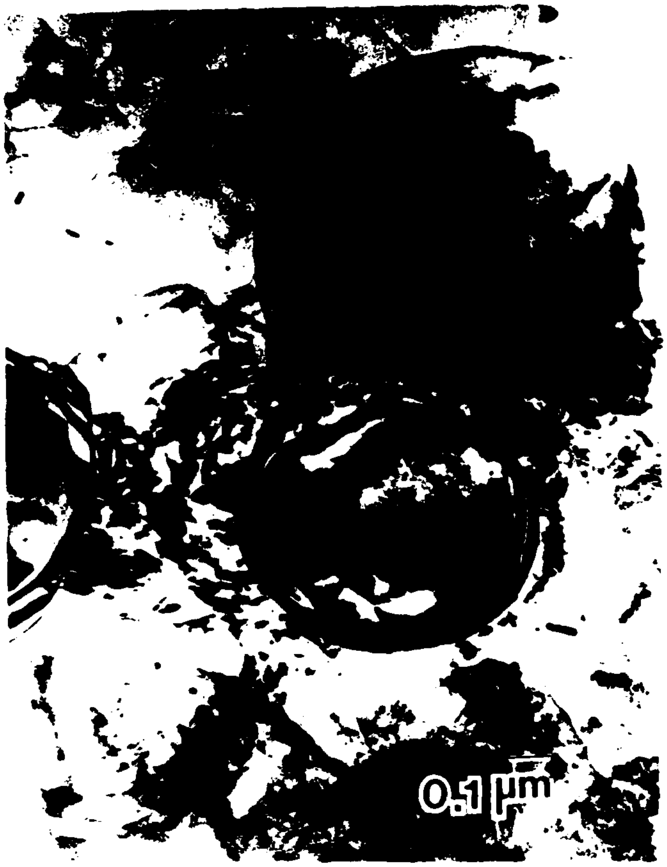

Figure 44. Microstructure of melt-spun Mg-5wt.%Li-5wt.%Si aged 2 hours at 500°C.

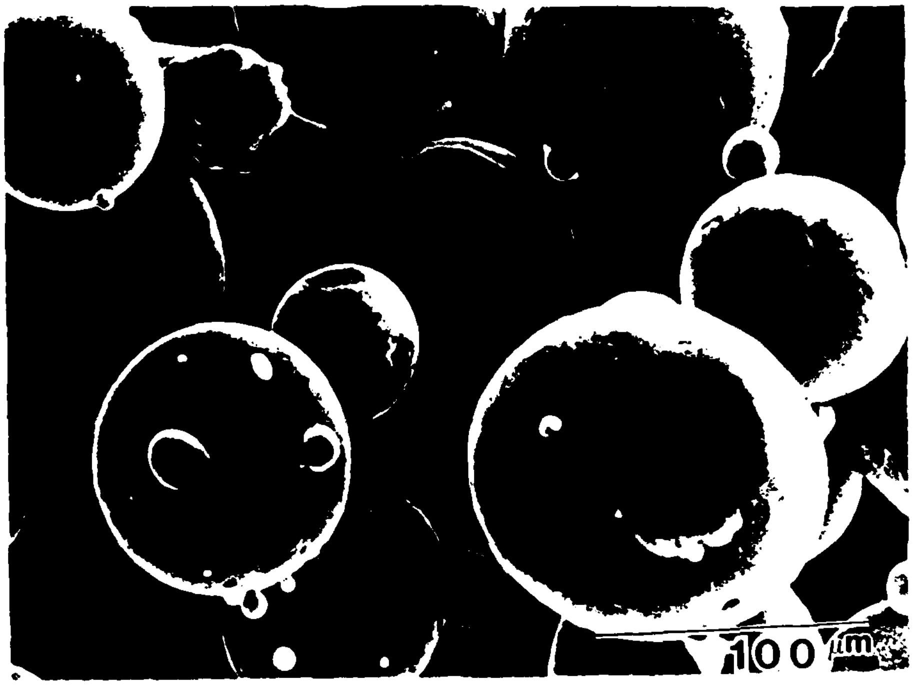

Figure 45. SEM micrograph of Mg-8wt.% Li alloy powders produced by centrifugal atomization.

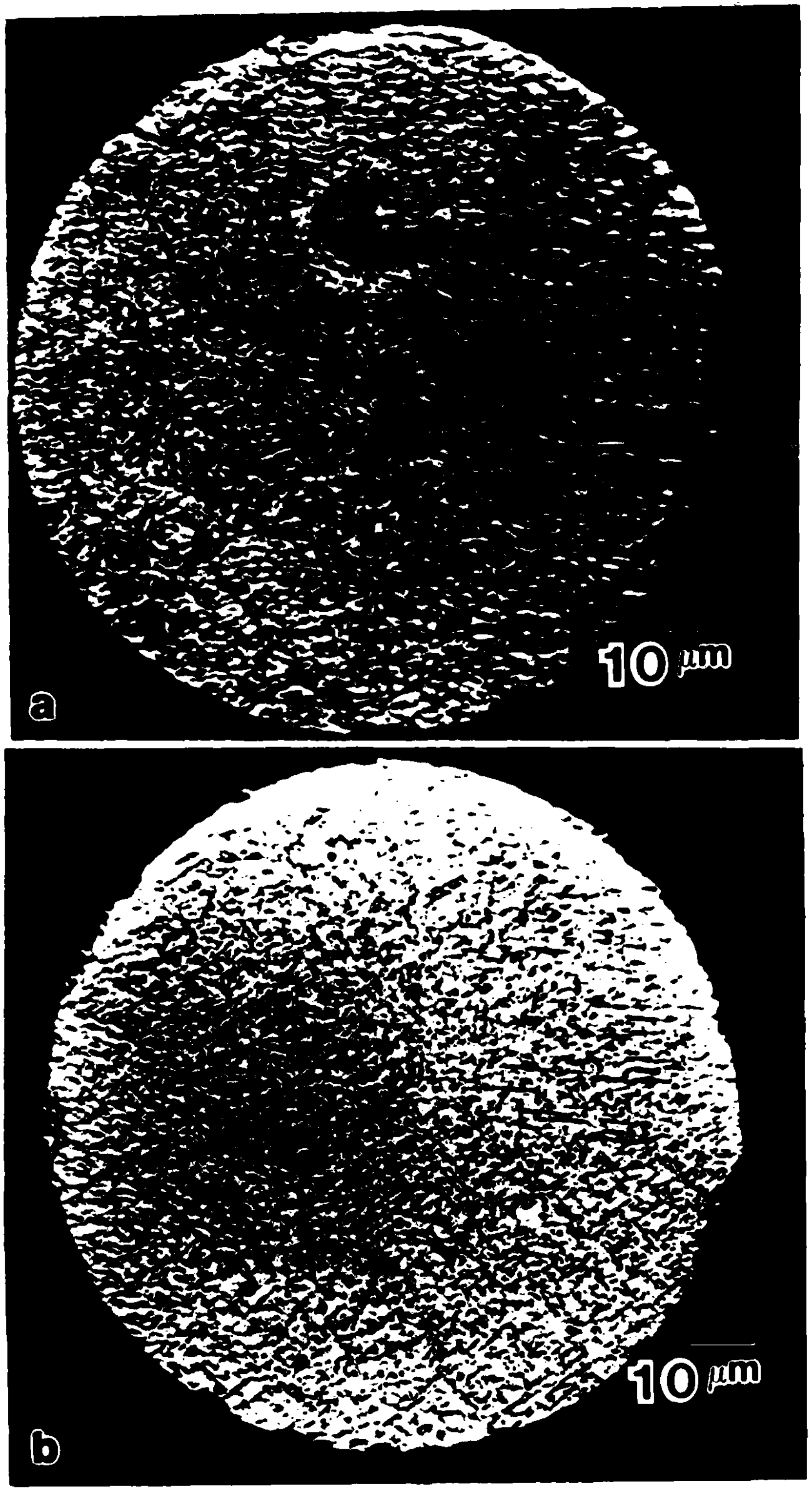
10 µm
a
10 µm
b

Figure 46. Optical micrographs of the as-CTA alloy powders. a) Mg-8wt.% Li;
b) Mg-8wt.% Li-1.5wt.% Si

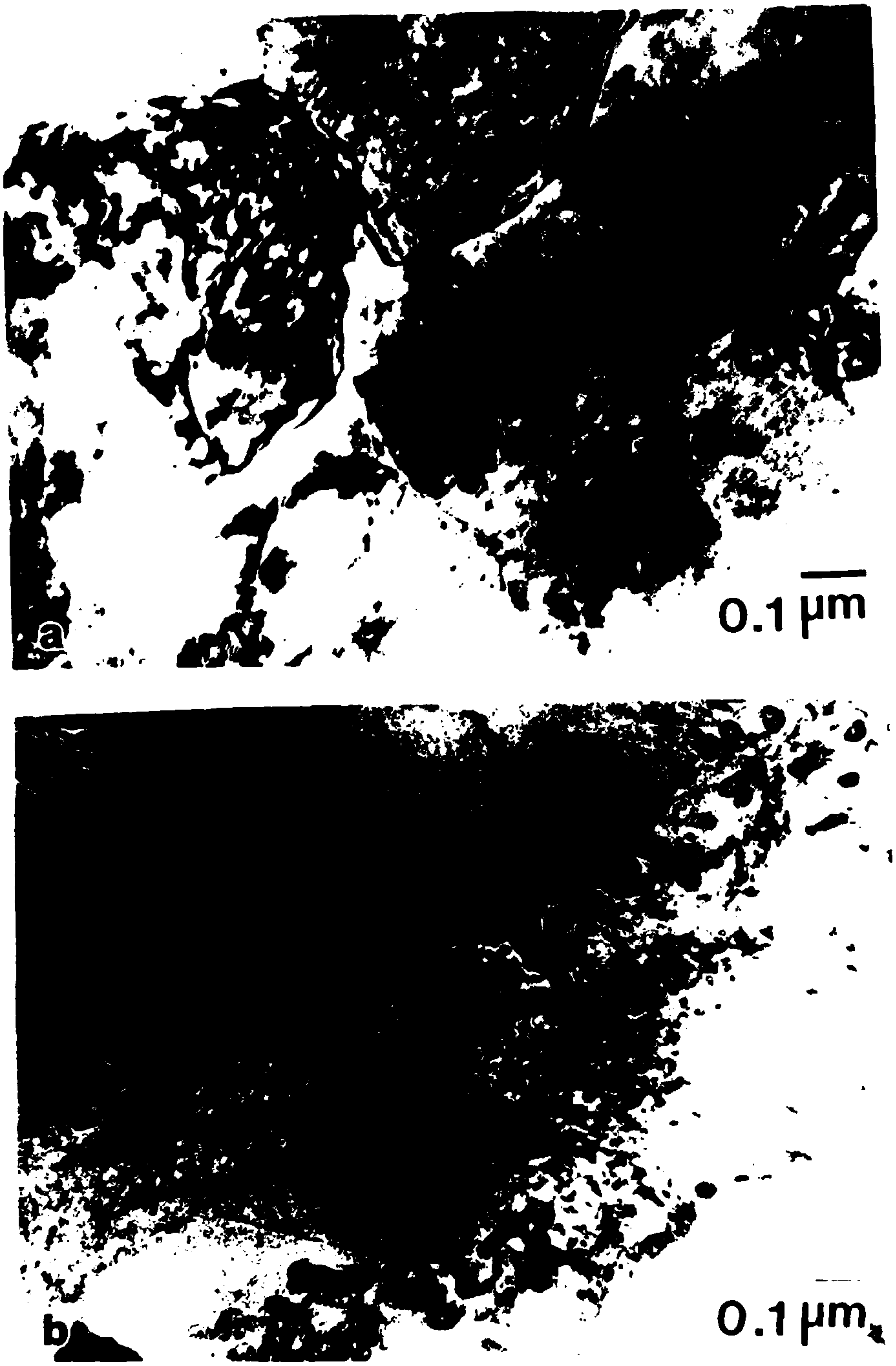
0.1 µm
a
0.1 µm
b

Figure 47. TEM micrographs of the as-CTA alloy powders. a) Mg-8wt.% Li; b) Mg-8wt.% Li-1.5wt.% Si.

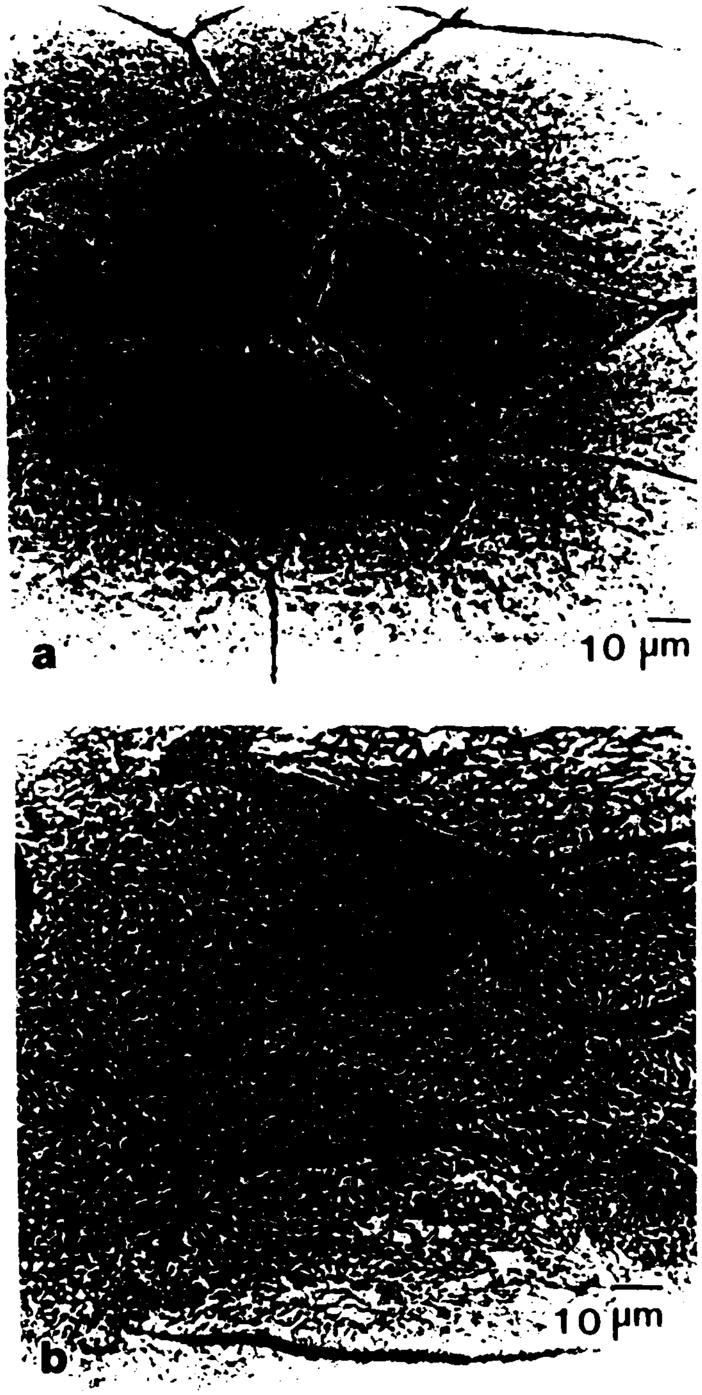

Figure 48. Optical micrographs of the compacts taken perpendicular to the compaction plane.
a) Mg-8wt.% Li; b) Mg-8wt.% Li-1.5wt.% Si

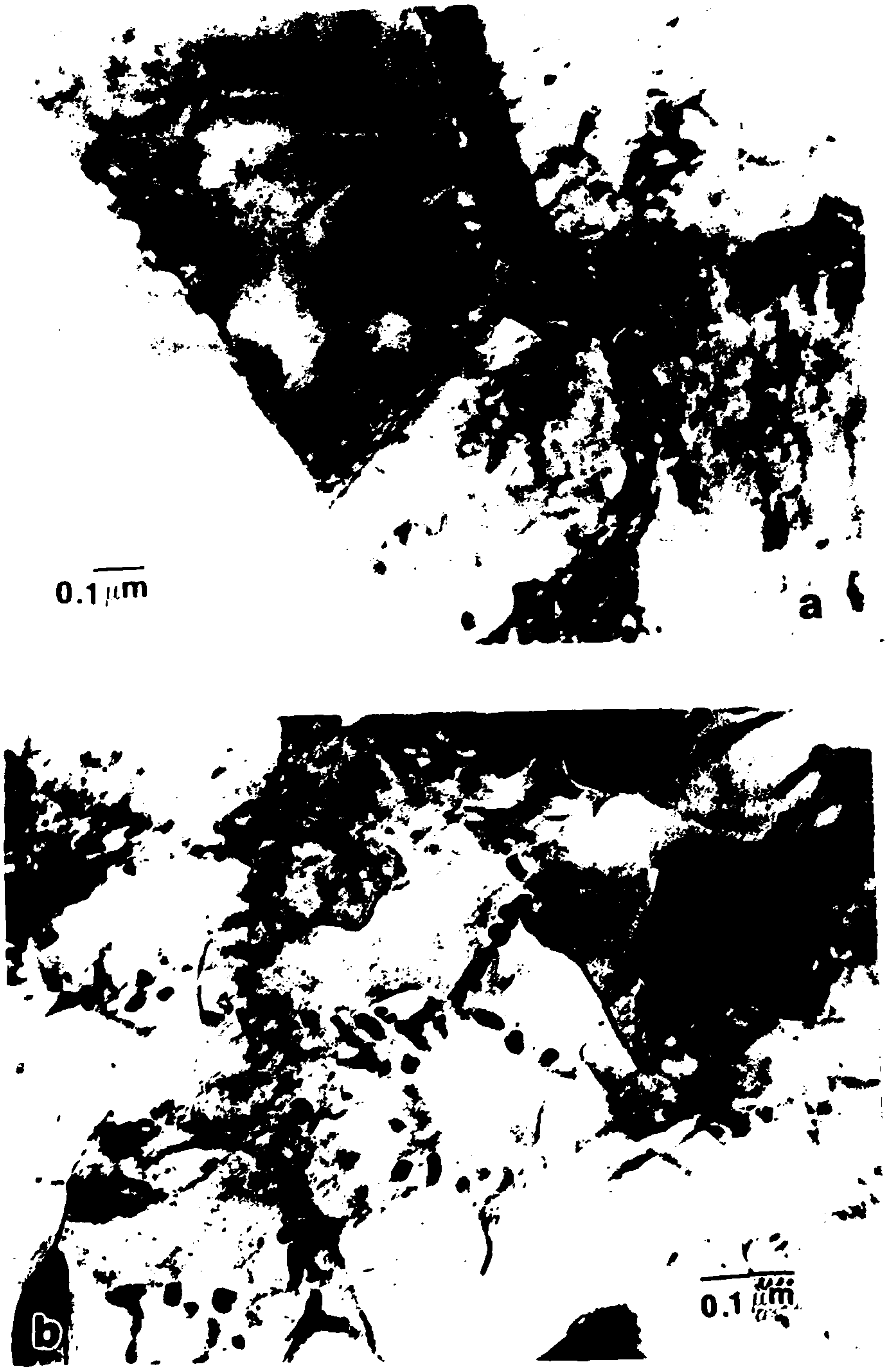
0.1 μm
a
b
0.1 μm

Figure 49. Microstructure present in the as-compacted material. a) Mg-8wt.% Li; b) Mg-8wt.% Li-1.5wt.% Si.

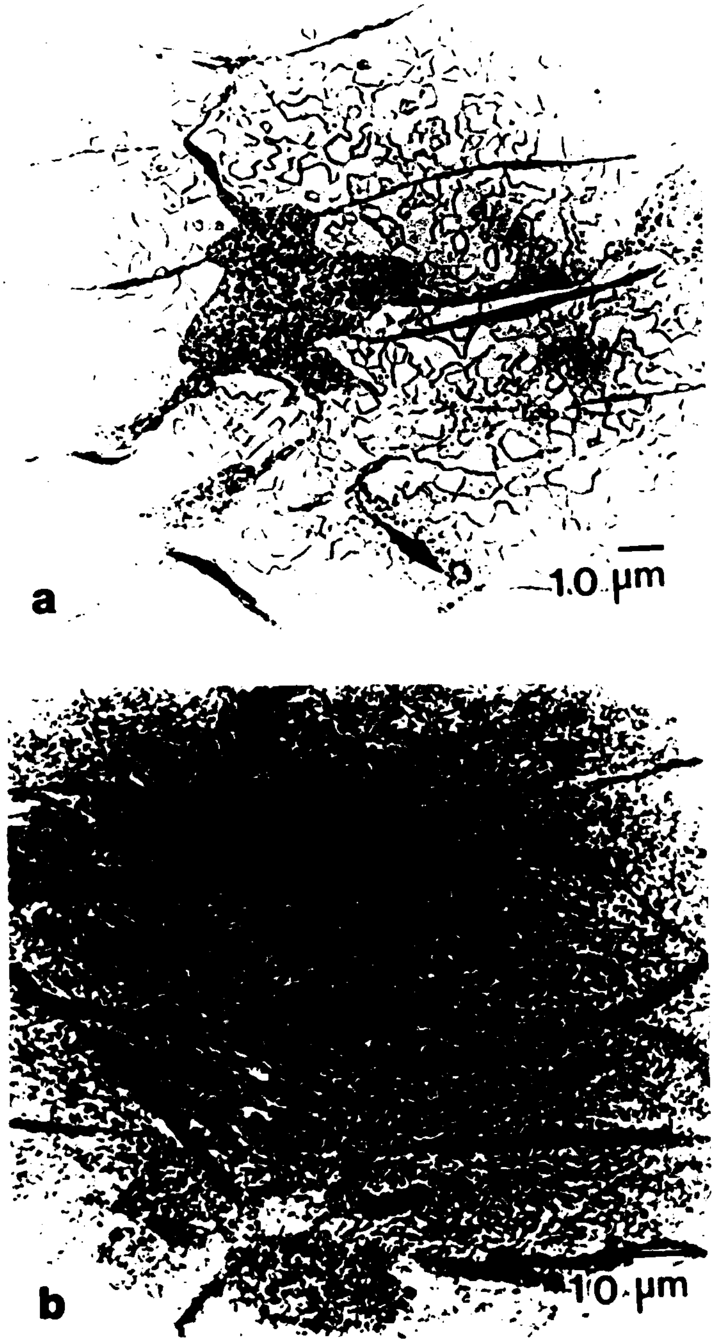

Figure 50. Microstructure present in specimens compacted and heat treated for 2 hours at 300°C. a) Mg-8wt.% Li; b) Mg-8wt.% Li-1.5wt.% Si

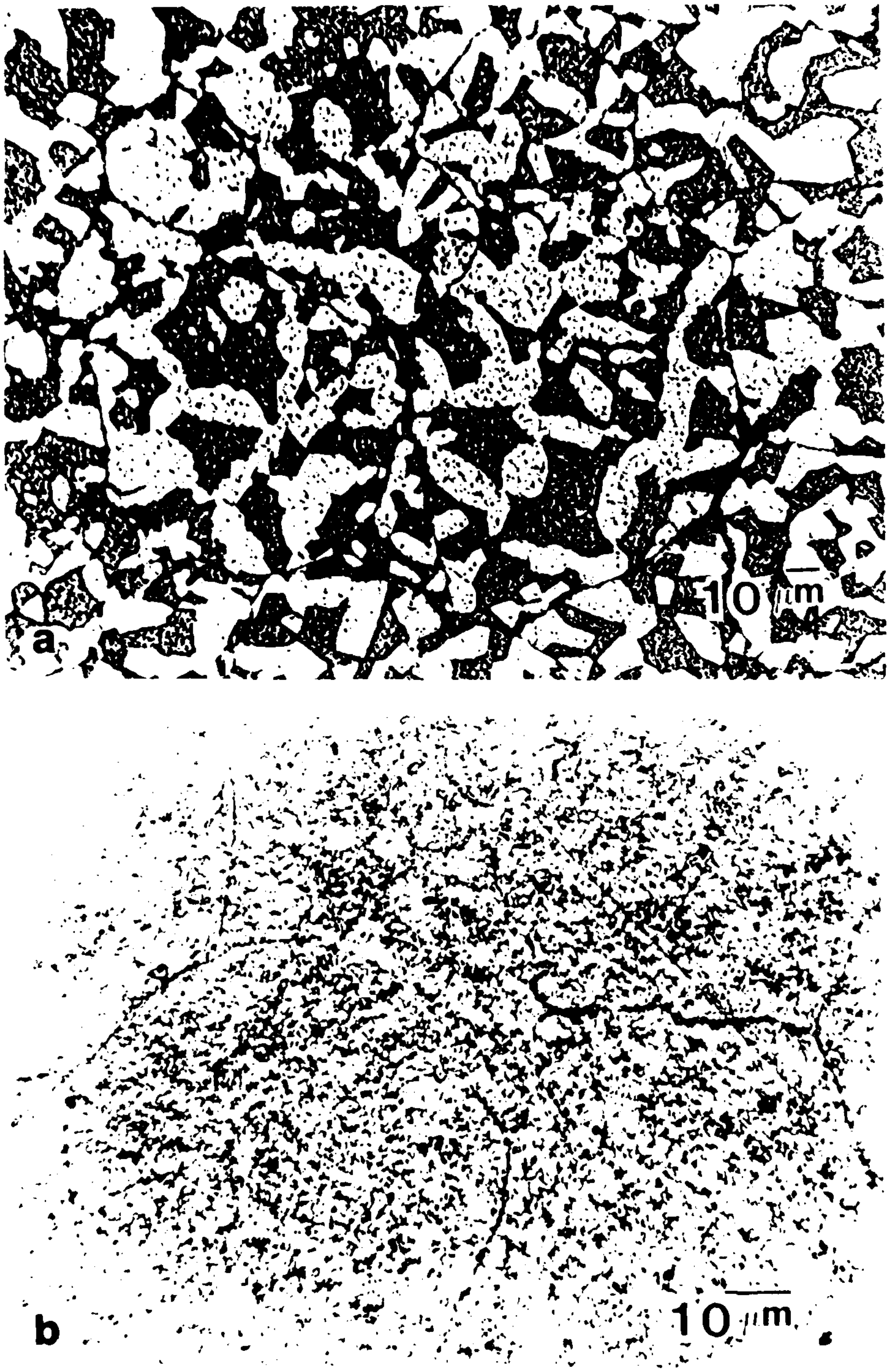
a
10 μm
b
10 μm

Figure 51. Microstructure of HIP'ed Mg-Li and Mg-Li-Si alloy powders. a) Mg-8wt.% Li; b) Mg-8wt.% Li-1.5wt.% Si

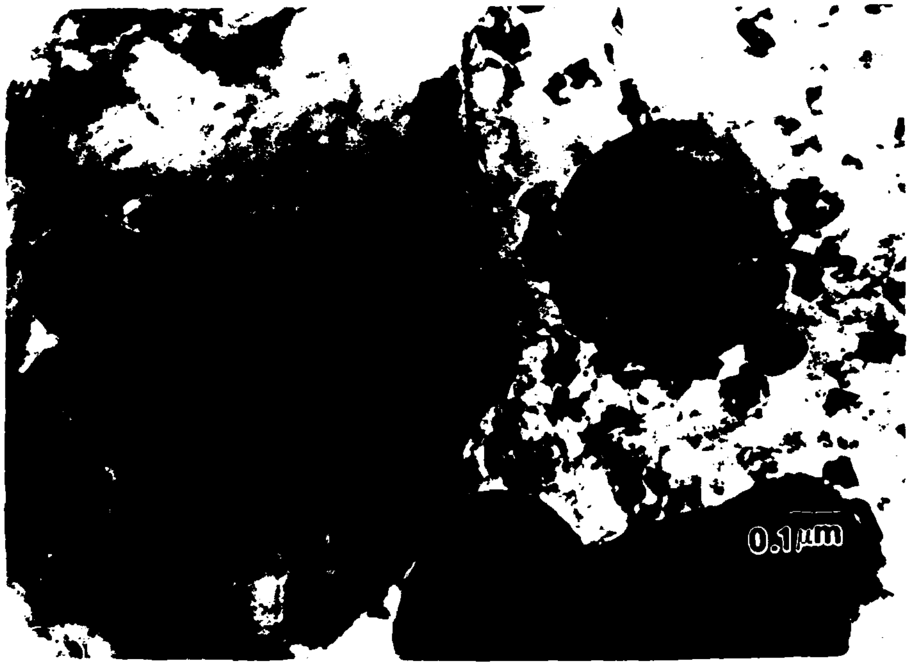

Figure 52. TEM micrograph of the microstructure present in HIP'ed Mg-8wt.% Li-1.5wt.% Si.

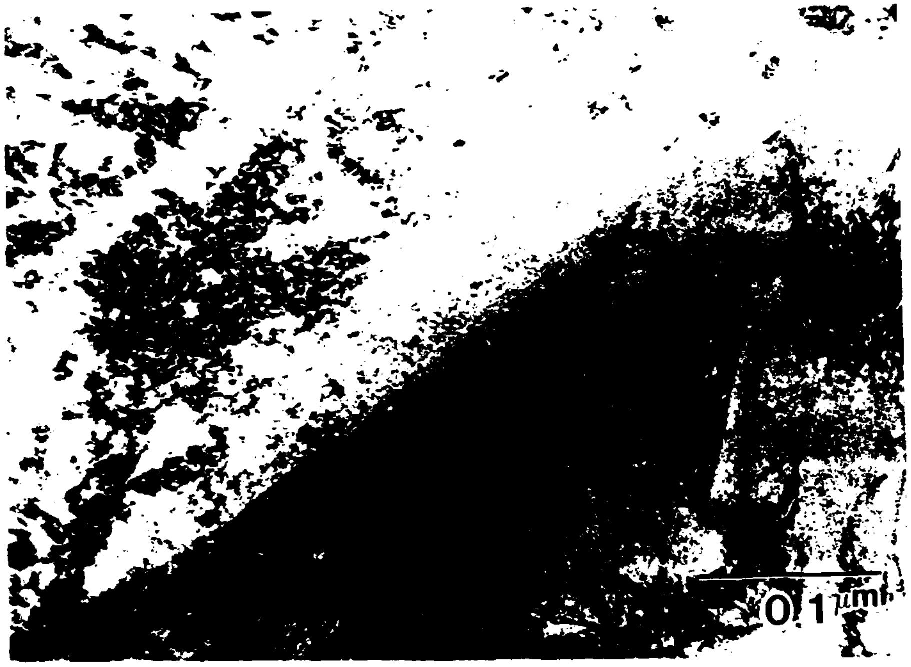

Figure 53. TEM micrograph showing a precipitation in the β grains of of HIP'ed Mg-8wt.% Li.

TABLE 6

Microhardness of melt-spun Mg-Li-Si Alloys

Alloy	As-cast	Melt-Spun
Mg-5wt%Li	40.8	46.3.
Mg-5wt%Li-5wt%Si	51.1	100.4
Mg-8wt%Li	42.8	44.8
Mg-8wt%Li-5.4wt%Si	59.9	117.4
Mg-12wt%Li	39.6	40.2
Mg-12wt%Li-5.8wt%Si	49.4	100.8
Mg-5wt%Si	52.9	100.4

TABLE 7

Tensile Data of Dynamically Compacted Mg-8wt.%Li and Mg-8wt.%Li-1.5wt.%Si Alloy Powders

Alloy	Condition	0.2%Y.S. (MPa)	U.T.S. (MPa)	ε_f
Mg-8wt%Li	as DC	fol	24.0	0.07
	300°C/2hrs	68.2	135	3.7
Mg-8wt%Li-1.5wt%Si	as DC	58.3	68.24	0.26
	300°C/2hrs	93.5	128	0.56

TABLE 8

Compressive Strengths of HIPped Mg-Li and Mg-Li-Si Alloy Powders

Material	Test temp (°C)	0.2%Y.S. (MPa)	U.T.S.(MPa)
Mg	25	86.2	97.8
	200	55.3	72.9
Mg-8wt%Li	25	150.0	240.0
	200	43.7	79.9
Mg-8wt%Li-1.5wt%Si	25	198.9	362.0
	200	75.7	125.4

4. REFERENCES

1. G. Cliff and G. W. Lorimer, J. Microscopy, 110, 107 (1975).
2. H. Jones, Mater. Sci. Engr., 5, 1 (1969-70).
3. R. D. Field, J. W. Zindel and H. L. Fraser, Scripta Metall., 20, 415 (1986).
4. P. Furrer and H. Warlimont, Z. Metallk., 64, 236 (1973).
5. M. H. Jacobs, A. G. Doggett and M. J. Stowell, J. Mater. Sci., 9, 1637 (1974).
6. M. Cooper, Acta Cryst., 23, 1106 (1967).
7. D. J. Skinner, R. L. Bye, D. Raybould and A. M. Brown, Scripta Metall., 20, 867 (1986).
8. P. Skjerpe, Met. Trans., 18A, 189 (1987).
9. J. W. Steeds, In: Introduction to Analytical Electron Microscopy, J. J. Hren, J. I. Goldstein and D. C. Joy (eds.), Plenum Press, New York, 387 (1979).
10. B. F. Buxton, J. A. Eades, J. W. Steeds and G. M. Rackham, Phil. Trans. Roy. Soc. Lond., A281, 171 (1976).
11. International Tables for Crystallography, T. Hahn (ed.), A, 604, D. Reidel Publishing Co., Dordrecht, Holland (1984).
12. G. Phragmen, J. Inst. Metals, 77, 489 (1950).
13. V. G. Rivlin and G. V. Raynor, Int. Met. Rev., 26, 133 (1981).
14. D. Munson, J. Inst. Metals, 95, 217 (1967).
15. C. Y. Sun and L. F. Mondolfo, J. Inst. Metals, 95, 384 (1967).
16. L. L. Rolkin, Fiz. Metal. Metalloved., 55, 733 (1983).
17. D. S. Gencheva et al., Fiz. Metal. Metalloved., 51, 788 (1981).
18. J. W. Cahn and G. Kalonji, in: Proc. Conf. Solid-Solid Phase Transformations, H. I. Aaronson, D. E. Laughlin, R. F. Sekerka and C. M. Wayman, eds., AIME, Warrendale, PA, 3 (1982).
19. P. G. Partridge, Metall. Rev., 118, 169 (1967).
20. J. A. Chapman and D. V. Wilson, Bull. J. Inst. Met., 91, 39 (1962-63).
21. J. T. Stanley, R. D. Field and H. L. Fraser, Int. J. of Rapid Solidification, in press.
22. W. Kurz and D. J. Fisher, Int. Met. Rev., 5/6, 177 (1979).

23. H. E. Cline, Acta Metall., 19, 481 (1971).

24. E. S. Wajda, Acta Metall., 2, 184 (1954).

25. P. G. Shewmon, Diffusion in Solids, McGraw-Hill, New York, 170 (1983).

26. V. V. Kinzhibalo, E. V. Mel'nik and O. F. Zmiy, Russ. Met., 3, 154 (1976).

27. D. J. Miller and H. L. Fraser, in: Proc. ASM Conf. on Enhanced Properties in Structural Metals, Orlando, FL (1986).

6. PUBLICATIONS* FROM AFOSR SUPPORT

The Microstructure of Rapidly Solidified Hyper-Eutectic Al-Be Alloys, Acta Met., **33**, 963, 1985, with D.C. Van Aken.

A Microstructural Comparison of Melt Spun and Laser Surface Melted Aluminum-Molybdenum Alloys, Met Trans. A., in press, with F.C. Grensing.

The Mechanism of Formation of Microstructure in Rapidly Solidified Hypereutectic Al Alloys, Acta. Met., in press, with J.T. Stanley, R.D. Field.

Rapidly Solidified Al-In Alloys, Int. J. of Rapid Solid., in press, with D.C. Van Aken.

Identification of Precipitates in Rapidly Solidified and Heat-Treated Al-8Fe-2Mo-Si Alloys, Scripta Met., **21**, 1987, p.1105, with V.K. Vasudevan.

The Microstructures of Rapidly Solidified and Heat-Treated Al-8Fe-2Mo-Si Alloys Proc. RQ6, Montreal, 1987, with V.K. Vasudevan.

Microstructure of Melt-Spun Magnesium-Silicon Alloys, Scripta Met., **21**, 1987, p.963, with F.C. Grensing.

Structure and Properties of Rapidly Solidified Magnesium-Silicon Alloys, Proc. RQ6, Montreal, 1987, with F.C. Grensing.

Doctor of Philosophy Degrees supported by this program:

Consolidation of Rapidly Solidified Particulate; Dean J. Miller

Microstructural Enhancement of Magnesium Alloys for Elevated Temperature Applications Using Novel Procesing Techniques; Fritz C. Grensing

* All papers co-authored by H.L.Fraser

5. FUTURE WORK

1. Determination of the mechanical properties and fracture toughness of rapidly solidified and extruded Al-8Fe-2Mo-si alloy ribbons.

2. Studies of dislocation-particle interactions in Al-8Fe-2M0-Si alloys to establish the appropriate strengthening mechanisms.

3. Studies of the coarsening behavior of the precipitates in Al-8Fe-2Mo-Si alloys to determine the factors responsible for their stability.

4. Initiate a study of Al_3X intermetallic compounds produced by P/M and RSP methods. Such an approach is important because of the segregation that results when tertiary alloying additions are added.

5. Determination of detailed structure/property relationships in Mg-Gd alloys.

6. Determination of the effect of Li on the solidification modes in Mg-Si alloys; from this conditions required for the production of a coupled micro-eutectic in the ternary alloys will be established.

7. Determination of the rôle of the crystal structure of the matrix on the properties of Mg-Li ternaries will be established.

END
DATE
FILMED
3-88
DTIC